

The Visualization of the Tumor Vascularization using Micro Computed Tomography

Inauguraldissertation

zur

Erlangung der Würde eines Doktors der Philosophie
vorgelegt der
Philosophisch-Naturwissenschaftlichen Fakultät
der Universität Basel

von

Sabrina Lang
aus Kiel, Deutschland

Basel, 2012

Genehmigt von der Philosophisch-Naturwissenschaftlichen Fakultät auf Antrag von:

Prof. Dr. Bert Müller, Fakultätsverantwortlicher

Prof. Dr. Thomas Jung, Co-Referent

Basel, den 13. Dezember 2011

Prof. Dr. Martin Spiess

Dekan

Contents

Summary	1
Zusammenfassung	3
1 Introduction	5
1.1 Micro Computed Tomography to Visualize Tumor Vessel Trees	5
1.2 Quantitative Evaluation of SR μ CT Data from Tumor	7
1.3 Necessary Procedures to Obtain Vector-based Vessel Trees	8
1.3.1 Specimen preparation	8
1.3.2 Data Acquisition using SR μ CT	9
1.3.3 Image Processing	9
2 Visualization of Tumor Vessels using Synchrotron Radiation-based Micro Computed Tomography	11
2.1 Introduction	11
2.2 Materials and Methods	11
2.3 Results and Discussion	12
3 Global and Local Hard X-ray Tomography of a Centimeter-sized Tumor Vessel Tree	15
3.1 Introduction	15
3.2 Methods and Materials	16
3.2.1 Specimen Preparation	16
3.2.2 Synchrotron Radiation-based Micro Computed Tomography	17
3.2.3 Data Analysis	17
3.3 Results	19
3.3.1 Differences between Global and Local Radiographs	19
3.3.2 Analysis of the Flat-field Images	22
3.3.3 The Absorption Histograms of Global and Local Tomography Slices	23
3.3.4 The Absorption Histograms of Global and Local Tomograms	23
3.3.5 Correcting Local Tomograms using Histogram Matching	23
3.3.6 Extending Local Sinograms by Less Detailed Global Data	28
3.3.7 Empirical Cupping Correction	28
3.3.8 Tumor Vessel System	29
3.4 Discussion	29
3.5 Conclusion	34

4	Comparing Grating-based and Propagation-based Phase-contrast Computed Tomography for Soft Tissue Imaging	37
4.1	Introduction	37
4.2	Material and Methods	39
4.2.1	Specimen preparation	39
4.2.2	Data acquisition and processing	39
4.2.3	Tomographic reconstruction	44
4.2.4	Comparative analysis and quality assessment	45
4.3	Results	48
4.4	Discussion	48
4.5	Conclusion	54
5	Morphological assessment of the vessel trees in cancerous and healthy tissues using synchrotron radiation-based micro computed tomography	65
5.1	Introduction	65
5.2	Material and Methods	66
5.3	Image Analysis	67
5.4	Results	69
5.5	Discussion	72
5.6	Conclusion	74
6	Conclusion	77
	Acknowledgments	88
	Curriculum Vitae	90

Summary

Cancer has been one of the most serious diseases and according to the world health organization (WHO) the total number of deaths due to cancer (7.6 million worldwide) will globally increase in future to 13.1 million deaths. Tumor-growth is strongly related to the neo-formation of blood vessels (angiogenesis), since the vessels provide the cancerous tissue with the necessary nutrients and oxygen. For this reason in this study 3D high resolution visualization and parametrization of tumor vessels down to capillary size was carried out. 3D datasets were acquired using synchrotron radiation-based micro computed tomography (SR μ CT) which provided sufficient spatial resolution to make also the smallest vessels down to 4 μ m visible. The contrast in the image is defined by the degree of X-ray attenuation/absorption in the specimen. Because absorption coefficients did not differ significantly between different kinds of soft biological tissue, contrast enhancement of the specimens was needed to obtain sufficient contrast in the tomograms. Contrast enhancement was done either by blood vessel staining using a contrast agent (see Chapter 2) or by generating corrosion casts of the vessels (see Chapters 2 and 4). Alternatively, phase contrast based SR μ CT was used which allowed the vessel tree visualization without any contrast enhancement (see Chapters 3 and 4). This technique measures the phase shift of the photon beam induced by a tumor. The sensitivity was shown to be 25 times higher in comparison to the absorption contrast based data.

By staining the tumor vascularization as seen in Chapter 2, characteristics of the tumor vessel morphology could be revealed. According to the vessel shape and the vessel density it was possible to identify the interface between the tumor and the healthy tissue. Vessels in cancerous tissue appeared strongly twisted. Additionally, several regions were found in tumors where the contrast agent leaked out from the cancerous vessels presumably due to damages of the vessel walls within the cancerous tissue. Vessel-free regions could be observed which gave evidence of necrosis in the tumor.

Most of the tumors exceeded the field of view, i.e. they do not fit the image of the camera, when using high resolution optics to reveal the smallest vessels in the 3D dataset. Local tomography of a tumor cast was carried out to allow high resolution imaging of a region of interest. Because of the interest in the morphology of the whole tumor the local tomography data was compared to the less resolution global SR μ CT data. It was shown that the absorption coefficients in the locally acquired data differed significantly from the ones of the global datasets. These differences are caused most probably by the non-locality in the filtered back-projection calculation which is needed to generate tomograms out of the radiographs. These non-locality artifacts caused the absorption coefficients in the tomographic slices to shift to higher values for increasing distances of the pixels to the rotation center. For this reason this effect is also called 'cupping artifact'. Additionally the high resolution images were affected by edge enhancement due to the coherence of the X-ray beam which caused the peaks in the

image histogram to appear more broadened.

One correction method, de-cupping method, empirically post-corrected the cupping artifacts in the local tomograms using the global data as reference. In another correction method the origination of these artifacts was prevented by extending the local sinograms using the less detailed global ones. Mathematically a sinogram is the radon transform of a tomographic slice [1]. It can easily be constructed using the corresponding radiographs acquired at different rotation angles. While the sinogram extension method proved better correction of the total μ -shift (90%), the de-cupping method was more suitable to correct the histogram broadening (78%). By matching the global and local histograms in the projections the peak broadening caused by edge enhancement could be reduced by 41%.

An alternative method to measure the blood vessels using SR μ CT is based on the measurement of the X-Ray phase shift instead of the X-ray absorption when transmitting through the specimen. The quality of two such phase contrast based SR μ CT methods (grating and propagation-based) was analyzed in Chapter 4, using the contrast-to-noise-ratio, the spatial resolution and the presence of artifacts. For the measured tumor tissue the holotomography technique provided better spatial resolution (SR = 8 μ m) in comparison to the grating interferometry (SR = 24 μ m). The contrast to noise ratio however is much better in grating interferometry (CNR = 57) than in holotomography (CNR = 11).

For further studies the data obtained by holotomography was used, as it provided the visualization of the smallest vessels despite the reduced contrast. Together with the absorption contrast based vessel cast of healthy and cancerous tissue the tumor, measured with holotomography, were analyzed according to their vessel parameters. Skeletonization and vectorization of the voxel based data allowed an easier extraction of the characteristic parameters. The calculations revealed a mean vessel diameter of 8.8 ± 4.2 μ m and a tortuosity value of 0.18 ± 0.19 rad for all vessels in the healthy corrosion cast. The cancerous vessels showed a mean diameter of 5.4 ± 5.5 μ m and a mean tortuosity value of 0.24 ± 0.25 rad. While the value for the vessel diameter showed differences between healthy and cancerous tissue, the tortuosity was more or less equal for both tissues. The quantification of vessel trees using SR μ CT data belongs to the vital steps in understanding of tumor formation and growth and in developing strategies against the disease.

Zusammenfassung

Krebsleiden zählen zu den lebensbedrohlichsten Krankheiten der modernen Welt und laut Aussage der Weltgesundheitsorganisation (WHO) wird die Anzahl von Krebserkrankungen auch in Zukunft weiter ansteigen. Um Fortschritte in der medizinischen Behandlung von Krebspatienten zu erzielen, ist die Erforschung des Tumorwachstums grundlegend. Die Expansion eines Geschwulstes wird durch die Angiogenese vorangetrieben, da die Bildung von neuen Blutgefässen die Versorgung des Krebsgewebes mit Sauerstoff und den nötigen Nährstoffen gewährleistet. Aus diesem Grund beschäftigt sich diese Arbeit mit der Visualisierung und Analyse von Blutgefässen in Tumoren.

Zur 3-D-Darstellung der Blutgefässe wurde Mikro-Computertomographie an Synchrotronstrahlungsquellen (SR μ CT) verwendet. Diese bildgebende Technik liefert hochaufgelöste Aufnahmen, die auch kleinste Blutgefässe mit einem Durchmesser von 4 μ m sichtbar machen. Der Bildkontrast wird dabei durch die Absorption der Röntgenstrahlung in der Probe bestimmt. Bei Weichgewebe sind die Unterschiede in den Absorptionswerten jedoch zu gering, um die Blutgefässe vom umliegenden Gewebe zu unterscheiden. Aus diesem Grund wurden in der vorliegenden Arbeit kontrastverstärkende Massnahmen durchgeführt.

In Kapitel 2 wird beschrieben wie ausreichender Kontrast durch die Färbung der Gefässe mit Hilfe eines Kontrastmittels herbeigeführt wurde, so dass deren Morphologie erkennbar wurde. Die damit gewonnenen Daten machten es möglich, gesundes von krankem Gewebe zu unterscheiden. Erkranktes Gewebe zeigte in den CT-Bildern vermehrt spiralförmige Blutgefässe und man konnte erkennen, dass das Färbungsmittel an einigen Stellen ausgelaufen sein musste. Dies lässt auf eine Nekrotisierung der Blutgefässe schliessen, welche ausserdem zur Folge hatte, dass grosse Bereiche des Tumores überhaupt keine Blutgefässe vorwiesen.

Da viele der untersuchten Tumore grösser als das durch den Detektor vorgegebene Sichtfeld waren, wurden sowohl lokale SR μ CT-Messungen eines ausgewählten Bereiches als auch globale SR μ CT-Messungen des gesamten Tumors, aber mit einer schwächeren Auflösung, durchgeführt (Kapitel 3). Um einen genügend hohen Kontrast zu erhalten, wurde für den Vergleich der globalen und lokalen Messungen ein Blutgefässabguss aus Polymer erstellt. Es stellte sich heraus, dass sich die Absorptionswerte in den lokalen Tomogrammen von denen in den globalen Tomogrammen unterschieden. Diese Unterschiede können auf die Nicht-Lokalität der gefilterten Rückprojektion zurückgeführt werden, ein Verfahren, das die Tomogramme aus den Projektionen errechnet. Diese verursachte eine ansteigende Verschiebung der Absorptionskoeffizienten zu grösseren Werten. Zusätzlich führte die Kohärenz der Strahlung bei der hohen Auflösung in den lokalen Bildern zu einer vermehrten Kantenverstärkung, so dass die Peaks in den Histogrammen breiter wurden. Da die Absorptionswerte in den globalen Tomogrammen den wahren Absorptionswerten der Probe am nächsten kommen, wurden die Werte in den lokalen Tomogrammen denen der globalen Tomogramme angepasst. Um

die Artefakte der nicht-Lokalität zu korrigieren, wurden diese zum einen empirisch bestimmt und aus den Bildern entfernt. In einer zweiten Methode wurde die Bildung dieser Artefakte umgangen, indem vor der Rekonstruktion die fehlenden Bereiche in den lokalen Projektionen durch die entsprechenden in den globalen Projektionen ersetzt wurden. Während die Artefakt-reduzierende Methode die grösstmögliche Korrektur der nicht-linearen Verschiebung der Absorptionskoeffizienten lieferte (78%), wurde die bestmögliche Korrektur der totalen Verschiebung mit Hilfe der Projektionserweiterungen zu 90% herbeigeführt. Die durch Kantenverstärkung verbreiterten Peaks konnte man am besten korrigieren, indem man die Grauwertbereiche in den Histogrammen der Projektionen vor der Rekonstruktion aneinander anpasste (41%).

Eine alternative Methode zur Bildgebung der Blutgefässe mit Hilfe von SR μ CT basiert auf der Messung der durch die Probe verursachten Phasenverschiebung der Röntgenstrahlung. Da es verschiedene Methoden in der Phasenkontrast-basierten μ CT gibt, wurden in Kapitel 4 die Qualitätsunterschiede zweier solcher Methoden (Gitterinterferometrie und Holotomographie) untersucht. Die Qualität wurde unter anderem anhand der räumlichen Auflösung und des Kontrast-zu-Rausch-Verhältnisses definiert. Dabei lag die Gitterinterferometrie mit einem fünffach höheren Kontrast-zu-Rausch-Verhältnis gegenüber der Holotomographie im Vorteil. Die Holotomographie ermöglicht im Gegensatz dazu eine dreimal bessere Auflösung. Obwohl diese Methode einen schwächeren Kontrast vorweist, wurde sie für weitergehende Studien verwendet, da sie die Möglichkeit bot auch die kleinsten Blutgefässe darstellen zu können. Zusammen mit den absorptionsbasierten Tomogrammen der Blutgefässabgüsse, sowohl von gesundem als auch krebskrankem Gewebe, wurden die Holotomographiedaten verwendet, um die Gefässparameter zu bestimmen. Dazu wurden die dreidimensionalen voxelbasierten Daten skelettiert und anschliessend vektorisiert, was die Auswertung erleichterte. Die Berechnungen für gesundes Gewebe ergaben einen mittleren Gefässdurchmesser von $8.8 \pm 4.2 \mu\text{m}$ und ein Ausmass der Gefässwindungen von $0.18 \pm 0.19 \text{ rad}$. Tumore zeigten dagegen einen Gefässdurchmesser von $5.4 \pm 5.5 \mu\text{m}$ und ein Ausmass der Gefässwindungen von $0.24 \pm 0.25 \text{ rad}$. Während die Werte des Durchmessers sichtbare Unterschiede zwischen dem gesunden und dem kranken Gewebe aufweisen, sind bei dem Ausmass der Gefässwindungen im Rahmen der Messungen keine Unterschiede erkennbar. Die Parametrisierung der Blutgefässe mit Hilfe der SR μ CT gehört zu den vielversprechenden Methoden um die Tumorbildung zu untersuchen.

Chapter 1

Introduction

1.1 Micro Computed Tomography to Visualize Tumor Vessel Trees

Cancer is the second most frequent cause of death in society, although the therapeutic strategies are constantly refined [2]. The formation of new blood vessels, angiogenesis [3, 4], is a crucial step for the survival and metastasis formation of malignant tumors [5]. This is because, like normal tissues, tumors require an adequate supply of oxygen, metabolites and an effective way to remove waste products [6]. Although novel therapeutic strategies attempting to inhibit this step are being developed, the biological regulation of this process is still largely unknown. A computer simulation model should help to investigate tumor formation and growth, and finally contribute to the development of treatment strategies like optimizing dose delivery during radiation therapy or systematic selection of anti-angiogenic drugs and improve the insight of the underlying mechanisms [7, 8]. To make sure that the computed results agree with tumors, one has to compare them with measured data. The visualization of the 3D vessel network is therefore crucial for studying the physiological processes related to angiogenesis and vascular diseases.

A most common way to analyze the morphology of blood vessel systems is the use of histology [9]. Unfortunately 3D characterization via serial sectioning is very tedious and time consuming [10]. Also, the sectioning damages the biological material [11]. Promising microscopy techniques, such as two photon microscopy, gives the opportunity of screening localized *in vivo* physiological signals [12, 13]. Unfortunately, multi-photon laser microscopy is still limited to about 200 μm depth and a restricted field of view. Other methods like scanning electron microscopy [14] *in situ* appear really accurate but are restricted to the investigation of several 100 μm , due to the finite penetration ability. Magnetic resonance imaging allows *in vivo* visualization of the vascular network of the whole tumor without causing damage [15, 16]. This technique achieves a resolution in the range of a few 100 μm . However, most of the vessel diameters lie between 3 and 10 μm (50% in the cerebral cortex), therefore micrometer resolution is necessary to visualize the smallest capillaries [17, 18]. Micro Computed Tomography (μCT) is a 3D imaging technique which provides micrometer resolution or by adding X-ray optics even in the nanometer resolution. μCT works like conventional clinical CT where the intensity changes of x-ray photon beams are detected after transmission through the object. The source of the x-rays can be a cone-beam emitting x-ray tube (laboratory source).

Another x-ray source, synchrotron radiation, has several advantages over the conventional x-ray tube. Using synchrotron x-ray sources one gets a coherent and very bright photon beam [19, 20]. The increased photon flux results in a reduced exposure time which causes a reduction in the data acquisition. A reduced experimental time-scale lowers problems due to time dependent mechanical instabilities like shrinkages and expansions of soft biological tissue [20]. Furthermore the synchrotron radiation source can provide a monochromatic beam which avoids beam-hardening artifacts.

Although the contrast is visibly better in Synchrotron Radiation-based μ CT (SR μ CT), one is still not able to make the vessels visible. Conventional absorption based μ CT is based on the attenuation of the light transmitting through the specimen. The attenuation can be described by the Beer-Lambert law:

$$\frac{I}{I_0} = e^{-\mu d} \quad (1.1)$$

I_0 and I are the intensities of the incident and transmitted radiation respectively. The specimen thickness is given by d . The absorption coefficient μ does not differ strongly between different kinds of soft biological tissue. In tumors it is therefore difficult to distinguish between the vessels and their surroundings. To be able to see vessels in conventional SR μ CT one has therefore to increase their contrast. There are contrast enhancing preparation methods, which were successfully applied in imaging the vascular network of the different organs. The most common way of increasing the contrast is the staining method [17, 21–23], where a contrast agent is injected into the vessels which does not penetrate through the vessel walls.

Another promising method is corrosion casting, where a cast agent is perfused in the vascular network of an animal [24–26]. After resin curing (1-2 d), the soft tissue is macerated, followed by decalcification, each for 24 hours. For μ CT the casts can be immersed in osmium tetroxide (OsO_4) for several days to increase the attenuation of the light in the specimen.

Another μ CT technique, where the vessels can be visualized without any contrast enhancing preparations, is the phase contrast based μ CT [27–33]. In phased contrast based μ CT the phase shift of the transmitting beam is determined instead of the attenuation which more sensitive to structural differences within an object. The phase shift is related to the real decrement δ of the refractive index $n = 1 + i\beta - \delta$. β is related to the absorption coefficient μ . Due to its high sensitivity also differences in soft tissue can also be visualized. There are several techniques that have been implemented to visualize variations in the phase. One method to induce the phase shift is the propagation based μ CT [34]. Its main advantage lies in the rather simple experimental setup [35]. No specialized optical elements are required in order to render phase shifts visible as intensity variations, because phase contrast may be achieved by the simple free-space propagation [36]. To obtain the phase shift, projections are acquired at different sample-to-detector distances. The quantity obtained by this measurement is related to the Laplacian (the second derivative) of the refractive index [37]. Although the experimental setup is easy to handle this is not the case for the retrieval of the phase information from acquired data. The phase shift can be obtained by resolving the relationship between the specimen induced phase shift and the contrast recorded at a sample-to-detector distance. There are different approximation techniques to solve this problem. A mixed approach of the contrast transfer function (CTF) and the transport of intensity equation (TIE) can be used to obtain the phase information in the images. The different methods depend on the compositions of the specimen. These methods need data from at least three different sample-

to-detector distances. However, taking a reduced quality into account, one can obtain phase information using the Paganin method where only single-distance data are necessary [36]. Another phase imaging method in tomography is grating interferometry [27, 29, 29, 31, 38]. This method takes advantage of two gratings. One is the phase grating which separates the incoming beam in the first order and generates a self-image at a defined distance. A second grating (amplitude grating) is placed in the plane of the self image which serves as an intensity mask [39]. The differential phase shift is calculated by comparing the intensity distribution without any perturbations with that of an object placed in front of the grating. Although the experimental setup is more complex and needs more mechanical stability in comparison to in-line methods [40], phase retrieval can easily be determined using the phase stepping method [41]. In contrast to the propagation based technique the specimen has to be measured in a medium which offers a similar refraction index to the specimen itself. Tumor samples usually are measured inside a water tank to prevent phase wrapping artifacts. The 3D information can be calculated from absorption and/or phase contrast based μ CT using the filtered back-projection algorithm [1]. The vessels can be isolated from the tomograms using an appropriate segmentation method. But even if the volumetric data allows for an easy vessel tree segmentation, the data have to be translated to vector-based representations to allow the direct comparison with the related computer simulations. From the vectorized data one can easily determine different vessel parameters like the vessel radii and length or the number of bifurcations, which are relevant to define the vessel morphology. From the obtained parameters one is not only able to define differences between healthy and cancerous tissue but can also help to validate and improve computer programs simulating the tumor neo-vascularization for a better insight into tumor growth. The challenge of the tumor vessel analysis down to the capillary size lies 3D imaging including appropriate spatial and density resolution. The GB sized data is needed to be segmented and parametrized properly afterwards.

1.2 Quantitative Evaluation of SR μ CT Data from Tumor

The biggest obstacle in the visualization of the vascular networks lies in the low contrast between the vessels and the surrounding tissue, using conventional absorption μ CT. Different specimen preparation methods and μ CT techniques were carried out to make the vessels visible inside the tumor tissue. In this thesis three different kinds of imaging techniques are proposed to overcome the problem of insufficient contrast.

In Chapter 2 the effectiveness of the contrast enhancing staining technique is presented. For that purpose a closer look at the tumor vessel morphology is taken.

Although the spatial resolution in SR μ CT was sufficient large to make the capillaries visible, limitations can occur depending on the size of the specimen. Because of the limited detector size and the cubically increasing amount of image data produced in moving to smaller voxel sizes, there is a trade-off between resolution and volume that can be acquired in a single scan. The maximum pixel size, which is enough to reveal the smallest capillaries, is approximately 1.5 μ m. As most of the available detectors at synchrotron radiation beamlines have a range of (2048x2048) pixels, the field of view (FOV) is limited to approximately 3 mm. Tumors differ strongly in shape and size. The limitation in the FOV is therefore a limitation in the analysis of the tumor vessels. Cutting the tumor to the appropriate size of the FOV would

be an unpredictable invasion in the tumor morphology. μ CT offers the possibility for region-of-interest (ROI) or local imaging of a specimen which exceeds the FOV. Local tomography however is inherent with diverse artifacts which affect the density distribution and therefore the possibility to segment the vessel tree appropriately.

In Chapter 3, high-resolution local tomography data of the tumor casts were compared with the one obtained by global tomography, where the specimen, in contrary to local tomography, fits the whole field of view of the camera [25]. In order to adapt the absorption values obtained from the two approaches, the de-cupping, sinogram extension and histogram matching was compared. The question arised which of these approaches provides the best results.

Absorption based μ CT images require sufficient contrast to make vessels visible in the tomograms. As contrast enhancement mechanisms in absorption contrast μ CT may cause changes in the morphology of the vascularization, an alternative is proposed in Chapter 4. This μ CT technique is based on the phase contrast, i.e., measures the phase shift of an incoming beam transmitting through an object of interest. Since phase contrast-based μ CT is more sensitive than absorption contrast, it is an appropriate method for the imaging of soft biological tissue. There are different techniques to reveal the phase shift indirectly. The prominent methods, the grating interferometer and the propagation based tomography, which imply the Paganin method and holotomography, are used in the study presented in Chapter 4. The study examines the image quality of the proposed methods in the visualization of soft biological tissue, defined by the spatial resolution, the contrast to noise ratio and the existence of artifacts. Additionally an alternative specimen, here a rat-heart, was included to give a broader spectrum of examples for soft tissue and the found results.

The morphometric analysis of the visualized tumor vessels is presented in Chapter 5. Vessel parameters like the vessel density, the vessel diameter and the bifurcation density are analyzed to define the characteristics common and unique to tumor and healthy tissue. The multi-modal data (absorption contrast μ CT of corrosion casts and holotomography) give evidence of the effectiveness to analyze the vascular structures of tumors.

The final conclusions can be found in Chapter 6.

1.3 Necessary Procedures to Obtain Vector-based Vessel Trees

1.3.1 Specimen preparation

The measured tumor samples were obtained from the Institute of Biomedical Engineering at ETH and University of Zurich. After the in vivo experiments [42], when the tumor reached a size which caused sufferings to the animal or led to a preferred size for following experiments, the mice with a weight of approximately 25 g were euthanized by an intraperitoneal injection of 350 ml Ketamine/Xylazine, the quantity varied depending on the individual weight of the mouse. Depending on the imaging technique used, the tumor, was isolated and stabilized on a sample holder to prevent movement of the specimen during data acquisition.

Staining : The contrast agent was a suspension of nanometer-size barium sulfate (BaSO_4) and physiological solution with a concentration of 80 g/l. The suspension was filtered (pore size $\pm 1 \mu\text{m}$, BD Falcon, USA) to obtain particles with dimensions less than the diameters of the smallest vessels. Before injection, the suspension was homogenized using the ultrasonic bath Sonorex Digital 10P, Bandelin at a temperature of 37 °C for a period of 10 min. After

anesthesia the animal was perfused with 250 ml heparin to avoid thrombosis. Finally, 10 ml barium sulfate suspension was injected via the left ventricle of the heart applying the peristaltic pump (Watson Marlow 101 U/R) as described in [43]. The barium sulfate solution was mixed with ink to optically follow that the staining of the whole vascular system was complete. Staining was judged as complete when the spleen became colored.

Corrosion Cast: Before application the resin was mixed with an hardener. As with the staining method the mice were perfused with 250 ml heparin to avoid thrombosis. Thereafter the polymer was injected with a peristaltic pump. Also here the injection could be traced using blue ink as a marker. The polymer hardening took 2-3 days then the corrosion of the soft and hard tissue was carried out using formic acid. After 5-7 days the mouse body was dissolved by the acid and only the polymer in form of the mural vascularization remained. The tumor vessels were cut from the cast and coated with osmium tetroxyd (OsO_4) to provide better contrast in the tomograms.

Phase Contrast Imaging: Since no contrast enhancing was necessary after extraction the tumor was only fixed in 4-5% para-formaldehyde (PFA) to prevent the tissue from damages due to decomposition and transferred into polymer containers for the imaging using SR μ CT.

1.3.2 Data Acquisition using SR μ CT

The SR μ CT-measurements were performed at the beamline TOMCAT (SLS at PSI, Villigen, Switzerland) and BW2 (HASYLAB at DESY, Germany) for absorption based μ CT and at the beamline ID19 (ESRF, Grenoble, France) for the phase contrast based μ CT. The beamlines offered the experimental equipment and software for the μ CT measurements. As the available experimental equipment for the grating interferometer offered only the possibility to carry out medium resolution tomography, it was necessary to build a high-resolution (spatial resolution is better than 5 μm) grating interferometer at the beamline ID19. For that purpose the construction of the setup and the experimental conditions were developed. The construction also required the application of the motors running by the available software to control the gratings. For the in-line tomography experiments no adoptions were required as no special setting is needed and the software for the data acquisition was already provided by the beamline. In the case of the specimen to be measured in PFA one had to take into account that bubble development could cause artifacts in the tomograms due to specimen movements or phase wrapping in phase contrast μ CT. To reduce the bubble development the specimens were therefore degassed in a vacuum chamber at around 10 mbar to remove the dissolved air in the liquid. After data acquisition the tomograms were generated by fully automatic reconstruction tools based on filtered back projection [1]. Each synchrotron beamline provided a corresponding reconstruction tool for this purpose. Before the reconstruction of the phase contrast based μ CT data, one had to retrieve the phase shift information of the raw data.

1.3.3 Image Processing

To obtain the phase information from the acquired images of the grating interferometry and the propagation based tomography, phase retrieval processings are necessary. For the different techniques adequate software was provided at ESRF (Computer code in IDL (ITT Visual Information Solutions, Boulder, Colorado, USA), for grating interferometry [44], ANKAphase for Paganin [45] and a phase retrieval algorithm for holotomography implemented in GNU

Octave version 2.1.73 [37]). While the tools for the grating interferometry and the Paganin are fully automatic, the holotomographic reconstruction needed pre-processing, for example, the alignment of the one-angle projections acquired at different sample-to-detector distances. For data comparison of specimens which were measured under different imaging conditions, registration was required. For the comparison of two projections or two single tomograms 2D registration was performed with a registration algorithm implemented in Matlab. In case of 3D data registration the tool offered by [46] was used.

For the visualization of the vessels the voxels which are part of the vessels had to be segmented. In the absorption contrast based μ CT data of the stained specimen and the corrosion cast this was easily be done by defining an appropriate intensity-based threshold. Quantitatively this threshold was obtained by using the Otsu method or by finding the intersection points between the Gaussians of the vessels and the surrounding objects in the histogram. This kind of segmentation is very effective as long as the object of interest is presented by distinguishable Gaussians in the histogram. As soon as the histogram peaks of two different objects merge together this method can not be used to segment the corresponding objects separately. This is the case in the phase contrast based tomograms, where the intensity values of the vessel are shared with other objects in the surrounding tissue. Setting a threshold would segment both objects, therefore a feature-based segmentation was needed. In case of the vessels which was approximated as tubes which differ in length and diameter the Frangi filter was applied. The Frangi filter is based on the advanced line detection tool described in [47] and [48].

For the analysis of the vessel characteristics a vectorization tool was developed (see Chapter 5) which allows extraction of vessel parameters and additionally decreases the data size by approximately 50%. The vectorization tool needs two formats for each dataset. One is the segmented and binarized 3D dataset, the other one contains its centerline. To obtain the centerline of the 3D image a skeletonization tool offered by [49] was used.

For the 3D visualization of the blood vessels the software VG Studio Max 2.0 (Volume Graphics, Heidelberg, Germany) was applied. Thresholds and colors were manually selected to elucidate the features of interest.

Chapter 2

Visualization of Tumor Vessels using Synchrotron Radiation-based Micro Computed Tomography

2.1 Introduction

The vascular structure of tumors differs from that of healthy tissue. To understand the formation of cancerous tissue, the vascular network of tumors should be uncovered down to the capillary level. Standard synchrotron radiation-based micro computed tomography (SR μ CT) in absorption contrast mode provides the necessary micrometer resolution [17] even for centimeter-sized tumors [21]. The visualization of a vessel tree, however, also requires sufficient contrast. Because the tissue consists mainly of water and low absorbing species, SR μ CT does not lead to significant X-ray absorption differences between vessels and surrounding tissue. So, the successful application of absorption contrast tomography requires dedicated tissue preparation procedures including embedding [22] and corrosion casting [23]. The more common procedure is the use of staining materials such as the incorporation of barium sulfate into the vessels [10, 11, 17, 21, 25].

2.2 Materials and Methods

The present study is based on the injection of a barium sulfate suspension with a grain size of 0.5 to 1 μ m and a concentration of 80 g/l via the left ventricle of the heart of mice under anesthesia using a peristaltic pump. The mice contained C51 or U87 tumors grown during two to three weeks until they clearly emerged to be easily extracted post mortem. The tumors were transferred to Eppendorf tubes filled with 4% para-formaldehyde for fixation. For the tomography measurements at the beamline TOMCAT (SLS at PSI, Switzerland) using the photon energy of 18 keV (bandwidth 2% to 3%) the container was fixed on the high-precision manipulator that rotated the tumor from 0° to 180° in steps of 0.12° to record 1501 projections. It should be mentioned that continuous irradiation of the specimen caused the formation of bubbles. To master this serious problem, the shutter in front of the specimen was closed during CCD-readout. Hence, the irradiation could be interrupted by 0.1 s between the exposure periods of 0.3 s per projection. The conventional filtered back-projection algorithm

served for the reconstruction. Because the specimen was significantly larger than the field of view, local tomography of the inner part was performed, which yielded relative local X-ray absorption coefficients. The 3D representations of the vessel morphology were generated by means of VG Studio MAX 1.2.1 (Volume Graphics, Heidelberg, Germany).

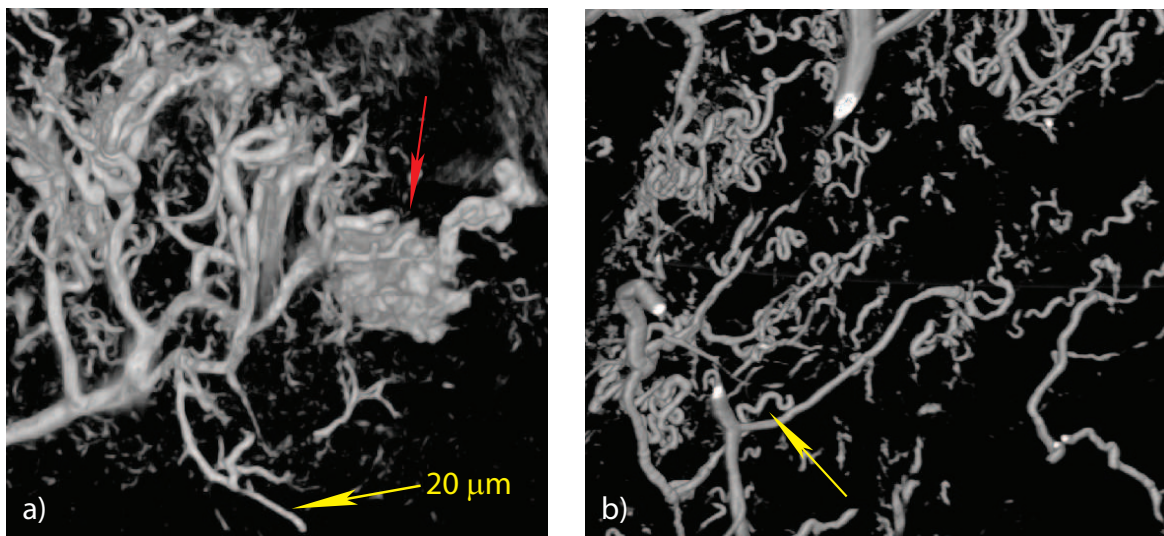


Figure 2.1: *The 3D representation shows the stained vessels. The yellow-colored arrow denotes an about 20 μm -wide vessel. The red-colored arrow indicates a barium sulfate accumulation associated with the contrast agent as the result of a damaged vessel wall. b) The 3D image demonstrates that many capillaries in the tumor exhibit a spiral shape as exemplarily indicated by the yellow-colored arrow.*

2.3 Results and Discussion

The homogeneous staining of the capillaries using barium sulfate micro- and nanometer sized particles is demanding, since the carrier medium has to exhibit low viscosity that associates with density differences to the barium sulfate. Consequently, sedimentation phenomena cannot be avoided, which result in an inhomogeneous sulfate particle distribution of the vessel trees [11, 17]. The smaller vessels often appear interrupted [17]. In order to improve the situation, the suspension should be suitably selected. The sedimentation velocity used, derived from Stokes law, should be as small as possible. It depends on the particle's grain radius r_p , the density difference between the carrier medium and the particles $\rho - \rho_p$, the viscosity of the fluid η and the gravitation constant g :

$$v_{sed} = \frac{2(\rho - \rho_p) \cdot r_p^2 \cdot g}{9\eta} \quad (2.1)$$

The most important parameter is the barium sulfate particle size. It has not only to be smaller than the smallest capillary, but well below one micrometer to reach low enough sedimentation velocities. Much smaller nanometer-sized particles, however, show a strong tendency to form clusters, which stop the perfusion through the blood vessel tree. Accordingly, globular barium

sulfate particles with a narrow sub-micrometer size distribution provide most homogeneous vessel staining. Healthy and cancerous tissue can be straightforwardly differentiated, since the fast grown tumor tissue exhibits a much higher density of capillaries than the surrounding healthy vascular structure. In several regions, however, the opposite behavior has been observed [21]. The explanation lies most probably in the necrosis of the inner part of the tumor. It is hypothesized that the path from the arteries to the veins within the necrotic part of the tumor is not intact anymore. Furthermore, there are several indications for damages of the vessel walls. First, already in alive mouse the tumor becomes dark red in the advanced stages indicating extended regions of blood coagulation. Second, the applied pressure for the injection of the barium sulfate suspension generates leakage as experimentally found at several sites of the tumor tissue [21] and demonstrated in Figure 2.1(a). Nevertheless, blood vessels in the cancerous tissue with diameters down to $11 \mu\text{m}$ could be clearly identified. The morphology of the vessel tree and the related shape of individual vessels within the cancerous tissue significantly differ from the healthy parts. The 3D representation in Figure 2.1 b) demonstrates that many vessels show a spiral shape, which belongs to typical signs of cancer tissue [50]. These details cannot be identified using *in vivo* magnetic resonance imaging, where only vessels with diameters down to about $80 \mu\text{m}$ come to light. The quantitative analysis of the barium sulfate stained vessels of the tumor, however, remains questionable, since significant parts are not stained and parameters such as the bifurcation probability versus vessel diameter cannot be meaningfully extracted. Therefore, the value of our study for the validation of computer simulations on the tumor formation [7] is limited. Here, it is highly desirable to improve the spatial resolution of phase contrast techniques that usually offer enough contrast to visualize the vessel tree without any stain even in para-formaldehyde solution [21].

Chapter 3

Global and Local Hard X-ray Tomography of a Centimeter-sized Tumor Vessel Tree

3.1 Introduction

Cancer is a leading cause of death worldwide [2]. Many studies in cancer research investigate the neo-vascularization in cancerous tissue to get insight in tumor formation and growth [21] with the aim to develop strategies against the disease. For the detailed investigation of the underlying phenomena, a three-dimensional visualization of the tumor vessel tree down to the capillary level would be most helpful. The smallest capillaries in the tumors (of centimeter size) have a diameter of around $4 \mu\text{m}$ and a wall thickness of about $1 \mu\text{m}$ [24, 51]. Synchrotron radiation-based micro computed tomography (SR μ CT) reaches the sub-micrometer regime without X-ray optics [52, 53], but for the given resolution the field of view (FOV) is restricted. For specimens, which exceed the FOV, one can only cut the specimen into pieces of appropriate size or use the stitching technique where the projections are recorded at different asymmetric rotation axes to obtain the entire projection images of the tumor for each rotation angle [19, 53]. These techniques are time-consuming because they require the acquisition of many more detector frames than a standard tomography scan. Moreover, the volume of the data tends to become huge, which results in long times needed for data reconstruction, and difficult management of the data. Consequently, many research teams only acquire a region of interest (ROI) of the entire projection and reconstruct just these partial datasets, an approach known as local tomography or truncated-projection tomography. In local tomography, however, the reconstructed X-ray absorption coefficients $\mu(x,y,z)$ do not correspond to the values obtained from globally acquired data [28, 53–55]. The deviations, a result of the interior problem, can only be slightly evaded [28] but not completely corrected [56]. Different algorithms have been reported to partially correct the related artifacts [57, 58]. For cases in which the absorption coefficients are known *a priori* for a subset of the ROI to be reconstructed, the problem can be solved, but this requires iterative algorithms, which are relatively complex and computationally intensive [59]. The present work deals with the question how far the local X-ray absorption coefficients $\mu(x,y,z)$ in the different local tomograms can be corrected using the information from the less detailed global data. First, it is tried to shift and scale

the binned μ -values of the local data to obtain the ones of the global tomogram. Second, the artifacts in the local tomogram have been reduced combining the high-resolution projections with less detailed data of the missing regions before reconstruction. Third, using the rigid or affine registration the influence of distortions for example as the result of the objective's aberration is addressed. Hence, the pros and cons of local tomography and the combination between local and global tomography are elucidated. It should be noted that the corrosion cast of the tumor vessel tree is especially suitable for this kind of evaluation as only two components (polymer and air) are present and, therefore, the density resolution is not a limiting factor.

3.2 Methods and Materials

3.2.1 Specimen Preparation

Three balb/c nude mice (Charles River Laboratories, France) have been used for the experiments in strict adherence to the Swiss law from animal protection. A suspension of 106 C51 tumor cells (murine colon carcinoma) was injected subcutaneously on the left flank of each animal. Ten days following injection, when the tumor have reached an average diameter of about 10 mm, mice were sacrificed and perfused with a polyurethane-based material [25] in order to produce a corrosion cast of the whole circulatory system. The casted tumor were subsequently extracted and treated with OsO_4 to enhance the contrast in SR μ CT. The tumor cast was fixed on the sample holder with wax, as shown in Figure 3.1.

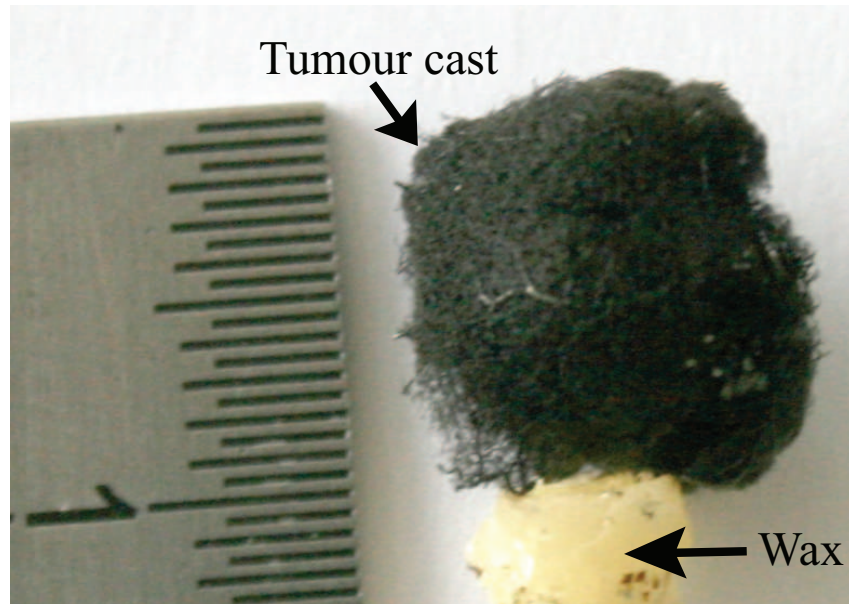


Figure 3.1: *The photograph shows the corrosion cast of C51 tumor vessels grown in nude mouse. The black color of the polyurethane cast results from the OsO_4 treatment. Wax served for fixation on the rotation stage for data acquisition.*

3.2.2 Synchrotron Radiation-based Micro Computed Tomography

SR μ CT measurements were performed at the TOMCAT beamline (Swiss Light Source SLS, Paul Scherrer Institute, Villigen, Switzerland) in absorption contrast mode [60]. A double multilayer monochromator was used to select a photon energy of 15 keV. The tumor cast was fixed on the rotation stage to acquire 1500 projections in 0.12° steps between 0 and 180° . The high-resolution imaging detector is based on a 4.2-megapixel CCD camera (PCO [61], Germany, 2048×2048 pixels; $7.4 \mu\text{m}$ physical pixel size) coupled to the X-ray beam by a microscope lens system (Optique Peter, Lyon, France) and a $20 \mu\text{m}$ -thin single-crystal scintillator made of cerium-doped lutetium aluminum garnet (LAG:Ce) which converted the X-rays into visible light. The microscope objective determines the magnification and the actual effective pixel size on the specimen scale. In this experiment, a PLAPO1.25 \times (numerical aperture (NA) 0.04) and a UPLAPO10 \times (NA 0.4) objective from the Olympus UIS series (Olympus Corporation, Tokyo, Japan) were used. Tomograms of the whole specimen were measured using the 1.25x objective; the effective nominal pixel size with this objective was $5.92 \mu\text{m}$. The field of view of 12 mm for this setup was sufficient to enclose the maximal diameter of the tumor. But the pixel size was too large to discriminate between tiny capillaries and to extract their diameters. Six hours after the global measurements the setup is changed to 10x objective, which leads to a lateral dimension of $0.74 \mu\text{m}$ for each detector pixel. The resulting FOV, however, is only 1.5 mm wide, which is substantially smaller than the tumor size. Therefore, this objective was only applied to perform local tomography. For both settings an exposure time of 0.175 s per radiograph was used. The global and local measurements were carried out each within approximately five minutes. The distance between the specimen and scintillator was estimated to 2 mm for global and local data acquisition. This short distance was chosen to minimize the effect of edge-enhancing propagation-based phase contrast, although this phenomenon cannot be completely eliminated. At the X-ray wavelength of 0.83 \AA , the characteristic width of phase-contrast fringes at this propagation distance is $(2 \text{ mm} \times 0.83 \text{ \AA})^{0.5} = 0.4 \mu\text{m}$. In the reconstructed tomograms, this leads to bright/dark fringe pairs, which broaden the histograms of the absorption coefficients. The distance between the camera and the scintillator was 30 cm whereby the scintillator to objective distance was 2 to 3 mm for the 0.04 objective lens and several $100 \mu\text{m}$ for the 0.4 objective lens.

3.2.3 Data Analysis

Flat-field Correction

Flat-field images were taken before and after the acquisition of the projection radiographs in each tomography scan. The mean intensity of the flat-field images taken before data acquisition was higher by 7.2% for the global and by 2.0% for the local datasets than the ones recorded after data acquisition. This can only partly be explained by variations of the electron beam current in the source, because the top-up mode operation of the SLS keeps these variations to approx. 2%. The reason could be the darkening of the detector lens optics and/or predominantly, thermal changes of the monochromator. In the radiographs measured with a pixel size of $5.92 \mu\text{m}$ there are areas without X-ray absorbing specimen, which allows extracting the time dependent decay of intensity. This information was implemented into the flat-field correction of the radiographs. For the flat-field correction of the data acquired with a pixel size of $0.74 \mu\text{m}$, the background images taken before and after the projection

radiographs were interpolated linearly before flat-field normalization.

Reconstruction

The tomographic reconstruction of both the global and the local tomography datasets was performed using the filtered back-projection technique, implemented in the parallel-beam reconstruction software PyHST (European Synchrotron Radiation Facility, Grenoble, France) [62].

Projection Analysis

The global and local projections were compared to determine potential differences between the two objectives. The projections were termed global for $5.92 \mu\text{m}$ pixel size and local for $0.74 \mu\text{m}$ pixel size. For comparison the corresponding ROIs in the global and local projections were selected. Rigid registration based on similarity transform was carried out (see Figure 3.2) to identify the same ROIs (common volume) in both images [63]. The software used for the registration was MATLAB R2010a and Simulink (Mathworks Inc., Natwick, MA, U.S.A.). The similarity transformation in two dimensions includes the two translation parameters (t_x , t_y), uniform scaling (s) and one rotation parameter (φ).

$$\begin{pmatrix} x' \\ y' \end{pmatrix} \begin{bmatrix} s \cos \varphi & -s \sin \varphi \\ s \sin \varphi & s \cos \varphi \end{bmatrix} \begin{pmatrix} x \\ y \end{pmatrix} + \begin{pmatrix} t_x \\ t_y \end{pmatrix} \quad (3.1)$$

The coordinates x' and y' describe the transformed coordinates. The registration process implies that one image (floating image) is transformed according to the reference image until optimal similarity is achieved for the similarity function. Here, the 'Normalized Mutual Information' (NMI) was used as similarity function, which allows the registration of images with different intensity distributions [64]. To obtain the NMI, first the joint histogram $h(a, b)$ of the two images had to be determined. The components consist of the X-ray absorption coefficients from local image (a) and the absorption coefficients from the global image (b). The intensity values in the joint histogram correspond to the counts of the absorption-value combinations in the local and the global image, respectively. The values of the joint histogram (a, b) describe the number of joint pixels between the reference and floating images. When creating a joint histogram of identical images all values lie on a diagonal through the origin. From the joint histogram the probability density function $p(a, b)$ can be determined:

$$p(a, b) = \frac{1}{N} h(a, b) \quad (3.2)$$

where N is the number of values in the joint histogram. $p(a, b)$ describes the probability that two pixels in the reference and floating images with the same coordinate have the intensity values a and b . Using $p(a, b)$ the Shannon-Wiener entropy H_{ab} could be determined:

$$H_{ab} = - \sum p(a, b) \log (p(a, b)) \quad (3.3)$$

The higher the similarity between two images, the lower is the Shannon-Wiener entropy. The NMI Y_{ab} is determined using the Shannon-Wiener entropy. The advantage of the NMI against the entropy is that it does not simply maximize the overlap of air.

$$Y_{ab} = \frac{H_a + H_b}{H_{ab}} \quad (3.4)$$

The NMI maximizes at the optimal alignment and can be thought of as a measure of how well one image explains the other. For the preparation of the projections for the registration a region, which is seen in the global as well as in the local projections is manually cropped. The cropped region was defined to be the floating image. The reference image here was the local projection, which had been binned by a factor of eight, the nearest integer value to the scaling parameter, to obtain approximately the same number of pixels in both datasets. After registration the rotation and translation parameters were used to refine the cropping. The scaling parameter was applied to refine the re-sample factor for re-sizing the local projection. Re-scaling was achieved by 2D cubic convolution interpolation of the image. The registration was repeated using the optimized floating and reference images until maximal similarity between the images were achieved. A histogram was calculated from the cropped global and the re-scaled local projections to compare the intensity distribution of both images.

Tumor Analysis

Analogue to the projections, a three-dimensional (3D) registration tool [46] to register the tomography data was applied. The transformations were carried out along the x-, y- and z-axes so one obtained the translation parameters (t_x, t_y, t_z) . The scaling depends here on three orthogonal directions. Hence, the three scaling parameters s_x, s_y , and s_z were introduced. The histograms of the cropped global and the re-sampled local 3D datasets were determined.

Histogram Analysis

Histograms characterize the contrast and density resolution of tomography data [65]. Here, the peak positions and the related full-width-at-half-maximum (FWHM) values were determined. The histograms of the global and local tomograms were compared.

3.3 Results

3.3.1 Differences between Global and Local Radiographs

Figure 3.3 (a) shows a characteristic global radiograph (pixel size $5.92 \mu\text{m}$). The dashed rectangle represents the region used for local tomography. The full-line rectangle indicates the selected ROI. The radiographs depicted in Figure 3.3 (b) to (e) correspond to this ROI and contain grids as guidelines. The radiograph in Figure 3.3 (b) corresponds to the local projection (pixel size $0.74 \mu\text{m}$). The related down-sampled radiograph using a factor of 8.11 is shown in Figure 3.3 (d). The factor 8.11 originates from the scaling of the rigid registration with the global data. Figure 3.3 (c) is the cropped part of the global projection as given in the full-line rectangle. The image in Figure 3.3 (e) shows the difference image between the global and the down-sampled local projection. In order to get a more detailed understanding of the differences between global and local radiographs, their histograms and selected line profiles are displayed in Figure 3.4. The histograms and line profiles originate from the data shown in Figure 3.3 (c) and (d). The locations of the profiles are denoted using the dashed lines in

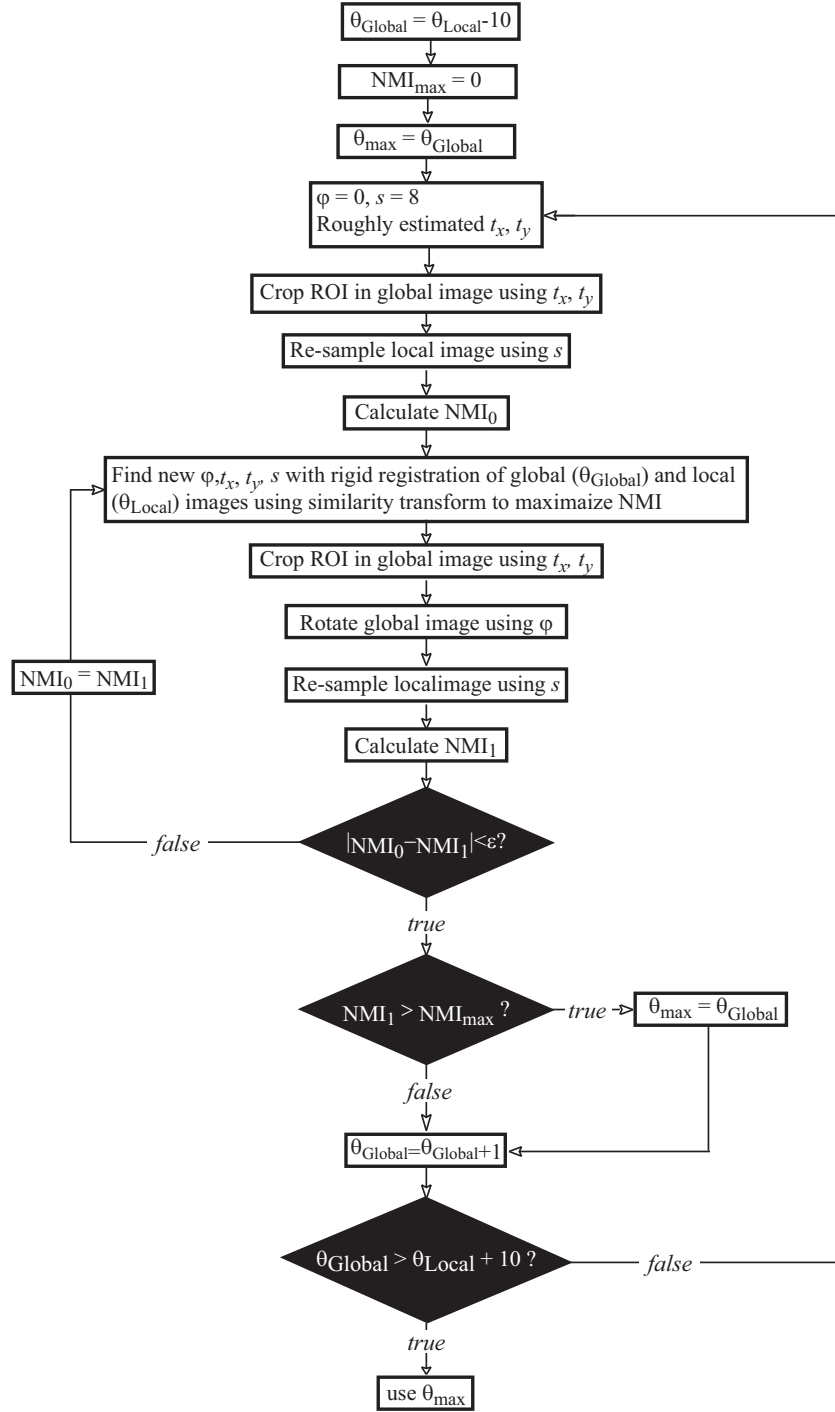


Figure 3.2: The registration procedure of local and global data is summarized in the flow diagram. θ describes the rotation angle step at which the projection was scanned. The local projections serve as reference the global projections as floating image.

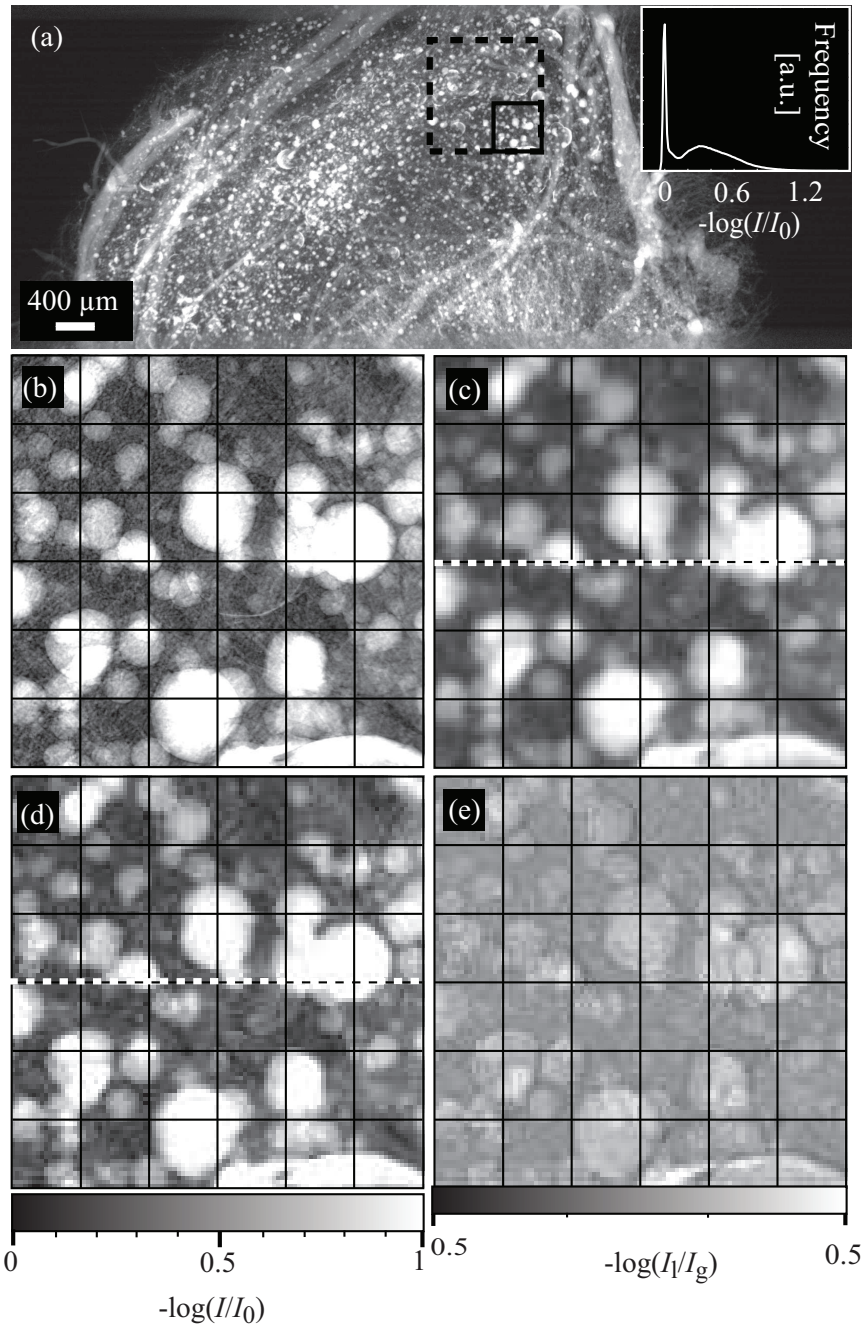


Figure 3.3: The radiographs of the tumor vessel cast were measured at TOMCAT beamline (SLS at Paul Scherrer Institute, Villigen, Switzerland): (a) global radiograph with a pixel size of $5.92 \mu\text{m}$; dashed rectangle illustrates the region measured for local tomography with a pixel size of $0.74 \mu\text{m}$; full line rectangle denotes the region-of-interest shown in the other images: (b) radiograph of local tomography using a pixel size of $0.74 \mu\text{m}$, (c) cropped area from global radiograph, (d) re-sampled image from local radiograph; (e) difference image between the (I_g) and re-sampled local (I_1) projection to reveal intensity differences. The $100 \mu\text{m}$ grids are incorporated as guidelines.

Figure 3.3. Both diagrams confirm the 35% higher I/I_0 -range in intensity for the local data. As expected, the profile of the local projection shows more details.

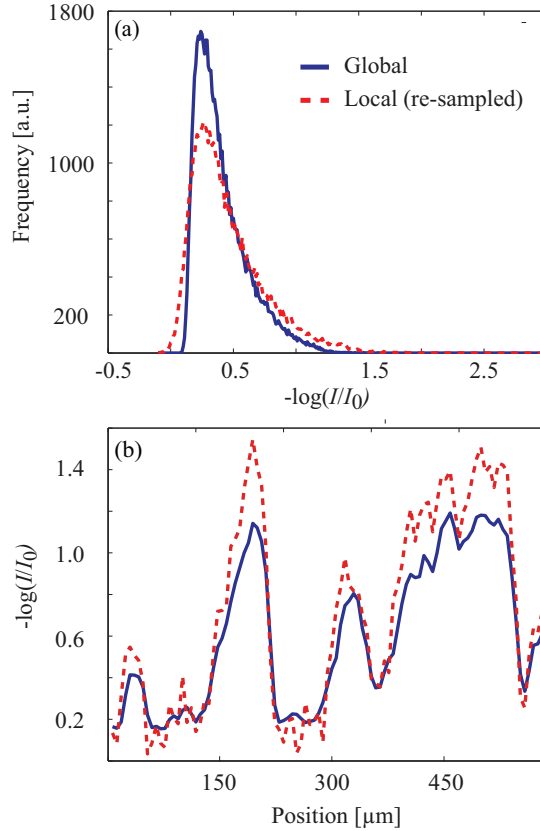


Figure 3.4: (a) The histograms of the global radiographs (blue-colored full line) and of the local radiographs (red-colored dashed line) are obtained from the ROI in Figure 3. (b) The line profiles denoted by the dashed lines in Figure 3 also show that the dynamic range of the local radiographs is by about 30% larger with respect to the global data.

3.3.2 Analysis of the Flat-field Images

The flat-field images (see Figure 3.5) show the typical stripes that come from the multilayer monochromator [20]. The signal intensity in these raw data describes the number of X-ray photons which have been converted into visible light and recorded by the CCD camera. The entity in which the signal is measured is called analogue-to-digital unit (ADU). The signal is much lower in the global image (Figure 3.5 (a)) than in the local image (Figure 3.5 (b)). The flat-field image in Figure 3.5 (b) is down-sampled using the factor of 8.11 to obtain the same number of pixels in the two images. The vertical profiles along the dashed lines in the images show the quantification of the observed intensity differences and are shown as examples in Figure 3.5 (c). The related histograms of the 2D images shown in Figure 3.5 (d) differ in peak position by 34% and in FWHM by 75%. The incident photon flux and exposure times per detector frame and the CCD as well as the scintillator used for both measurements were identical, so that the differences must be attributed to the detector lens optics. Indeed, these

differences can be quantitatively explained from the different magnifications and numerical apertures of the microscope objectives used (see below) and should be fully eliminated as the result of flat-field corrections. The ADUs of the re-sampled local flat-field image shows visible over-saturation by 9.3%. The maximal ADU value in the non-re-sampled local flat-field image is 0.5% below the saturation limit.

3.3.3 The Absorption Histograms of Global and Local Tomography Slices

Figure 3.6 (a) shows a selected slice of global tomography from the tumor cast. The dashed circle encloses an area imaged in local tomography. The local region has been found in the global tomograms by 3D registration. The area within the square is presented in image of Figure 3.6 (c) as cropped, in the image of Figure 3.6 (d) as local tomography slice re-sampled prior reconstruction using the scaling factor of 8.11, and in the image of Figure 3.6 (e) as high-resolution local tomography slice. The incorporated grids validate the appropriate registration. The differences between the images are properly reflected by the histograms in Figure 3.6 (b). The histogram of the local tomography slices is remarkably broader than that of the global data. Even more important, there are substantial shifts of the peak positions to higher X-ray absorption coefficients.

Comparing the two histograms of local tomography one recognizes that the re-sampling has caused a 57% reduction of the FWHM of the air peak close to $\mu = 0$. Such a reduction is the result of the large re-sampling factor and the associated binning [65]. The second peak located between 10 and 20 cm⁻¹ originates from the Os-loaded polyurethane. There is a third peak above 60 cm⁻¹ (not shown in Figure 3.6 (b), see Table 3.1), which stems from remaining bone (also Os-loaded) and relates to the bright clusters in the tomography slices.

3.3.4 The Absorption Histograms of Global and Local Tomograms

Figure 3.7 compares the absorption histograms of the 3D datasets. Figure 3.7 (a) shows the effect of re-sampling using the scaling factor 8.11. As already recognized for the 2D data the re-sampling gives rise to significantly sharper peaks. It is reasonable to analyze the effect of local reconstruction in absence of the differences in the optics. This can be achieved by truncating the ROI from the global projections before reconstruction is carried out. In Figure 3.7 (b) the histograms of the globally acquired images, where ROI cropping took place after (blue-colored, full line) and before (red-colored, dashed line) reconstruction, are shown. The locally reconstructed data are slightly shifted to higher absorption coefficients and exhibit significant peak broadening. Nevertheless, peak shift and broadening are much less pronounced than for the locally acquired data.

3.3.5 Correcting Local Tomograms using Histogram Matching

Local tomography does often not provide the correct local X-ray absorption coefficients, cp. Figure 3.7. Therefore, the application of histogram matching well known from image processing to adjust the histograms of two images [66] might be an appropriate approach to correct the local X-ray absorption coefficients. In order to keep the procedure simple, the tomograms were directly modified instead of the radiographs. However, it was chosen to use a simplified approximation to histogram matching that uses only two scalar parameters and approximates the two histograms by stretching and shifting one of them. As shown in Figure 3.4 (a), the

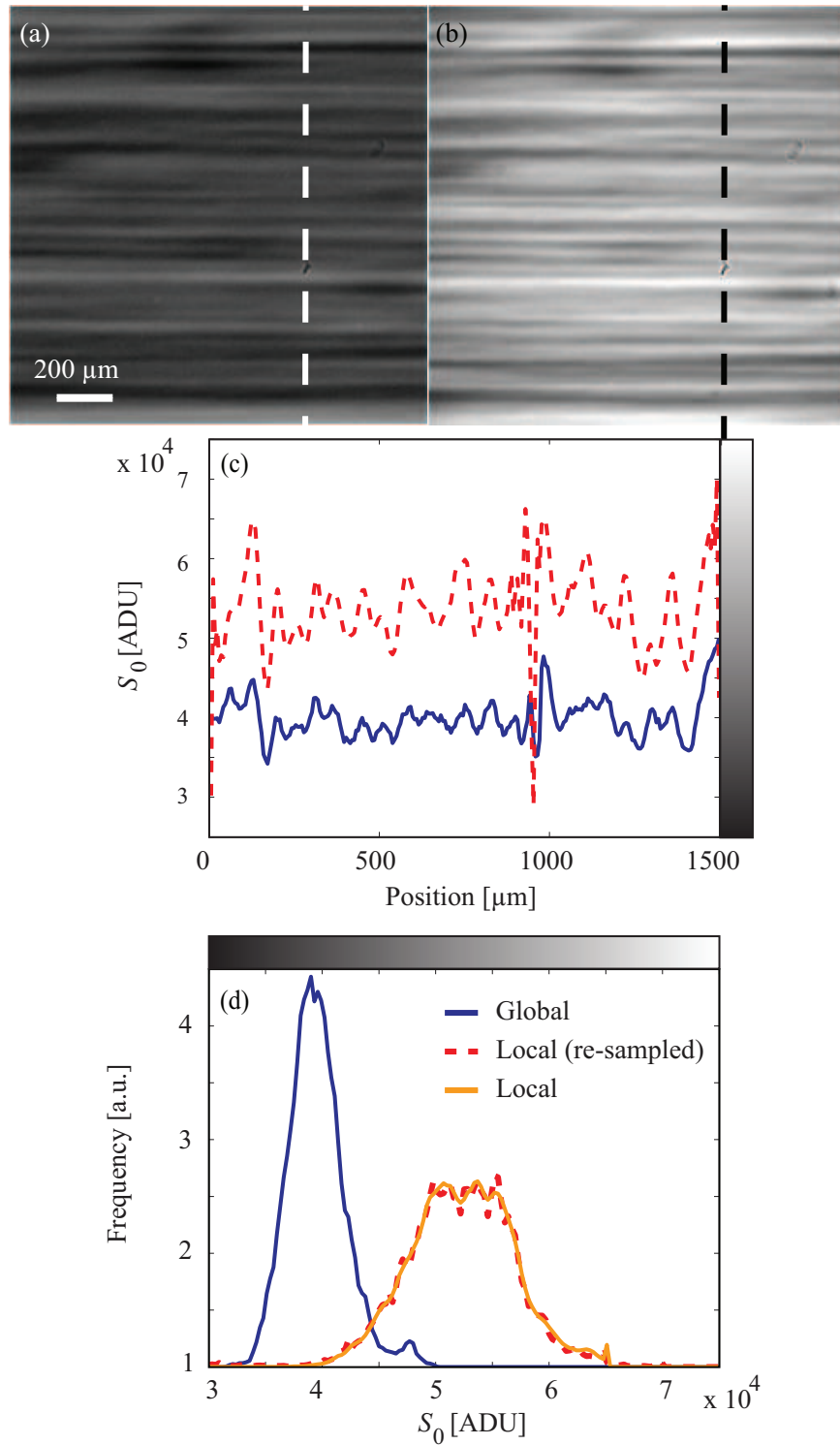


Figure 3.5: The flat-field images with low-magnifying objective, pixel size $5.92 \mu\text{m}$ and high-magnifying objective, pixel size $8.11 \times 0.74 \mu\text{m}$ reveal an intensity ratio according to the numerical apertures by 0.7 which is close to the expected value $66/100$.

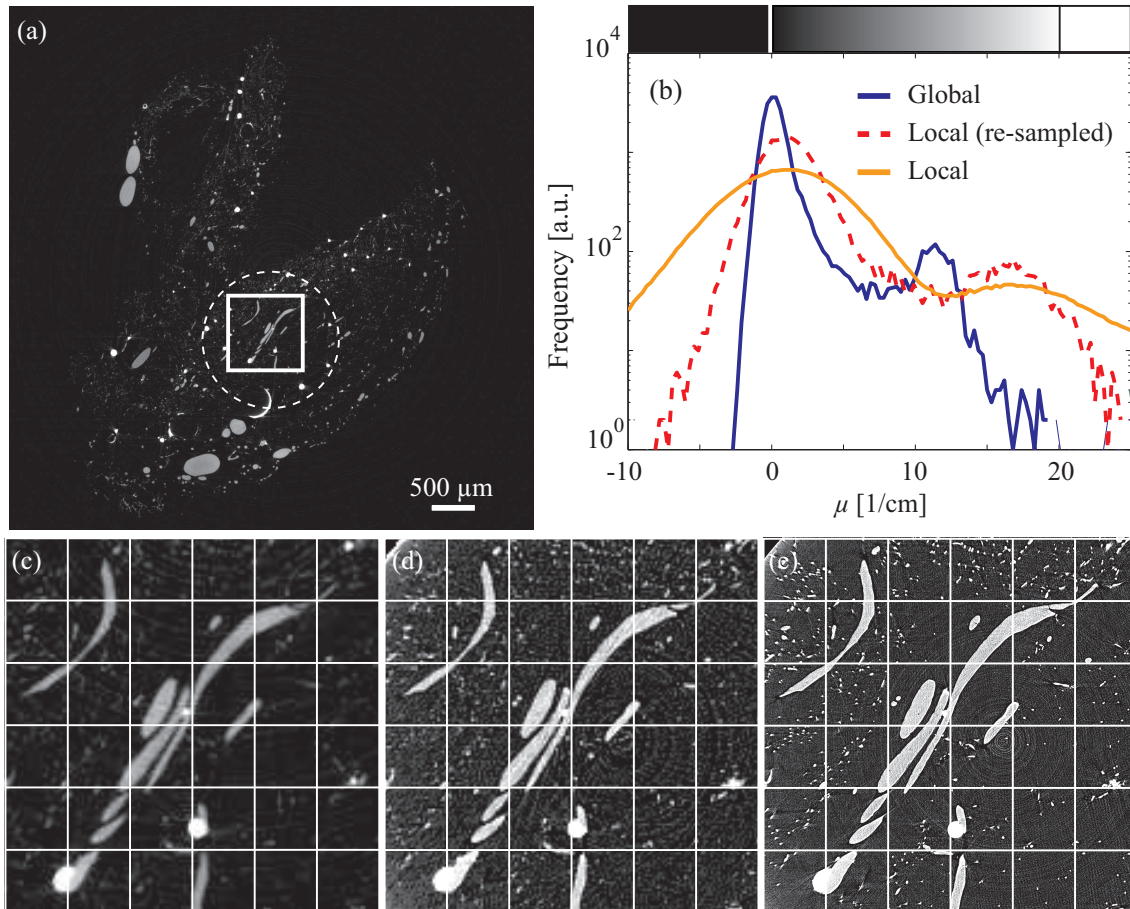


Figure 3.6: The tomography slice (a) is globally acquired and shows a virtual cut through the entire tumor. The dashed circle encloses the locally acquired tomogram. The full line rectangle corresponds to the cropped area (c) the tomography slice of the local tomography, re-sampled using the factor 8.11 (d) and with the high spatial resolution (e). The related histograms of the slices (b) show the massive influence of the different analytical methods on the local X-ray absorption coefficients.

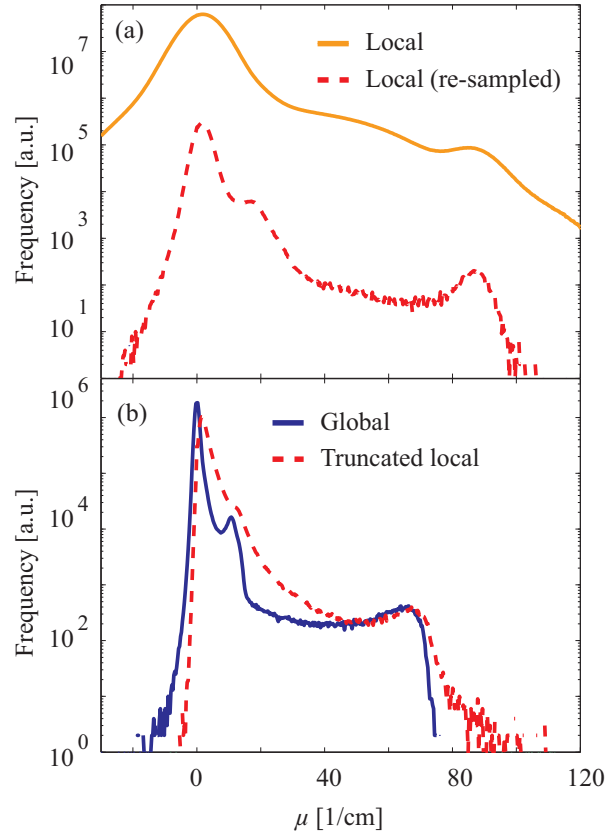


Figure 3.7: The diagrams show the histograms of the 3D data: (a) the influence of re-sampling the local data using the factor 8.11; (b) cropping globally acquired data before and after reconstruction - red-colored dashed and blue-colored full line, respectively. Three peaks can be identified in the 3D histograms which are related to air, polymer and bone for increasing order.

histograms of the radiographs exhibit just one peak of different FWHM. To equate the FWHM of the re-sampled local data to that of the global histogram, the intensity values for every locally acquired and re-sampled radiograph $I(x, y)$ is corrected using the difference between the most frequently occurring intensity value in the global projection and in the local projection D , and the ratio of the FWHMs R :

$$I_{HM}(x, y) = R[I(x, y) - 1] - D \quad (3.5)$$

Based on the corrected radiographs $I_{HM}(x, y)$, tomograms were reconstructed and their histograms compared with the histograms of the original datasets. As displayed in Figure 3.8, this histogram matching procedure of the locally acquired data causes a significant peak sharpening and peak shifts to more reliable absorption coefficients. The sharpening in the histograms of the radiographs by 35% reduces the FWHM of the air peak by 25% for the local, re-sampled tomogram and 33% for the local tomogram. Nonetheless, the air-related peak in the corrected histograms is still well above zero.

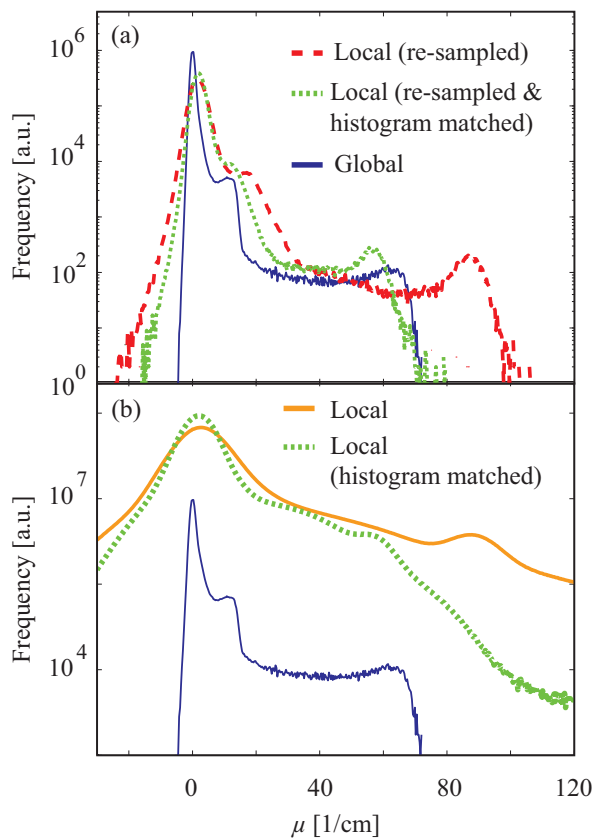


Figure 3.8: *Correcting local radiographs using histogram matching: (a) histograms of re-sampled tomography data and (b) histogram of high-resolution tomography data.*

3.3.6 Extending Local Sinograms by Less Detailed Global Data

In order to complete the local projections, one may take advantage of the less detailed global projections. Because the local and global projections have different pixel sizes, the local projections were down-sampled using the factor of 8.11. The regions in the global projections showing the identical regions visible in the local ones were replaced by the down-sampled local projections with a precision in pixel size of $5.92 \mu\text{m}$. Figure 3.9 (a) shows the comparison of the histograms of the tomography data with and without such an extension. The extensions of the re-sampled local projections by the less detailed global ones lead to a slight shift to smaller absorption coefficients. Alternatively, one can up-sample the global projections to fit the pixel size of the local data. This approach, however, yields huge datasets. Figure 3.9 (b), therefore, shows the histograms of only one tomography slice. Again, the extension slightly shifts the peaks to more reasonable X-ray absorption coefficients. Unfortunately, it coincides with a significant broadening of the peaks.

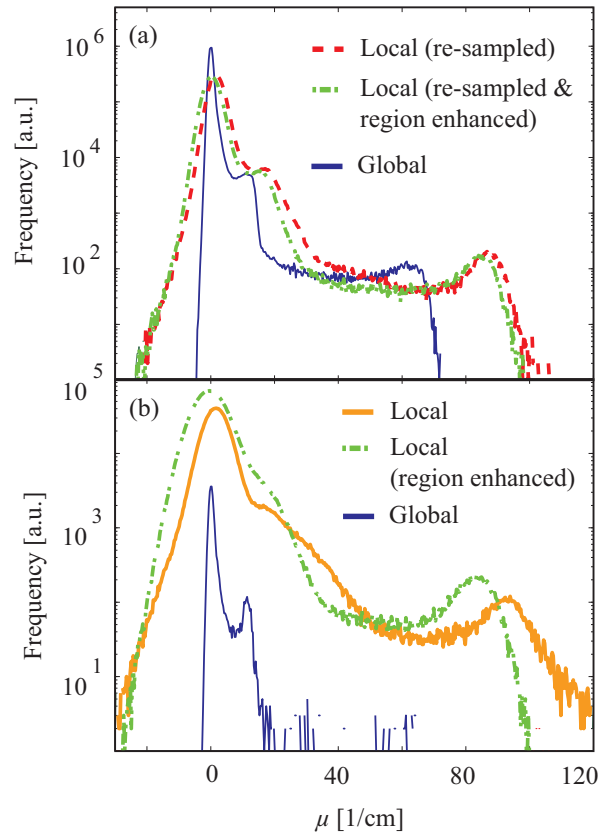


Figure 3.9: *Extending local sinograms by less detailed global data: (a) histogram of re-sampled tomography data and (b) histograms of high-resolution tomography data.*

3.3.7 Empirical Cupping Correction

Cupping artifacts occur in cone-beam CT and result from beam hardening [1]. Although the origin of beam hardening is quite different, similar behavior could be identified in the

local tomograms presented here (cp. Figure 3.10 (a)). It was communicated [67,68] that the absorption peaks shift to larger absorption coefficients from the rotation center to periphery. Thus, the tomogram was divided into eight concentric sub-domains of identical area as illustrated for one slice in Figure 3.10. For each of the color-coded 3D subunits the histogram is plotted. The air peaks show larger shifts to higher X-ray absorption coefficients for larger distance to the center of the local tomogram. Although this order is not found for the bone peak, absorption coefficient shifts for the different distances to the rotation center have been observed as well. These peak shifts were applied for an empirical cupping correction of the tomography data, which might also be termed 'de-cupping'.

The correction of the histograms includes two components. First, the shift of the air-related peak present in the data of the eight subunits (cp. Figure 3.10 (a)) was applied as individual constant for each subunit to guarantee that the air peaks have their maxima at zero absorption. This procedure, however, shows a nonlinear dependence on the distance to rotation center so that a cubic spline interpolation of the Matlab R2010a code has been applied to achieve a gradual change from center to periphery. Second, the absorption coefficients in the locally acquired data were compressed adapting the peak distances between air and Os-loaded bone to the values of the global tomogram to obtain the bone-related maximum at the desired absorption coefficient.

The resulted histogram is displayed in Figure 3.10 (b). Such an empirical de-cupping, however, only reduces the FWHM of the air peak by 20% and the three peaks are still much broader than the peaks in the global data. While the peaks for air and Os-loaded bone are forced to the absorption coefficients of the global tomogram, the Os-loaded polyurethane peak prominent in the global data is missing in the histograms of the high-resolution data.

3.3.8 Tumor Vessel System

The software VG Studio MAX 2.0 (Volume Graphics, Heidelberg, Germany) served for the visualization of the tumor vessels. Figure 3.11 represents 3D tumor vessel images of global and local data, respectively. The high-resolution tomography data were corrected using histogram matching to apply a well comparable threshold for the two images. The high-resolution local data reveal the small capillaries, whereas the global data merely show a non-uniform background. In the majority of cases, however, the authors show images with individually adapted thresholds to avoid such a background and to better highlight certain features. The Os-loaded bone leftovers, for example, are clearer visible in Figure 3.12. The direct comparison of the global with the histogram-matched local tomography data demonstrates that the vast majority of the small capillaries with diameters between 3 to 15 μm are missing in the image of the global data.

3.4 Discussion

Local tomography provides useful 3D images with a lot of details, but the absorption coefficients obtained from a simple tomographic reconstruction of local tomography data are usually inconsistent with global data, i.e., data in which the detector field covers the full width of the specimen. Against that, the global data are generally less detailed. Therefore, in multi-scale studies, it seems attractive to correct the local tomography data by means of the global data. In the present study three empirical approaches were evaluated, i.e. two parameter histogram

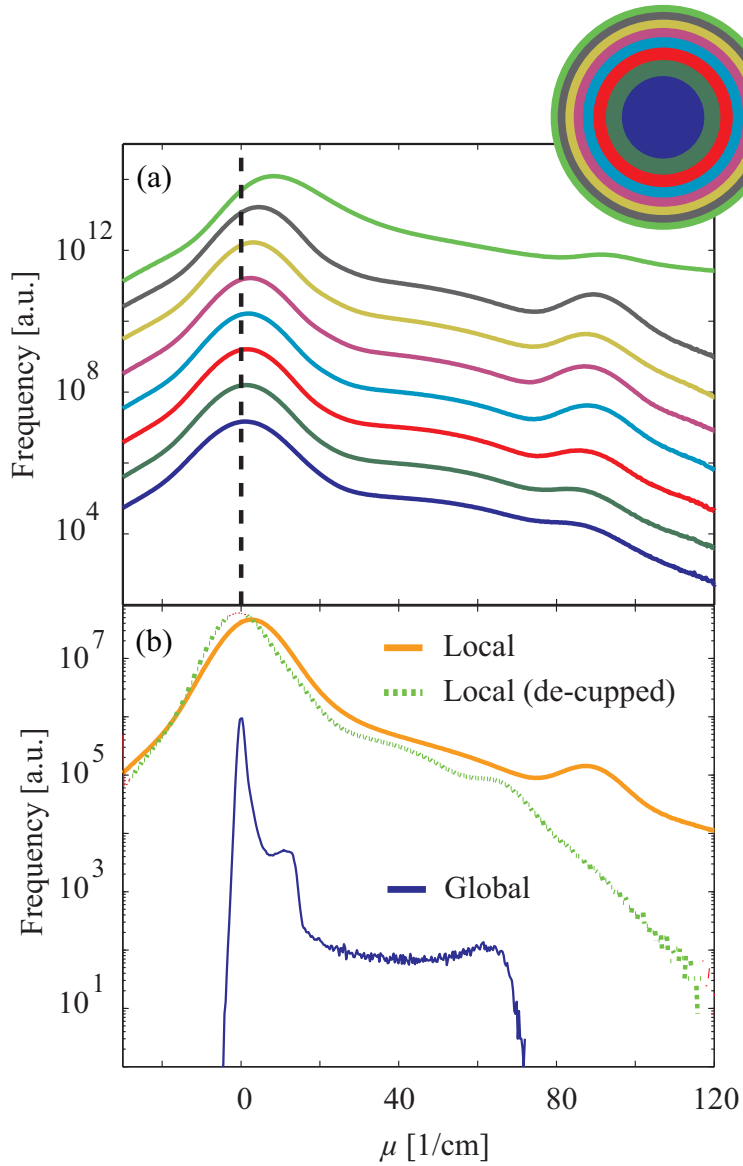


Figure 3.10: *Empirical cupping correction of tomography data: (a) histograms of color-coded regions with the same number of voxels; (b) histogram modification as the results of cupping correction by means of the air peak shift.*

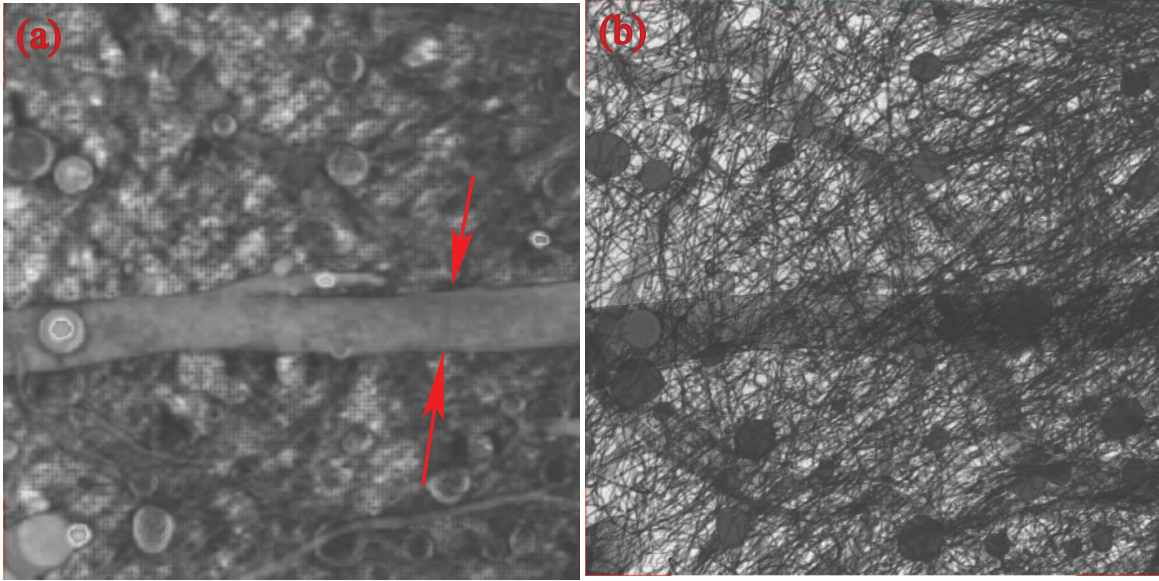


Figure 3.11: Comparing globally (a) and locally (b) acquired 3D representations of the tumor vessel system. The histogram matching of the locally acquired data allows choosing an equivalent threshold for the local data showing a network of small capillaries and for the global data exhibiting a non-uniform background.

Table 3.1: Selected parameters of the histogram analysis.

	Position of the Air-peak (1/cm)	FWHM of the Air-peak (1/cm)	Distance between Air- Bone-peak (1/cm)
Global tomogram	0.00 ± 0.00	0.52 ± 0.00	61.7 ± 0.2
Local tomogram	2.74 ± 0.02	5.85 ± 0.02	84.5 ± 0.3
Global tomogram from incomplete data	1.27 ± 0.02	0.89 ± 0.02	63.5 ± 0.3
Re-sampled local tomogram	2.56 ± 0.05	5.71 ± 0.02	84.6 ± 0.4
Local tomogram after de-cupping	0.54 ± 0.03	4.33 ± 0.03	66.9 ± 0.5
Re-sampled, histogram matched local tomogram	1.68 ± 0.02	1.51 ± 0.02	54.9 ± 0.5
Histogram matched local tomogram	1.91 ± 0.02	3.90 ± 0.02	54.6 ± 0.3
Re-sampled local tomogram with missing data	0.27 ± 0.01	2.18 ± 0.01	85.0 ± 0.1
Local tomogram with missing data	0.31 ± 0.02	4.90 ± 0.02	83.2 ± 0.4

matching, sinogram extension, and multi-parameter cupping correction, to identify an effective procedure for correcting the local X-ray absorption coefficients in local tomography data. The discrepancies between the X-ray absorption coefficients obtained from the local and the global data is, at least partly, due to systematic artifacts, often termed bias, in the local data that result from the fact that the locally acquired projections are truncated [69,70]. However, differences in the response functions of the detector configurations used for the acquisitions can be an additional source of discrepancy. Before a direct comparison between local and global tomography, the potential influence of the detector optics should therefore be analyzed and suitable registration algorithms with voxel precision have to be employed.

The flat-field images recorded with the objectives 1.25x (NA 0.04) and 10x (NA 0.4) exhibit different brightness. As the numerical aperture differs by a factor of 10 and the magnification only by a factor of 8.11, an average signal ratio between the global and the local data of $(8.11/10)^2 = 0.66$ should be expected. This matches the experimentally observed ratio of around 0.7. In any case, this effect should only enter into the statistical noise properties, not into the systematic shift of the reconstructed absorption coefficients, because the radiographs of both datasets were corrected in the conventional manner by subtraction of dark images and normalization to flat-field images taken with the object removed from the beam. The observed maximal intensity for the re-sampled flat-field images exceeds the limited detector read-out of 16-bit by 9.3%. These high values is not related to over-saturation of the detector during acquisition but caused by re-sampling phenomena.

The rigid registration between the global and re-sampled local radiographs resulted in errors of sub-pixel magnitude. These remaining errors, however, cannot explain the significant discrepancies between the values of global and re-sampled local radiographs, as clearly identified in the images of Figure 3.3 and 3.4. While a quantitative explanation of this phenomenon is beyond the scope of this study, one could attribute the broader histogram of the locally acquired data with respect to the globally acquired ones mainly to the differences in the point spread function of the imaging system [71], especially to the tails in this function. This is because other possible contributions are canceled out by the re-sampling of the high-resolution data to the larger pixel size of the global data. The effects, which the re-sampling procedure eliminates (or drastically reduces), include, in particular, any differences due to the presence of edge-enhancing phase contrast fringes in the high-resolution data, as well as the different statistical properties of the two datasets in so far as they are directly caused by the different pixel sizes of the data. The registration procedure of the radiographs reveals that the agreement between the global and local images is significantly better, if the global projections are shifted by two or three angular steps θ of the specimen rotation (each step 0.12°) with respect to the local projections. The more reliable 3D-registration procedure of the tomograms corroborates this observation. The related rotation parameter corresponds to $\theta = 0.31^\circ$, whereas no rotational misalignment in the perpendicular directions has been found. Hence, the not exactly adjusted rotation angle gives rise to a misalignment of 0.05° from the third angular step ($\theta = 0.36^\circ$). For the tumor, this angular misalignment may cause errors in intensity of about 1%, but contributes only in negligible manner to the discrepancies in the histograms mentioned above also because the detector is assumed to work in the linear domain [61]. Corrections of systematic errors as proposed by [72] cannot be applied, since the exact composition of the specimen is unknown.

One could presume that another source of error may lie in deformations of the highly elastic specimen during the data acquisition. The visible deformation in the projections (see

Figure 3.3 (e)) however corresponds to only 1.2? and can therefore be neglected. In order to exclude any noteworthy deformation during data recording, affine registration including global shearing and variable scaling parameters in the orthogonal directions has been carried out [63]. These calculations have not given any indication for such deformations. Therefore, it can be concluded that the specimen has not changed its shape and relative movement artifacts can be excluded.

The registrations of the radiographs and of the tomograms make available the scaling parameters in the orthogonal directions between global and local data, which correspond to 8.11 (± 0.02). This value is only slightly higher than the nominal one given by the supplier of the objectives [71,73]. Variations between the three orthogonal directions of maximal 0.02 are well below the pixel size of the global data. The absorption histograms of the common volumes of globally and locally acquired data strongly differ concerning absolute and relative peak positions and half widths. The partial volume effects, much stronger in the global tomograms [74] and the edge enhancement, more clearly visible in the local tomograms [65,75,76] can notably influence the histograms and explain the main discrepancies between the histograms before re-sampling or binning. As the re-sampling with a factor of about eight equals an averaging, these two effects should be of minor importance comparing the global and the re-sampled local absorption histograms of common volumes. Binning, which corresponds to the use of a large re-sampling factor (here about eight), especially carried out prior reconstruction, significantly sharpens the peaks and thereby improves the contrast (density resolution) [65]. The comparison of the histograms obtained from the high-resolution data with the re-sampled local histograms confirms this earlier result.

While the air peak of the global tomography data is detected at X-ray absorption coefficients close to zero (cp. Table 3.1), the air peak of the local data is located at about 2.8 cm⁻¹. A shift to higher X-ray absorption (1.3 cm⁻¹) is also observed if the global data are restricted to the common region with the local radiography for reconstruction. Therefore, in agreement with the literature [1], this shift is regarded as an artifact due to the local acquisition geometry.

Peak broadening in 3D data histograms may originate from minor peak shifts from slice to slice. One of the reasons for these shifts can be the photon energy gradient in X-ray beams from multilayer monochromators. However, in the present case this phenomenon can be excluded as the effect is absent within the global tomogram. For the local data, however, the air peak position scatters around the mean value of 2.76 cm⁻¹ by 0.84 cm⁻¹. Correcting this scattering from slice-to-slice, the FWHM of the air peak does not diminish remarkably (only 0.7%).

In order to reduce the artifacts related to the truncation of the local projections, it seems to be straightforward to complement the local radiographs (or, equivalently, the sinograms) by the less detailed global data that was previously described as zoom-in tomography [77]. For the datasets in the present study, however, the results of this approach, given in Figure 3.9, are rather disappointing. The peak positions of polymer and bone in the extended local data are only slightly shifted and still far from the peaks derived from the global tomogram. This observation is in quantitative agreement with the simulations and experimental data of Xiao et al. [77]. The error estimated on the basis of this approach corresponds to a reduction by 11%, which fits our result of 14%. Therefore, this approach only supports the correction of the air-related peak. The observation that the sinogram extension approach does not yield satisfactory results, and does not have as much effect on the data as would be needed to match the histograms, constitutes strong evidence that, for the present dataset, the mismatch

in reconstructed absorption coefficients between the local and global data is not primarily due to the typical local-tomography artifacts. Since, in addition, almost all experimental parameters were the same in the acquisition of both datasets, with the only major exception of the detector configurations used in both datasets, one can conclude that the discrepancies are primarily caused by differences in the detector response functions.

Among the model-independent approaches, histogram matching belongs to the powerful methods to match the data. However, conventional histogram matching is rather difficult for tomography data because of their size, especially since the number of voxels in the common volume differs between the global and local data by a factor of 535. Therefore, the approach of histogram matching of the radiographs prior to reconstruction was chosen. Because the intensity histogram of the global data (cp. Figure 3.4 (a)) exhibits discontinuities, the conventional histogram matching procedure has been replaced by a two-parameter approach to generate a distribution with comparable peak position and half width. This approach does not provide perfect agreement, but much better results than the sinogram extension. Evaluating the graphs in Figure 3.8 (a), it has to be stated that this histogram matching does not yet yield reliable local X-ray absorption coefficients. Therefore, the two-parameter histogram matching of the radiographs is considered to be rather an empirical method. It also may depend on the choice of specimen. In the present example, however, it can be applied to determine a common threshold for the direct comparison of global and local tomography images.

3.5 Conclusion

Local tomography is a powerful technique to generate 3D pictures of small features in a larger specimen that exhibit a strong X-ray absorption difference compared to their surroundings. The local X-ray absorption coefficients derived from local tomography, however, are only semi-quantitative even after applying correction procedures.

For the two datasets investigated here, the findings from the different approaches used to match the reconstructed values of absorption coefficients, together with the comparison of equivalent regions in the projection data (Figure 3.4 (b)), brought us to the conclusion that the differences observed in the reconstructed X-ray absorption coefficients in the tomograms are predominantly due to different point-spread functions of the two detector configurations used resulting from the exchange of the lens in front of the camera, and much less to the fact that one of the datasets was acquired in a local geometry. In the present case, a simple histogram stretching method therefore yielded better results to match the reconstructed values than, for example, sinogram extension of the local data by the global dataset.

Generally, our study shows that, when attempting to match datasets from multi-scale tomography measurements, experimentalists should not only consider the well-known phenomenon of the shift of the reconstructed values due to local acquisition geometries, but also potential differences due to other factors, such as different response of the detector configurations used. Beyond the present study, the question in how far the absorption coefficients obtained by SR μ CT - even those obtained in global geometry - are quantitatively correct depends on how much the detector response function, in each individual case, affects the measured I/I_0 values in the normalized projections. For cases where these effects are not negligible, and where quantitatively correct absorption values are needed, well-defined and effective calibration pro-

protocols may have to be established.

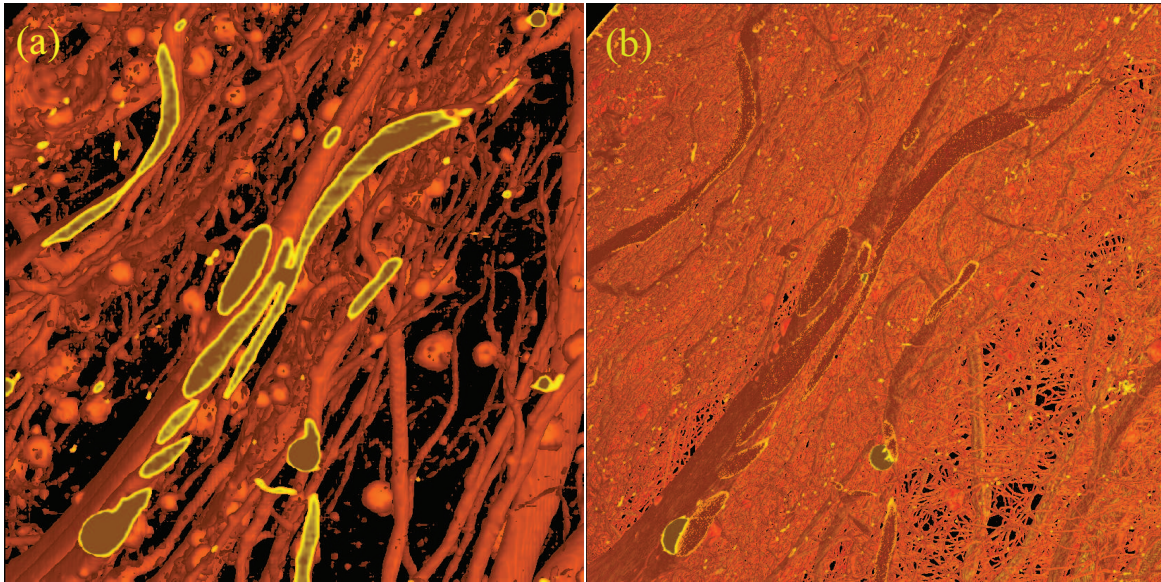


Figure 3.12: *Using different thresholds for global and local data, the dense network of smaller capillaries seen in the histogram matched local data (b) can become completely invisible in the global data (a)*

Chapter 4

Comparing Grating-based and Propagation-based Phase-contrast Computed Tomography for Soft Tissue Imaging

4.1 Introduction

The common methods for microscopic investigation of soft tissues of human and animal origin are optical microscopy, including histology, and high-resolution magnetic resonance imaging (MRI). MRI has the advantage of being compatible with in-vivo studies and yielding 3D images, but its spatial resolution is limited to approximately $80\ \mu\text{m}$ [42]. Optical microscopy of histological sections reaches much better lateral spatial resolution but here the specimen has to be cut irreversibly into thin slices. This means that sectioning is essentially a 2D method. It usually requires invasive preparation procedures that involve fixation, dehydration or freezing, and embedding. These time-consuming processes often cause local stress and strain within the inhomogeneous soft tissues [78]. The related local deformations can be corrected by means of less detailed X-ray micro computed tomography (μCT) data. True micrometer resolution μCT , however, is incompatible with in-vivo studies because of the high X-ray dose deposited in the investigated object. However, on extracted tissue, it yields high-resolution 3D data of the specimen morphology. Unfortunately, the composition and density variations in soft tissue specimens only result in weak X-ray absorption contrast. This is particularly critical for high spatial resolution because the contrast further decreases as the features get smaller. Contrast-enhancing techniques like staining with contrast agents or corrosion casts can be used [21], but there are tissues for which these techniques are known to fail, e.g., tumours in the final stage [42]. An efficient alternative to X-ray absorption contrast μCT in studying soft tissues is μCT in phase contrast mode. In X-ray phase contrast methods, refraction and/or diffraction of X rays on interfaces or density modulations within the specimen generate image signal, rather than only the X-ray absorption. The exact mechanism varies from technique to technique. Common phase contrast methods include crystal interferometry [79, 80] analyzer-based imaging [81, 82], propagation-based imaging (PBI) [75, 83, 84] and, more recently, X-ray grating interferometry (GIFM) [31, 39, 40] as well as related other grating-based methods [85].

These methods differ greatly in their experimental setup and in the signal they provide, but they have in common that the signal is related to variations in the of X-ray refractive index within the object under study. Absorption and refraction of X rays in matter can be described by means of the complex refractive index n , which is defined as

$$n(x, y, z) = 1 - \delta(x, y, z) + i\beta(x, y, z). \quad (4.1)$$

Here, the decrement δ describes refraction, whereas the imaginary part β describes absorption. Both δ and β are dimensionless real-valued quantities and depend on the X-ray wavelength and on the elemental composition and density of the medium. In conventional X-ray absorption-contrast imaging, the image signal is usually the transmitted intensity,

$$I(x, y) = I_0 \exp \left[-\frac{4\pi}{\lambda} \int \beta(x, y, z) dz \right], \quad (4.2)$$

where I_0 is the incident intensity and z the beam propagation direction. A tomographic reconstruction of $(-\ln I/I_0)$ yields the distribution of linear attenuation coefficient μ , which is linked to β by the relationship $\mu = 4\pi\beta/\lambda$. For hard X rays, both δ and β are many orders of magnitude smaller than unity for all materials, which reflects the weak refraction and attenuation of the radiation when it passes through matter. For X-ray photon energies above 10 keV, however, the values of δ for light materials, such as water and soft tissue, are much higher than the values of β . Therefore, generating contrast from variations in δ can drastically improve the contrast-to-noise ratio. Methods that use this principle are called "X-ray phase contrast" methods. However, the image signal in X-ray phase contrast is generally not related to δ as a simple line integral, and it strongly depends on setup and data analysis algorithm. Tomographic retrieval of $\delta(x, y, z)$ from phase-contrast images therefore requires an additional data processing step: the reconstruction of the phase projection image $\varphi(x, y)$ from the images recorded by the detector. Since the wavefront phase φ and the refractive index decrement δ are related by

$$\varphi(x, y) = \frac{2\pi}{\lambda} \left[\int \delta(x, y, z) dz \right], \quad (4.3)$$

a tomographic reconstruction of the integrated image then yields the distribution of δ . The algorithm used to obtain $\varphi(x, y)$ from the experimentally recorded images, known as "phase retrieval", strongly depends on the experimental setup, the physical model and the approximations used. In the following, the term "phase tomography" was used to refer to the combined process of data acquisition, phase retrieval and tomographic reconstruction, or its results. In the present study a tumor from human cells grown in nude mouse and a heart from a rat are selected to quantitatively compare three phase tomography methods: X-ray grating interferometry [31] and two propagation-based methods: holotomography [86,87] and single-distance phase tomography using Paganin's method [36,45]. The sensitivity and resulted contrast as well as the spatial resolution were discussed with the aim to elucidate the performance properties of each of the three methods for the imaging of selected biological tissues.

4.2 Material and Methods

4.2.1 Specimen preparation

Balb/c nude mice (Charles River Laboratories, France) were used to obtain the tumor specimen, in strict adherence to the Swiss law from animal protection. A suspension of 10^6 C51 tumor cells (murine colon carcinoma) was injected subcutaneously on the left flank of each animal. Extraction of the grown tumors took place at the Institute for Biomedical Engineering (ETH, Zurich) before they had reached a diameter of 3 mm. Immediately after extraction the specimens were fixed in 5% para-formaldehyde (para-formealdehyde) to avoid decomposition. To reduce bubble formation during the experiment, which is a frequent phenomenon in μ CT with spatial resolution in the micrometer range, the immersed tumor samples were put in a desiccator for 12 hours at a pressure of 5 mbar. After this degassing procedure the specimens were transferred into polymer pipette tips for the measurements. The heart specimen was obtained from a male Fischer rat (Charles River Laboratories, L'Arbresle, France). The specimen did not show any pathological sign. After extraction, it was immersed in 10% para-formealdehyde solution. All operative procedures related to animal care were carried out at the ESRF and strictly conformed to the Guidelines of the French Government (licenses 380825 and B3818510002). For the experiment, the heart was placed in a plastic tube 11 mm in diameter.

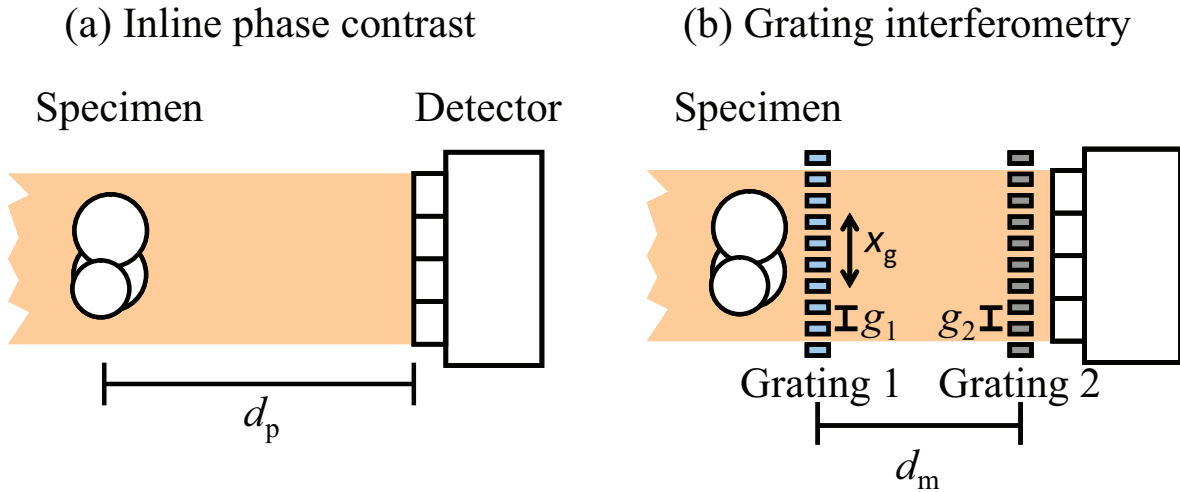


Figure 4.1: *Setup schemes for (a) propagation-based and (b) grating-based phase contrast as used in the present study.*

4.2.2 Data acquisition and processing

Both tumor and heart were investigated with grating-based tomography, holotomography, and single-distance phase tomography using Paganin's algorithm. The two latter methods are both propagation-based; they were performed on the same experimental raw data. The main differences in setup parameters between the two specimens were the spatial resolution and the field of view. The experiments were carried out at the ID19 beamline at the European Synchrotron Radiation Facility (ESRF, Grenoble, France). The technical details of

the beamline at the time of the experiment are described elsewhere [88]. The detector configurations for all measurements were indirect CCD-based systems, i.e., the X-ray intensity profile was converted to visible light by a scintillator screen, and the visible-light image was then projected onto the CCD sensor by lens optics. Table 1 summarizes the key experimental parameters for the measurements.

For the tumor measurements, the detector setup consisted of a 19- μm -thick gadolinium gallium garnet (GGG, $\text{Gd}_3\text{Ga}_5\text{O}_{12}$) scintillator, microscope optics with a $4\times$ objective (numerical aperture [NA] 0.16), and a $2.5\times$ eyepiece. The CCD-based digital detector was an ESRF FReLoN camera (model 230-42, 2048×2048 pixels of $15\ \mu\text{m}$ size). The pixels were binned 2×2 , resulting in an effective grid of 1024×1024 pixels with a pixel size of $3\ \mu\text{m}$. A photon energy of 17.6 keV was selected from the spectrum of an undulator source by Bragg reflection on a multilayer (Ru/B4C, period 4 nm).

For the measurements on the rat heart, a powder scintillator and $2\times$ magnifying lens optics were used with two different detector heads: a FReLoN model 230-42 (see above) for grating interferometry and a FReLoN model TH7899 (2048×2048 pixels of $14\ \mu\text{m}$ size) for the propagation-based imaging, resulting in effective pixel sizes of 8.0 and $7.5\ \mu\text{m}$, respectively, for grating interferometry and propagation-based imaging. A wiggler was used as a source, and a photon energy of 19 keV selected with a double-crystal Bragg monochromator (Si-111).

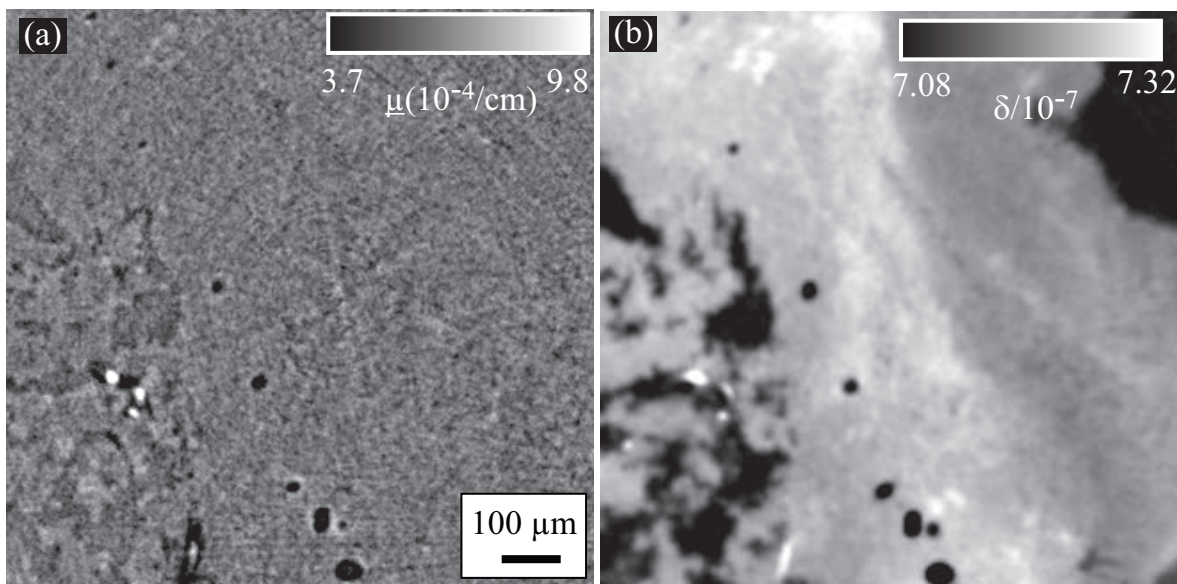


Figure 4.2: *Tomographic slices of the tumor sample measured with an interferometer at the beamline ID19 (European Synchrotron Facility, France). Gray values are determined according to the mean value (a) and phase difference (b) in the intensity oscillation.*

Grating interferometry (GIFM)

In X-ray grating interferometry the phase shift of the photon beam transmitted through the specimen is measured using a phase grating G1 and an absorption grating G2. Figure 4.1 (b) shows the setup of a grating interferometer schematically. G1 and G2 are line gratings.

Grid G1 acts as a diffractive element which induces a periodic modulation in the wavefront. Downstream of G1, this modulation leads to an interference pattern with a period g_s . In the experiments reported here, the incident wavefront was nearly plane and grating lines had a thickness that was designed to result in a phase shift of π in the wavefront at the selected photon energy. In this case, the period g_s of the interference pattern is half of the pitch g_1 of G1. The visibility of the interference fringes varies as a function of distance behind the grating and reaches maximum values at distances [89]

$$d_m = m \frac{g_1^2}{8\lambda} \quad (m = 1, 3, 5, \dots). \quad (4.4)$$

The distances d_m are called fractional Talbot distances or Lohmann distances. In the following one shall refer to the index m as the Talbot order and to d_m as the m -th fractional Talbot distance.

The analyzer grating G2 is placed downstream of G1 at one of the fractional Talbot distances defined by Equation (4.4). The lines of G2 should be as absorbing as possible, and its period g_2 should be designed to be the same as the period of the interference pattern generated by G1. Grating G2 works as a transmission mask and encodes fringe position into intensity of the detector [31]. G2 is needed because fringe spacing and displacement are usually too small to be resolved directly by the detector.

When an object is placed in the X-ray beam, the refraction caused by the object will result in a shift and/or distortion of the interference fringe pattern at the entrance plane of G2. The change in position of the fringes is proportional to the first lateral derivative of the projected phase profile of the specimen, and therefore its detection gives a differential phase contrast image. However, in the image recorded by the detector, this information is usually superimposed on the absorption signal from the specimen.

For separating the differential phase information from the absorption information, the phase stepping method can be used: one of the gratings G1 or G2 is laterally scanned in a few steps over one fringe period, in the direction orthogonal to the fringe orientation (and, thus, also orthogonal to the grating lines). This is an adaptation of the well-known general concept of phase shifting interferometry to the particular case of a grating interferometer. As a function of the position x_g of the scanned grating Figure 4.1, the intensity recorded in each pixel of the detector will oscillate. The phase Ψ of the measured intensity oscillation can easily be determined from the data, for example, by Fourier analysis. It is related to the X-ray phase shift φ by

$$\Psi(x, y) = \frac{\lambda d_m}{g_2} \frac{\partial \varphi(x, y)}{\partial x} \quad (4.5)$$

The experimentally obtained map of $\Psi(x, y)$ is called a differential phase contrast (DPC) image. It is obvious from equation (5) that the sensitivity of a grating interferometer to the phase gradient $\partial\varphi/\partial x$ increases with increasing inter-grating distance d_m (provided the spatial coherence of the X-ray beam is sufficient [89] and with decreasing grating period g_2 . It is also obvious that the phase profile $\varphi(x, y)$ can be retrieved from $\Psi(x, y)$ through a simple integration along the x coordinate of the image, as long as the boundary values $\varphi(0, y)$ are known for all positions y . This condition is usually met in tomography, unless the specimen is larger than the field of view. The 3D distribution of the decrement $\delta(x, y, z)$ of the refractive

index can be retrieved from $\varphi(x, y)$ by tomographic reconstruction, as is apparent from equation (3). In experimental practice, the object imaged (or the container holding the object) is often immersed in a phase-matching liquid in a tank with plane-parallel walls, to reduce the strong phase contrast from the object surface (or the container wall) that can create artifacts in the image. When immersion is used, it has to be taken into account that one obtains only the relative values $\Delta\delta = \delta - \delta_0$, where δ_0 is the decrement of refractive index of the immersion medium. Obviously, if the value of δ_0 is known, then it can be used as a reference to determine the absolute δ values. In addition to the DPC image, an absorption-contrast image can be obtained from the phase stepping scan data by simply calculating the mean value of each pixel over the oscillating intensity function.

The recovery of the DPC and the absorption image from the raw data was performed by a computer program written by the authors in the IDL language (Exelis, Boulder, CO, USA). This is the code routinely used at beamline ID19 for the processing of grating interferometry data.

Experimental parameters for GIFM on the tumor specimen: The interferometer used for the measurements on the tumor consisted of a silicon phase grating G1 with a pitch $g_1 = 4\mu\text{m}$ and a gold analyzer grating G2 with $g_2 = 2\mu\text{m}$ pitch. The gratings were separated by 140 mm, i.e., the 5th fractional Talbot distance (FTD) at the photon energy of 17.6 keV. Phase-stepping scans with 4 points were performed by stepping the grating G1 over one fringe period, i.e., over a range of $g_1/2$, at grating positions $x_gj = jp_1/8$ ($j = 0, 1, 2, 3$). The exposure time was 0.3 s per raw detector image for 359 projection angle intervals over 360° . Because of the strong phase gradient occurring between the edges of the sample container and the surrounding air, phase wrapping artifacts occur [90]. In the present study, these artifacts were eliminated by a procedure in which *a priori* information about the container (i.e., its chemical composition and its rotational symmetry) was used, together with geometric information obtained from the scan data, to model the phase profile of the container and replace the areas around the container edges in the differential phase contrast radiographs by modeled data, prior to tomographic reconstruction.

Experimental parameters for GIFM on the heart specimen: For the heart measurement the gratings had periods of $g_1 = 4.8\mu\text{m}$ and $g_2 = 2.4\mu\text{m}$. They were placed at a distance of $d_m = 482$ mm between one another (corresponding to $m = 11$, i.e., the eleventh FTD at 19 keV). Phase stepping was carried out by scanning grating G1 over one fringe period in 5 steps, with an exposure time of 1.5 s per raw image, for 1500 projections over 360° (i.e., 1499 angular intervals). A correction of phase wrapping effects was not necessary for these data because the measurements were carried out while the heart in its container was immersed in a tank filled with water, so that the phase gradient at the container walls was significantly reduced.

Holotomography

Holotomography [86] is based on phase contrast generated by the propagation of X rays in free space between specimen and detector. Compared to absorption-contrast imaging, the additional information needed to solve the phase problem is obtained by taking images at different propagation distances.

Because, at any propagation distance, the contrast transfer function (CTF) for phase contrast takes zero values for certain spatial frequencies, data sets for holotomography are usually

taken at more than two distances. In the present study, the propagation distances were chosen with a computer software tool that optimizes the overall squared CTF [35], using the photon energy and the detector resolution (expressed in terms of pixel size) as input parameters. This tool, named "ht_opti2" and written in the Octave programming language, is available to users at the beamline ID19 of ESRF. Additional constraints, such as the technically feasible minimum and maximum values of propagation distance, need to be taken into account. For the measurements on the tumor specimen, four distances were used in the holotomography experiment. The data were acquired at an initial pixel size of $1.5 \mu\text{m}$ of the detector and then binned to $3 \mu\text{m}$ pixel size by software. For the initial detector pixel size of $1.5 \mu\text{m}$, distances between specimen and detector of $d_p = 13, 60, 120, 360$ mm were determined. For each of these four distances, images were taken at 800 equidistant angles over a range of 180° , with an exposure time of 0.3 s per raw image. For the holotomographic phase retrieval and tomographic reconstruction, the data set acquired at 13 mm distance was excluded because it contained strong artifacts.

For the heart measurements, data were taken at five propagation distances within the technically accessible range: 200, 400, 700, 900 and 1100 mm. The exposure time was 1 s per raw image for 1500 projections over 360° . In these measurements, the accessible sample-detector distances were technically limited to 1.1 m by the travel range of the longitudinal motion stage on which the detector of the "medium-resolution" tomography setup at ID19 is mounted [88]. The data set acquired at 900 mm was not used for the holotomographic reconstruction because of a problem in the alignment of the images with those acquired at other distances.

The phase retrieval algorithm for holotomography at beamline ID19 is implemented in the Octave programming language. The user can choose between several algorithms proposed. For the present study, a mixed approach between the contrast transfer function (CTF) and the transport of intensity equation (TIE) [37, 87, 91] was chosen. While the calculation of the differential phase is based on TIE is less adapted for hard x rays (10-100 keV) [35], it is well suited for short propagation distances. The CTF approach, on the other hand, requires that objects have a slowly varying phase and weak absorption. The combined model has the advantage that it is valid for extended propagation distances as well as non-negligible absorption. To reduce low frequency artifacts, which can arise from the fact that the transfer function for phase contrast is always small in the low spatial frequency range, the low-frequency components of the phase profile are presumed to be proportional to the logarithm of the projected intensity transmission via a fixed estimated ratio δ/β of refractive index decrement over absorption coefficient [87]. In the present case, this a-priori input parameter was taken to be 1371, corresponding to the values of δ and β of water at 17.6 keV.

The phase retrieval algorithm for holotomography data contains a filter that performs a deconvolution of the image with the resolution-function of the detector. To obtain better insight in the influence of this filter on the image quality the holotomography data of the heart was processed additionally without the filter.

Single-distance phase retrieval

Under a set of simplifying assumptions, the phase profile $\varphi(x, y)$ of the X-ray wavefront at the exit plane of the specimen can be recovered from only a single radiograph in free-space propagation phase contrast, taken at a suitable distance between detector and specimen. In this case, it is not necessary to take radiographs at multiple distances as in holotomography.

Here a simple but powerful non-iterative algorithm was used presented by Paganin et al. [36], in a recent implementation in the Java computer language. This simple program, named ANKAphase [45], is freely available and can be run as a standalone application or as a plug in to the well-known software ImageJ.

There are essentially two conditions that should be met for Paganin’s algorithm to be valid. Firstly, the ratio δ/β of the decrement of refractive index δ over the absorption coefficient β should be constant throughout the specimen. While this implicitly allows for non-negligible absorption by the specimen (an advantage), it also means that the chemical composition of the specimen should vary only marginally within the object. It should be noted that, while the multi-distance holotomography approach presented above also assumes such a fixed ratio δ/β , it only uses this fixed ratio for the reconstruction of the low spatial frequencies. In single-distance phase retrieval, however, the assumption of such a fixed ratio should be expected to have much greater influence since it affects the whole frequency spectrum of the retrieved phase map, not only the low frequencies.

Secondly, Paganin’s algorithm requires that the approximation of the phase-contrast signal as being proportional to the Laplacian of the phase profile, $(\partial^2\varphi/\partial x^2 + \partial^2\varphi/\partial y^2)$, should be valid. This is a common point with the TIE approach in holotomography (from which Paganin’s method is derived), but not with the CTF approach. It implies that propagation distances are limited to $d_p \ll D^2/\lambda$, where d_p is the propagation distance, D the size of the smallest feature to be resolved in the object, and λ the X-ray wavelength.

The spatial resolution of the phase maps retrieved with Paganin’s algorithm is limited to $((\lambda d_p)^{0.5})$. This means that a trade off between spatial resolution (which improves with shorter d_p) and contrast (which increases with d_p) needs to be made - an additional minus compared with multi-distance holotomography techniques. Moreover, the spatial frequencies at which the contrast transfer function goes through zero will not be well reconstructed with a single-distance method (unless there is substantial absorption contrast at these frequencies). These limitations may be compensated by advantages that single-distance algorithms in general, and Paganin’s method in particular, have over multi-distance approaches. These advantages include the greatly reduced instrumental effort and time for data acquisition, owing to the fact that radiographic projections are only required from one distance, just as in a standard absorption-contrast measurement. In addition, the image registration steps required in holotomography data processing to merge the information from different distances are not needed when working with data from a single distance. Moreover, Paganin’s method essentially restricts the calculation effort for phase retrieval to two Fourier transforms of each radiographic projection and is therefore relatively fast.

In the present study, phase recovery and tomographic reconstruction using ANKAphase was performed for all data sets obtained by free-space propagation, in addition to the holotomographic reconstruction performed on the same data. Similar to the holotomography processing a constant ratio of $\delta/\beta = 1371$ was used for the tumor, and $\delta/\beta = 1546$ for the heart.

4.2.3 Tomographic reconstruction

After phase recovery, the tomographic reconstruction of most of the data was carried out using the program PyHST [62]. This software has been developed in-house at the ESRF and is used as the standard tomography reconstruction program for all user experiments at beamline ID19. PyHST uses the filtered back-projection (FBP) method with a standard ramp filter. In

Table 4.1: Key experimental parameters for the measurements.

	Tumor sample	Heart sample
Detector pixel size Δ_{pix}	3 μm	7.5 μm (PBI) 8 μm (GIFM)
X-ray photon energy E and wavelength λ	17.6 keV 0.704 \AA	19 keV 0.653 \AA
Monochromator	Multilayer Ru/B ₄ C, 4 nm period	Double crystal Si-111 (Bragg)
Propagation-based imaging (PBI)		
Propagation distances ^a d_p	(13), 60, 120, 360 mm	0.2, 0.4, 0.7, (0.9), 1.1 m
Grating interferometry (GIFM)		
Grating periods g_1	4 μm	4.8 μm
g_2	2 μm	2.4 μm
Talbot order m	5	11
Distance d_m between gratings	140 mm	482 mm

^aData taken at distances in brackets were not used for holotomography reconstruction.

particular, the filter used in this study does not apply any damping to high frequencies. Some of the data were tomographically reconstructed with code written in IDL, which implements the same principles (i.e., FBP and no high-frequency damping). For the differential phase contrast projection images from GIFM data, an imaginary sign filter, recently implemented in PyHST, was used instead of the ramp filter in the filtering step of the FBP procedure. Since all of the phase contrast methods used here are differential methods, i.e., the quantities measured have the characteristics of a derivative of the projected phase profile, an integration constant was added to each tomogram, to obtain absolute values of the decrement δ of refractive index. This constant was obtained, in each case, by shifting the histogram of the tomogram data so that the peak corresponding to the material surrounding the container corresponded to the literature value of δ for this surrounding material. For the PBI measurements, this material was air, with a value of $\delta_{\text{air}} = 7 \times 10^{-10}$. For the GIFM measurements, the material was demineralized water at room temperature. The literature value is $\delta_{\text{water}}(19\text{keV}) = 6.39 \times 10^7$.

4.2.4 Comparative analysis and quality assessment

To compare the quality of the images obtained by the different modalities, an analysis of their spatial resolution and density resolution as well as the presence of artifacts was carried out. For a detailed comparison between the methods for each specimen, equivalent regions of interest (ROIs) had to be identified. For the measurements of the heart this was trivial because the object had not been removed from its container between the data acquisition of interferometry and holotomography. The tumor sample, however, had been removed from its container between the two measurements to remove bubbles that had formed in the first measurement. It was therefore necessary to register the tomography volume images obtained

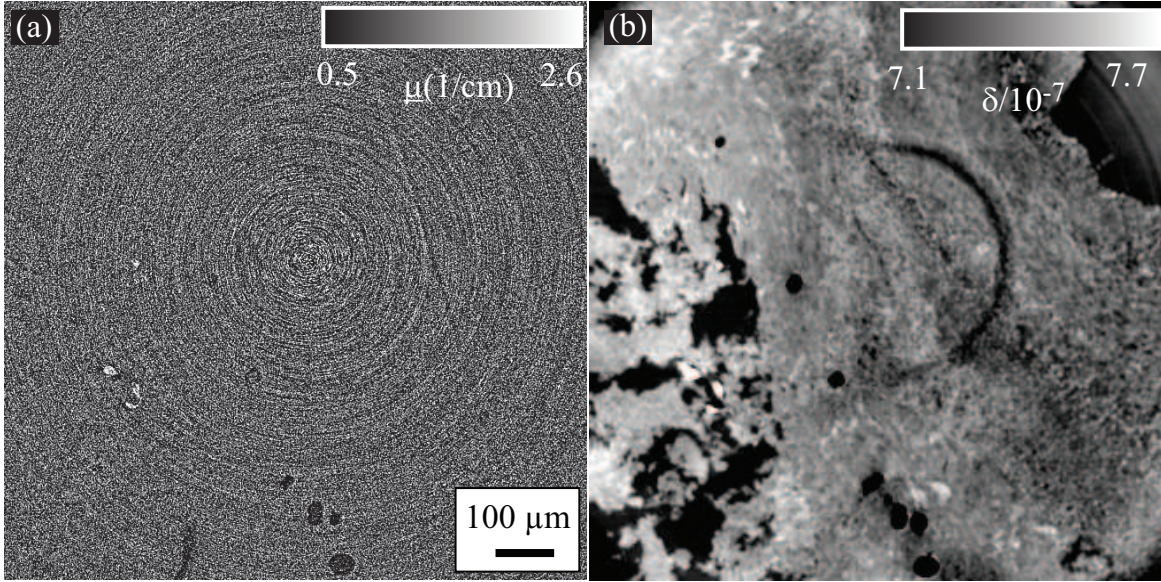


Figure 4.3: *Tomographic slices of the tumor sample measured with holotomography at the beamline ID19 (European Synchrotron Radiation Facility, France). The images were obtained with no-phase retrieval (a) at the detector-to-sample distance d_p of 13 mm and holotomography reconstruction (b).*

with free-space propagation with those from grating interferometry. Using a 3D registration tool [46] the calculated transformation parameters were used to transform the interferometer tomograms to match the ROI defined in the holotomography data.

As a measure of the spatial resolution in the tomograms, the radial spectral power function (RSP) was calculated for regions with strong structure and normalized by the RSP of a homogeneous area. The spatial resolution was estimated as the first observed frequency which is greater than twice the mean value of the baseline [92, 93].

For the analysis of the density resolution (CNR) the contrast-to-noise ratio [94]

$$CNR = \frac{|S_a - S_b|}{\sqrt{\sigma_a^2 + \sigma_b^2}} \quad (4.6)$$

was determined. In this equation, the quantities S_a and S_b are the mean values of two homogeneous ROIs a and b in the tomograms, representing two different materials. The quantities σ_a and σ_b denote the standard deviations of the values in these same two ROIs. The CNR was determined for different pairs of materials a and b , where b was always the PFA.

In addition to the CNR, the histograms of the presented tomographic slices were determined; they give additional information on the density resolution of the different imaging modalities. In the histograms, each ensemble of voxels representing a given material appears as a peak. While the integral area under the peak corresponds to the number of voxels corresponding to the material, the width of the peak - as expressed, for example, by its full width at half maximum (FWHM) - are a measure of the density resolution: the smaller the width of the peak, the higher the density resolution [65].

Finally, a qualitative analysis based on visual inspection and comparison of the tomograms obtained with the different methods was made. This analysis included such aspects as the visual distinction of different regions and the presence of noise and artifacts, such as ring artifacts, cupping or other low-frequency artifacts.

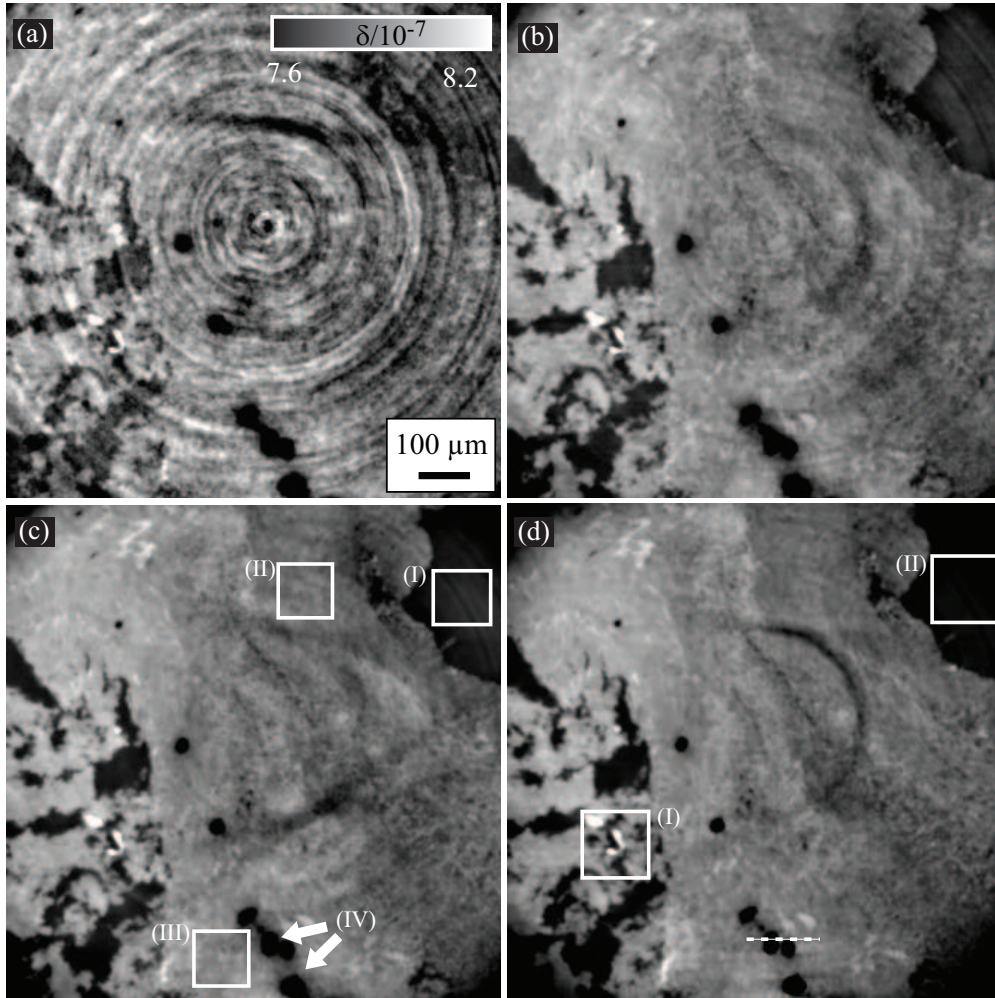


Figure 4.4: Tomographic slices of the tumor sample measured with one distance propagation based tomography (Paganin) at the beamline ID19 (European Synchrotron Radiation Facility, France). The images differ according to their sample-to-detector distance d_p by 13 mm (a), 120 mm (b), 180 mm (c) and 360 mm (d). For the features (II-dark tissue, III-bright tissue, IV-lipid) in (c) the CNR was calculated. Noise is represented by pixels belonging to PFA (I). Along the dashed line an image profile was made (4.10). The rectangles in (d) show the regions (I-full of features, II-background) which had been used to determine the RSP.

4.3 Results

The tomographic slices upon which all further analysis was based are shown in Figures 4.2 through 4.7. These figures show, for each imaging modality and phase-retrieval technique, one slice of each specimen. The positions of the slices in the entire volume data sets were selected for their wealth in relevant features. Clearly visible are the low-density spots (appearing in black), which are assumed to be lipid cells. In the GIFM image (see Figure 4.2) one can clearly distinguish between two different kind of soft tissue. Blood vessels can be seen as bright disordered spots. The dark background is the PFA. Figures 4.2, 4.3, 4.4 show data for the tumor measurements. Figure 4.2 shows GIFM data. The absorption tomogram Figure 4.2 (a) and the phase tomogram Figure 4.2 (b) were extracted from the same data. Figures 4.3 and 4.4 show images obtained from free-space propagation data. Figure 4.3 (a) is an absorption tomogram (i.e., no phase recovery was performed, and the data were treated as if they were pure absorption-contrast data), reconstructed from data taken at the smallest propagation distance realized (13 mm). Figure 4.3 (b) is a phase tomogram obtained by holotomography, and Figure 4.4 shows phase tomograms obtained by applying Paganin’s method to the data sets taken at different distances. Figures 4.5, 4.6, 4.7 show data for the heart measurements, arranged in the same order as the tumor data in Figures 4.2, 4.3, 4.4. The CNR analysis was performed on the ROIs marked in the panels Figures 4.4 and 4.7 (c). Its results are shown in Tables 4.2 and 4.3 for the tumor and the heart sample, respectively. The histograms of all slices shown in Figures 4.8 and 4.9.

The ROIs used for the RSP analysis of spatial resolution are marked by rectangles in Figures 4.4 (d) and 4.7 (d). The values of spatial resolution obtained from the RSP analysis are listed in Tables 4.2 and 4.3. The results show strong differences between the different methods. In addition, section profiles were taken at the positions marked by the dashed lines in Figures 4.4 (d) and 4.7 (d). These profiles are shown in Figures 4.10 and 4.11. The holotomography reconstruction procedure includes, by default, a deconvolution with an estimated detector resolution function to the projection data prior to the actual phase retrieval process. This is neither the case for the Paganin software used here (ANKAphase) nor for the software used to reconstruct the GIFM data. For comparison, an additional holotomography reconstruction of the heart data sets was performed, in which the deconvolution was deactivated. A comparison of the data obtained with and without the deconvolution is shown in Figure 4.15. The images differ in sharpness and in the overall reconstructed values of δ

4.4 Discussion

As should be expected, at the photon energies used, the specimens yield hardly any absorption contrast. This is apparent in the absorption-contrast tomograms, shown in Figures 4.2 (a), 4.3 (a), 4.5 (a) and 4.6 (a). They show hardly any features, and most of the few details that can be seen in these "absorption" images are actually a result of edge-enhancing inline phase contrast, especially in Figures 4.2 (a), 4.5 (a), and 4.6 (a), which represent cases in which the propagation distance was relatively long. The nearly-complete absence of absorption contrast is reflected by the poor CNR values of the absorption images (Tables 4.2 and 4.3) and by the fact that their histograms (Figure 4.8, 4.9) have only a single broad peak. Visual inspection shows that the absorption images are dominated by noise and ring artifacts and are unusable for practical purposes, reflecting the fact that absorption contrast is insufficient for the dis-

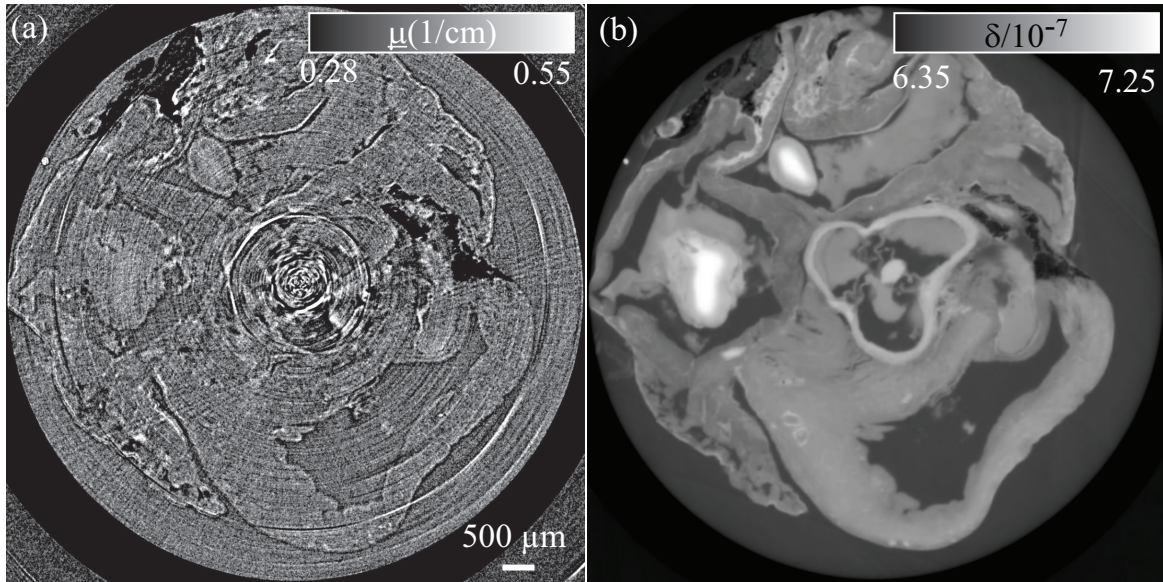


Figure 4.5: Tomographic slices of a rat heart measured with a grating based interferometer at the beamline ID19 (European Synchrotron Radiation Facility, France). The contrast is based on pseudo absorption (a) and phase (b).

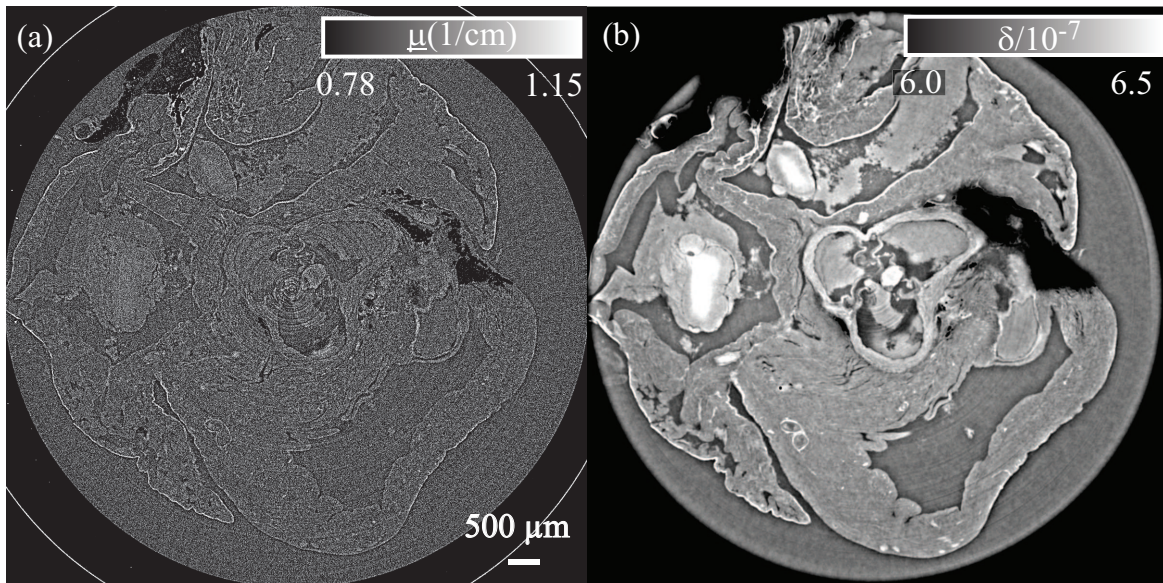


Figure 4.6: Tomographic slices of a rat-heart measured with holotomography at the beamline ID19 (European Synchrotron Radiation Facility, France). The images were obtained with no-phase retrieval (a) at a detector-to-sample distance d_p of 200 mm and holotomography reconstruction (b).

crimination of different types of soft tissue.

Unlike the absorption data, most of the phase tomograms are of high quality in terms of their contrast-to-noise properties. This observation is valid for images obtained from all three phase retrieval methods investigated, i.e., GIFM, holotomography and Paganin's method. However, substantial differences exist between the images obtained with the different methods, and/or from different propagation distances. These will be discussed in the following.

The overall best results in terms of the contrast-to-noise ratio are obtained by interferometry. For most of the materials in the specimens, the CNR values shown in Tables 4.2 and 4.3, which describe the contrast to the immersion liquid PFA, are best for the GIFM data. This is particularly true for tissue and blood. The trend is different for lipid, where the CNR values are similar for PBI and GIFM, and for the container material, where PBI yields much higher CNR values.

The lipid and the container material (assumed to be polypropylene) are structures with relatively strong phase contrast. Closer inspection of the data reveals that the higher CNR for these materials obtained with the PBI techniques compared to GIFM is mainly due to the fact that the contrast at which these structures are rendered is larger in the phase-retrieved PBI images than in GIFM; i.e., the numerator in Equation (4.6) takes a higher value. For example, the section profiles shown in Figure 4.10 show that the reconstructed refractive index of the lipid structures in the tumor differs from the surrounding tissue by no more than 3×10^{-8} in the GIFM tomogram, whereas the difference exceeds 10^{-7} in the PBI images (both Paganin and holotomography). The reconstructed values of δ for the container material are even extremely different between GIFM and the PBI methods: GIFM yields values around 6×10^{-8} (close to the literature value of polypropylene for the working energies), while holotomography and Paganin's approach yield grossly underestimated values around 3×10^{-8} .

These discrepancies in the reconstructed values of δ between the methods can have various origins. Thus, in the PBI techniques, the assumed condition of a fixed, known ratio of δ/β may be violated to an extent that can explain the differences. This is clearly the case for the container material, for which δ/β ranges between 5000 and 6500 for the working energies - more than 3 times higher than the values for water, which were assumed to be uniformly valid in the slice. GIFM is not dependent on such *a priori* assumptions on the X-ray optical properties and yields more quantitatively correct values for these high-contrast materials. However, GIFM may yield systematically reduced contrast in cases where phase wrapping occurs [90]. Even details in the reconstruction algorithms can have a non-negligible influence on the reconstructed values. For example, the histograms in Figure 4.15 demonstrate that the reconstructed values in holotomography depend on whether the detector deconvolution filter is used or not.

When comparing the different PBI images, it should be expected that the images obtained by single-distance phase retrieval should improve in CNR as the propagation distance d_p is increased, because of the generally increasing values of the contrast transfer function (Figure 4.14). Visual inspection of Figures 4.4 and 4.7 seems to confirm this expectation, but the CNR values extracted from these images (Tables 4.2 and 4.3) only partly agree with this finding. In particular, the CNR values obtained for lipid in the tumor sample and for blood and container material in the heart samples do not follow the expected trend. An important reason for this deviation from the expected behavior is the fact that systematic artifacts within the regions assumed to be homogeneous can increase the σ values in the denominator of Equation (4.6) and thus reduce the CNR value obtained. In particular, cupping artifacts due to imperfect

phase reconstruction influence the results in this way. These artifacts tend to become stronger with increasing distance d_p . This explanation is in accordance with the fact that those regions in which the anomalous behavior of the CNR with distance occurs are relatively small in area and strong in contrast, and are thus more likely to be affected by cupping.

The holotomography images systematically show a lesser CNR than the Paganin images. A partial explanation can be related to the higher spatial resolution of the holotomography data (Tables 4.2 and 4.3, Figure 4.12, 4.13), but this is not a valid explanation for the data obtained by holotomography without the use of the detector deconvolution filter [Figure 4.13 (b)].

Not surprisingly, the use of the detector deconvolution filter in holotomography drastically improves the spatial resolution (Table 4.3 and Figures 4.13 (b), 4.13 (c), 4.15). In terms of the statistical properties of the images, one might expect the CNR to decrease as a result of the use of this filter (which acts like a sharpening filter and can thus be expected to amplify noise). However, this is not uniformly the case, as a comparison of the CNR values obtained with and without the filter shows (Table 4.3). The fact that regions as the lipid or the container wall exhibit a better CNR with the filter activated than without it is most probably due to the fact that the sharpened projection images reduce cupping artifacts in the tomograms. The same filter can, in principle, be combined with the other phase retrieval methods, although this was not implemented in the software used for this study.

The spatial resolution, as assessed qualitatively through inspection of feature edges in the images and estimated quantitatively by the RSP method (section 4.2.4 above and last column in Tables 4.2 and 4.3), is clearly better in the PBI images than in the GIFM images. This finding concerns both the absorption images and the phase tomograms. The main reason for this systematic difference between PBI and GIFM is that, while the resolution is limited by X-ray diffraction in both cases, the mechanism is different. In GIFM, the spatial resolution is limited by the shear between the two interfering first orders of diffraction of the grating G1. This shear is

$$s = 2 \frac{\lambda d_m}{g_1} \quad (4.7)$$

Applied to the experimental parameters (Table 4.1), Equation (4.7) yields shear values of $s = 9.9 \mu\text{m}$ for the tumor measurements and $s = 26.2 \mu\text{m}$ for the heart measurement. Since these values are substantially larger than twice the pixel size, $2 \Delta_{pix}$, the detector resolution can be assumed to be only marginally limiting the overall spatial resolution of the GIFM measurements reported here. In the propagation-based images, the spatial resolution is limited by the width w of the first Fresnel zone,

$$w = \sqrt{\lambda d_p} \quad (4.8)$$

The values of w for the PBI measurements on the tumor are $w = 1.0, 2.1, 2.9, 5.0 \mu\text{m}$ (for $d_p = 13, 60, 120, 360 \text{ mm}$). For the rat heart, they are $w = 3.6, 5.1, 6.8, 8.5 \mu\text{m}$ (for $d_p = 200, 400, 700, 1100 \text{ mm}$). The observation of poorer spatial resolution in GIFM compared to PBI (Tables 4.2 and 4.3) is thus in qualitative accordance with the theoretical expectations. The absolute values for spatial resolution obtained via the RSP method, however, differ substantially from the values of s and w obtained from Equations (4.7) and (4.8), but it should be considered that they were obtained with an entirely different method and using different definitions. In addition, the detector resolution is a major limiting factor for the PBI images.

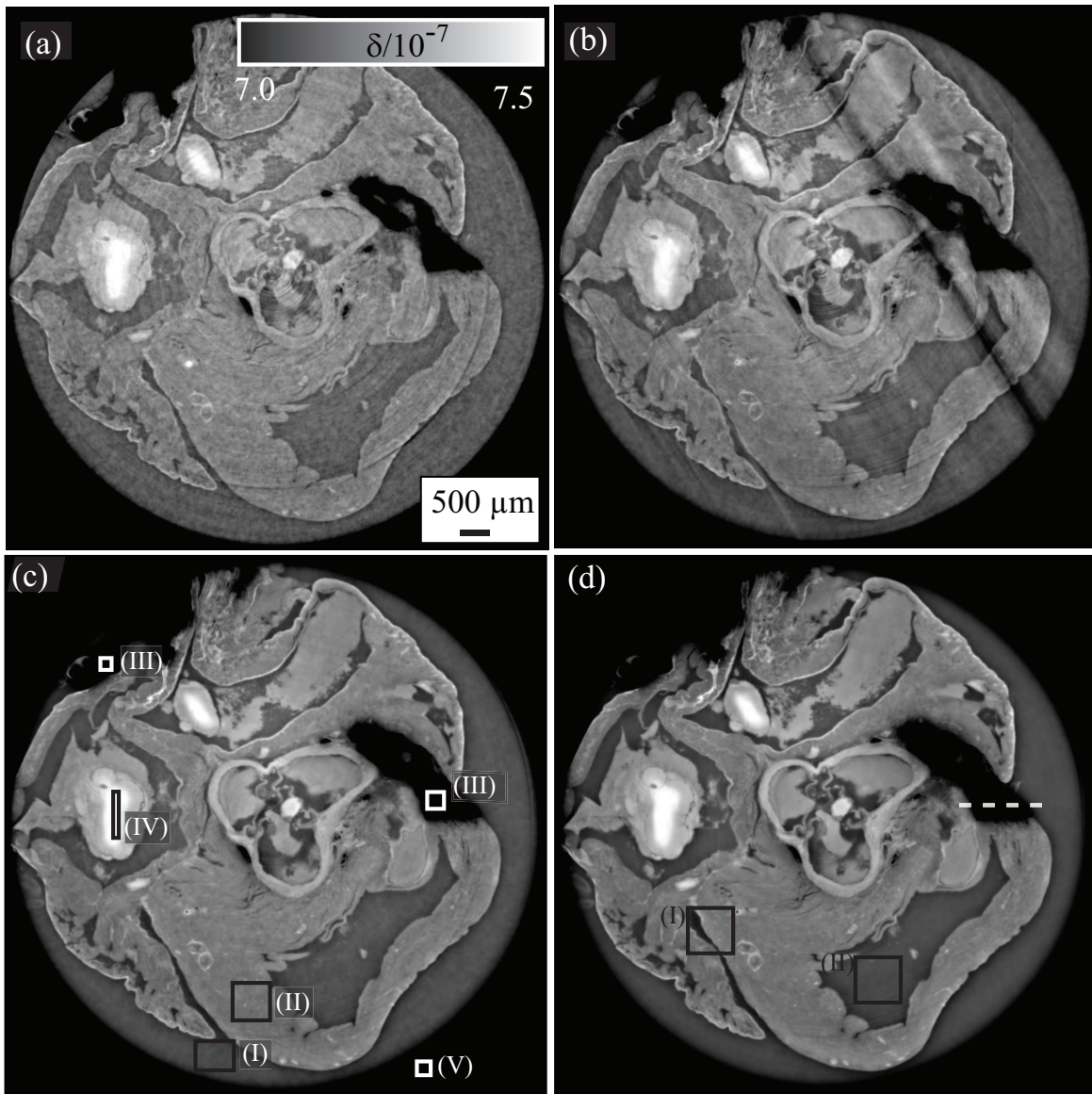


Figure 4.7: Tomographic slices of a rat heart measured with holotomography at the beamline ID19 (European Synchrotron Radiation Facility, France). The images were obtained using Paganin-processing (a)-(d) for distances $d_p = (200, 400, 700, 1100 \text{ mm})$ respectively. To determine the CNR the marked areas in (c) of the features (II-tissue, III-lipid, IV-blood, V-container) against the background (I) were used. The dashed line demonstrates the region along which the profiles (4.11) were taken. The rectangles in (d) show the regions (I-full of features, II-background) which had been used to determine the RSP.

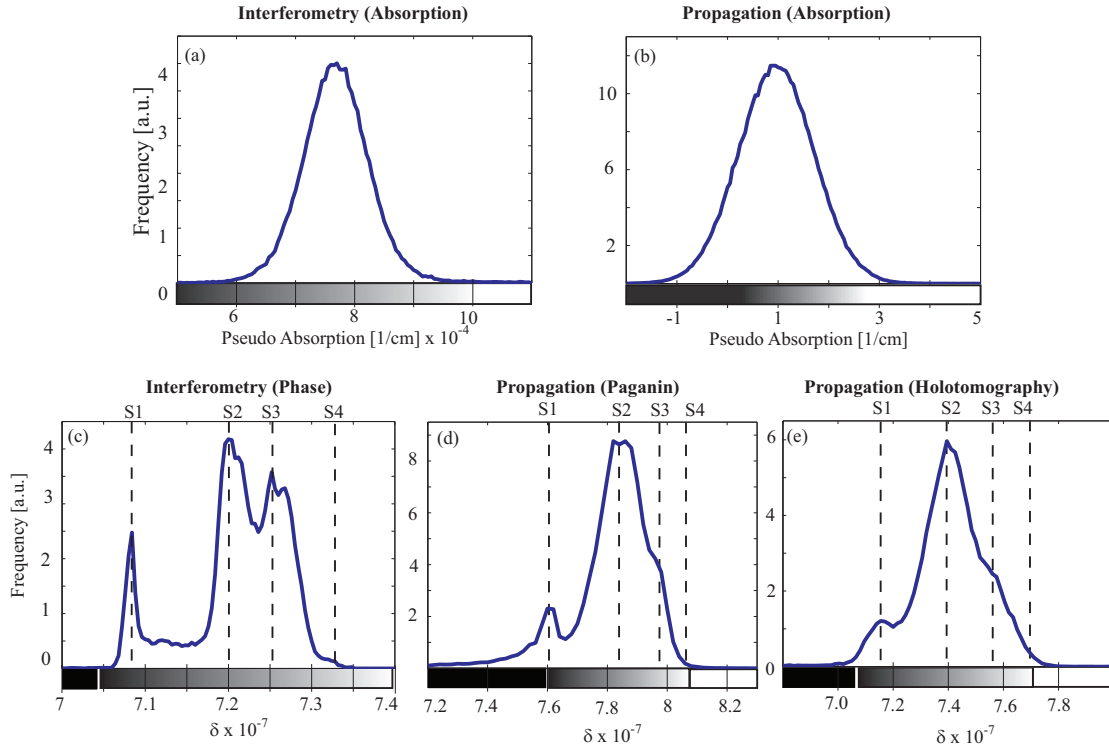


Figure 4.8: The figure illustrates the histograms of tomographic slices of a tumor sample presented in this study. The gray values are based on the pseudo absorption coefficient (a+b) and the real decrement of the refractive index δ . δ -values are obtained by interferometry (c), Paganin processing at highest distances (b) and Holotomography (e). In the gray scale bar the gray value range which can be observed in the images of the respective slice are illustrated. In the phase contrast histograms at least two peaks PFA (left) and tissue (right) can be distinguished. Prominent peaks in the phase contrast histograms are labeled with: S1 - PFA, S2 - Dark Tissue, S3 - Bright Tissue Tumor, S4 - Blood.

The holotomography images (Figures 4.3 and 4.6) clearly have the best spatial resolution among the tomograms obtained in this study, for each of the specimens. This is confirmed by the quantitative values from the RSP analysis (Tables 4.2 and 4.3) and by a look at zoomed details (Figure 4.12, 4.13). This result is more than expected because (a) holotomography combines the good contrast of long propagation distances with the high resolution information that can be obtained at short distances, and (b) among the different computer programs used in this study for retrieving the phase images, the holotomography routine was the only one with a detector deconvolution routine.

The fact that the holotomography reconstruction of the heart data set without the deconvolution yields a spatial resolution even inferior to the reconstructions obtained without such a filter using Paganin's method (4.12, 4.13, Tables 4.2 and 4.3) indicates that the deconvolution filter is decisive for spatial resolution.

One of the striking visual differences between the GIFM tomograms on the one hand and the PBI images on the other - especially in the case of the heart sample - is that the PBI data exhibit remaining phase-contrast fringes even after phase retrieval (Figures 4.6 and 4.7), while the GIFM data do not exhibit any such artifacts (Figure 4.5).

These residual fringes in the PBI images can have a substantial influence on any quantitative analysis of phase tomography data. In the present case, they may have affected the results of resolution estimations by the RSP method, in which they tend to give deceptively good values for spatial resolution. On the other hand, if such fringes are present in regions used for contrast analysis they will degrade the CNR value and broaden the peaks in the histograms. (For the CNR analysis the selected regions were used to exclude these effects, but the histograms shown in Figure 4.8 and 4.9 include their effects.)

More importantly, residual fringes will generally impair the correct interpretation of the reconstructed volume images, whether they are inspected by a human beholder or whether machine-aided segmentation procedures are used. In both cases, the artifacts pose the risk of false-positive recognition of features such as interfacial layers.

The GIFM phase tomography data seem less sensitive to ring artifacts than both absorption data and PBI phase tomograms. In the Paganin-reconstructed images, the influence of ring artifacts decreases with increasing propagation distance. This can be attributed to the fact that, while the phase contrast generally increases with distance, the prevalence of artifacts, which arise predominantly from imperfect correction of sharply-localized variations in the beam profile or non-uniformity of the detector response (e.g., impurities on the scintillator), is essentially independent of distance.

4.5 Conclusion

The comparison of synchrotron-radiation X-ray phase tomography data obtained with different acquisition and phase-retrieval methods, as presented in this study, quantitatively confirms the complementarity of the three methods investigated, i.e., X-ray grating interferometry (GIFM) and two phase recovery methods in propagation-based imaging (PBI): multiple-distance holotomography in a combined TIE/CTF approach, and single-distance phase retrieval using Paganin's method. The GIFM phase tomographic data have the highest density resolution and show the best overall accuracy of the retrieved values of refractive index (where those values were known). They do not show substantial problems with low-frequency

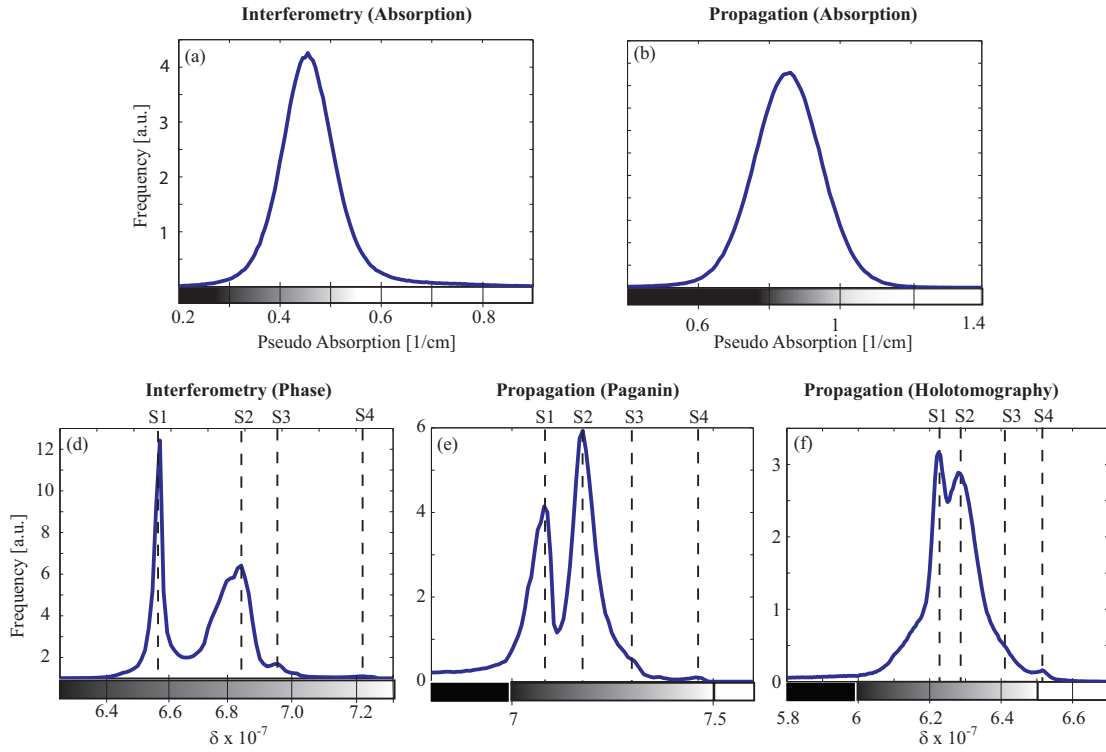


Figure 4.9: The figure illustrates the histograms of tomographic slices of a rat-heart (a-e) presented in this study. The gray values are based on the pseudo absorption coefficient (a+b) and the real decrement of the refractive index δ . δ -values are obtained by interferometry (c), Paganin processing at highest distances (b) and Holotomography (c). In the gray scale bar the gray value range which can be observed in the images of the respective slice are illustrated. In the phase contrast histograms at least two peaks PFA (left) and tissue (right) can be distinguished. Prominent peaks in the phase contrast histograms are labeled with: S1 - PFA, S2 - Tissue, S3 - Vessel Wall (Heart), S4 - Blood.

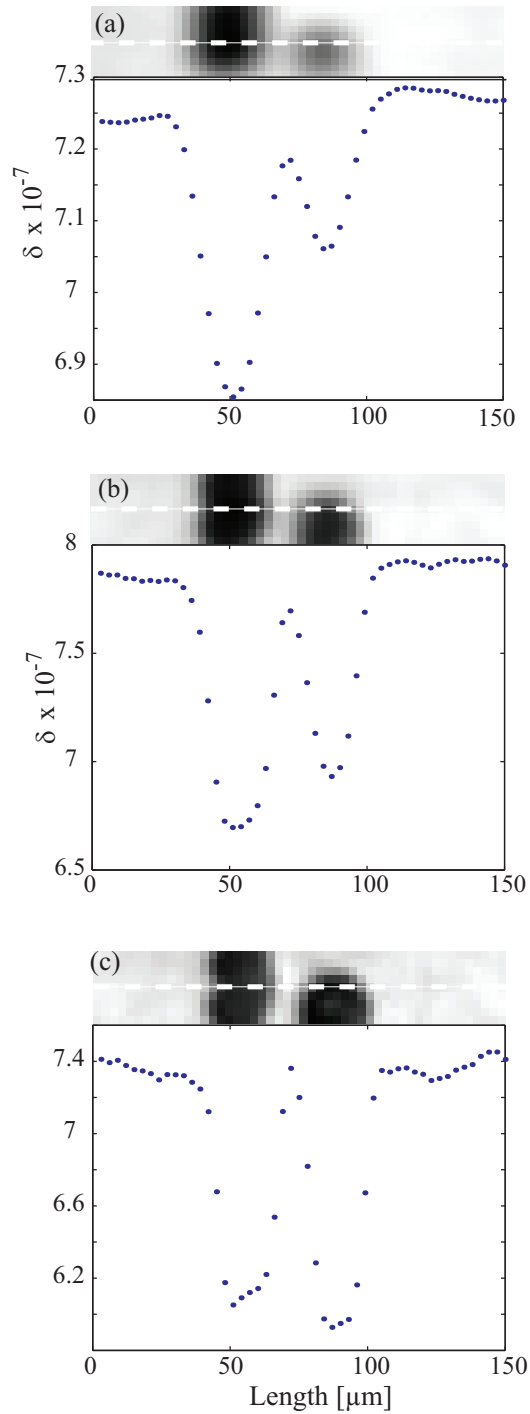


Figure 4.10: The plots show profiles of sections in the tumor images measured with phase contrast based μ CT using X-ray grating interferometry (a) and propagation based μ CT. For the latter one can differentiate between Paganin (b) and Holotomography (c). The profile is selected along the dashed line in the cropped region illustrated above every plot. The position of the dashed line is highlighted in the Paganin image in Figure 4.4 (d).

artifacts such as cupping and have no remaining phase-contrast fringes. This makes GIFM phase tomograms easy to interpret and to segment. On the other hand, the spatial resolution of GIFM is limited by the shear of the two beams created by diffraction in the first grating. Our study confirms that GIFM performs best among the phase-contrast generation methods and phase retrieval algorithms when spatial resolution need not be better than approximately 10 μm . For higher spatial resolution, PBI methods are better suited, mostly because they are limited only by the detector resolution and by Fresnel diffraction from the specimen. The holotomography approach used here performed by far best concerning this figure of merit. An important factor in this good performance was the deconvolution with the estimated detector resolution carried out by the holotomography reconstruction software. Such a deconvolution filter would be a valuable option also in phase retrieval software for the other techniques, where it is yet to be implemented.

For GIFM, the resolution function by which the images are deconvolved should include the effects of grating diffraction. Paganin's method of single-distance phase retrieval has the advantage over GIFM and holotomography that it requires no more instrumental effort than a standard absorption tomography scan, both in terms of the experimental procedure (in particular the net exposure time and the total time required for data acquisition) and the amount of data and number of raw images generated. This can be an important advantage when imaging specimens subject to degradation by exposure to radiation (e.g., development of bubbles in aqueous environments), temperature change etc. A somewhat unexpected result is that, in holotomography, the combined CTF/TIE approach chosen for the reconstructions here proved to be as much influenced by strong deviations of δ/β from the assumed value, in certain regions of the specimen, as the single-distance approach. However, holotomography could generally have performed better in this study if the data from the shortest distance had been usable.

From a users point of view, it can be noted that there is a tradeoff between complexity of the setup, complexity of the data processing, and quality of the data. Among the methods used here, GIFM is the one that requires the most complex mechanical setup. However, the data analysis requires no other parameters than the experimental geometry, and in particular no knowledge of the sample composition. The processing is thus, in principle, fully automatic. An important restriction is, however, the need to avoid phase jumps. The specimen therefore either needs to be immersed in a phase-matching liquid (here: water), or the outer edges of the specimen (or its container) need to be replaced in the projection radiographs by modeled data, an approach chosen for one of the samples measured in this study. Holotomography, on the other hand, is conceptually simple in terms of data acquisition. The difficulty lies in the processing, which requires substantial manual interaction and a good degree of expertise. It also requires image registration of the data taken at different distances. While this step is largely automated, it may fail or yield unsatisfactory results. Single-distance phase retrieval with Paganin's method is very simple and fast in terms of data acquisition and relatively easy in processing (although it requires a reasonable correct guess of δ/β), but good results are only obtained for "well-behaved" objects, in which the actual ratio δ/β does not deviate too much from the assumed value.

Table 4.2: Contrast-to-noise ratios (CNR) and spatial resolution (SR) obtained with the different modalities, for the tumor sample. The CNR values were determined from the ROIs indicated in Figure 4.4 (c) using the definition in Equation 4.6. The CNR is determined between three features (dark tissue, bright tissue and lipid cells) and areas representing paraformaldehyde (PFA). The SR was determined with the RSP method using the regions presented in Figures 4.4 (d).

Tumor	CNR tissue, dark	CNR tissue, bright	CNR lipid	SR (μm)
Interferometer (Absorption)	1.5	12.2	5.2	19.2
Interferometer (Phase)	59.4	54.4	167.8	24.5
Paganin ($d_p = 13$ mm)	6.1	11.9	139.8	12.0
Paganin ($d_p = 60$ mm)	17.3	17.7	171.9	9.8
Paganin ($d_p = 120$ mm)	20.4	17.3	147.6	10.2
Paganin ($d_p = 360$ mm)	23.8	19.9	58.9	11.4
Holotomography, with detector deconvolution	11.1	11.7	97.3	8.0
Absorption ($d_p = 13$ mm)	0.1	0.4	8.8	6.1

Table 4.3: Contrast-to-noise ratios (CNR) and spatial resolution (SR) obtained with the different modalities, for the heart sample. The CNR values were determined from the ROIs indicated in Figure 4.7 (c) using the definition in Equation 4.6. The CNR is determined between four materials (tissue, lipid, blood and container wall) and areas representing paraformaldehyde (PFA). The SR was determined with the RSP method using the regions presented in Figures 4.7 (d).

Heart	CNR tissue	CNR lipid	CNR blood	CNR container	SR (μm)
Interferometer (Absorption)	0.6	13.3	9.5	56.5	58.9
Interferometer (Phase)	54.7	103.8	262.8	250.9	81.7
Paganin ($d_p = 200$ mm)	13.8	29.2	89.4	594.9	49.1
Paganin ($d_p = 400$ mm)	13.6	35.6	103.7	879.6	40.3
Paganin ($d_p = 700$ mm)	24.1	82.6	256.1	539.9	38.6
Paganin ($d_p = 1100$ mm)	24.9	87.4	134.5	267.6	38.6
Holotomography, without detector deconvolution	15.9	84.1	114.6	319.4	70.0
Holotomography, with detector deconvolution	9.3	97.9	112.8	428.0	40.3
Absorption ($d_p = 13$ mm)	0.7	20.1	3.5	32.3	36.5

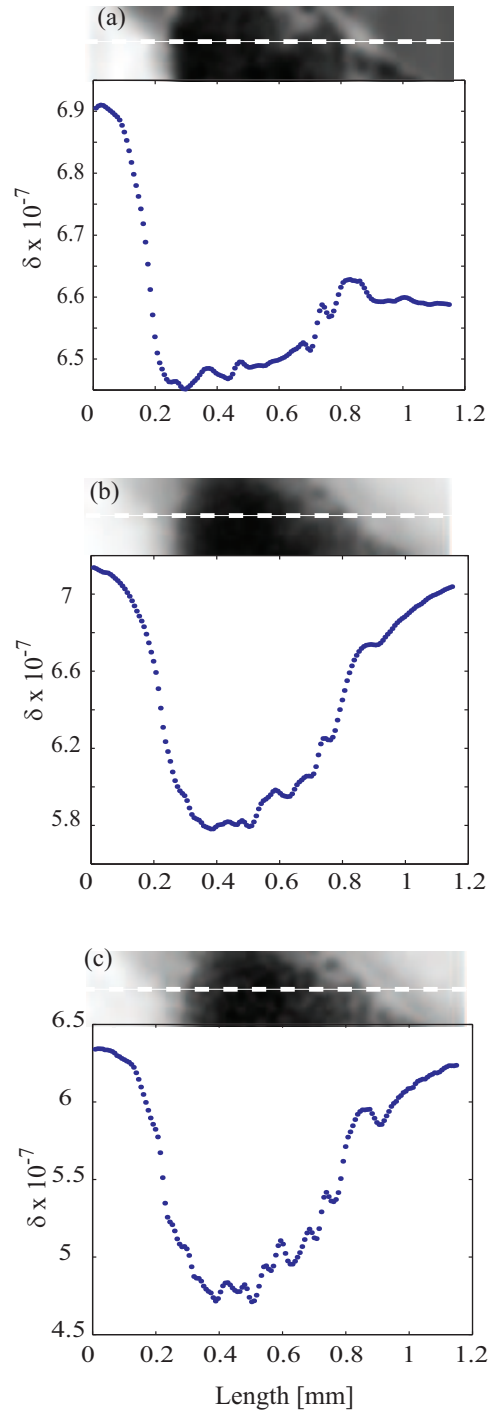


Figure 4.11: The plots show profiles of sections in the rat-heart images measured with phase contrast based μ CT using X-ray grating interferometry (a+d) and propagation based μ CT. For the latter one can differentiate between Paganin (b) and Holotomography (c). The profile is selected along the dashed line in the cropped region illustrated above every plot. The position of the dashed line is highlighted in the Paganin image in Figure 4.7 (d).

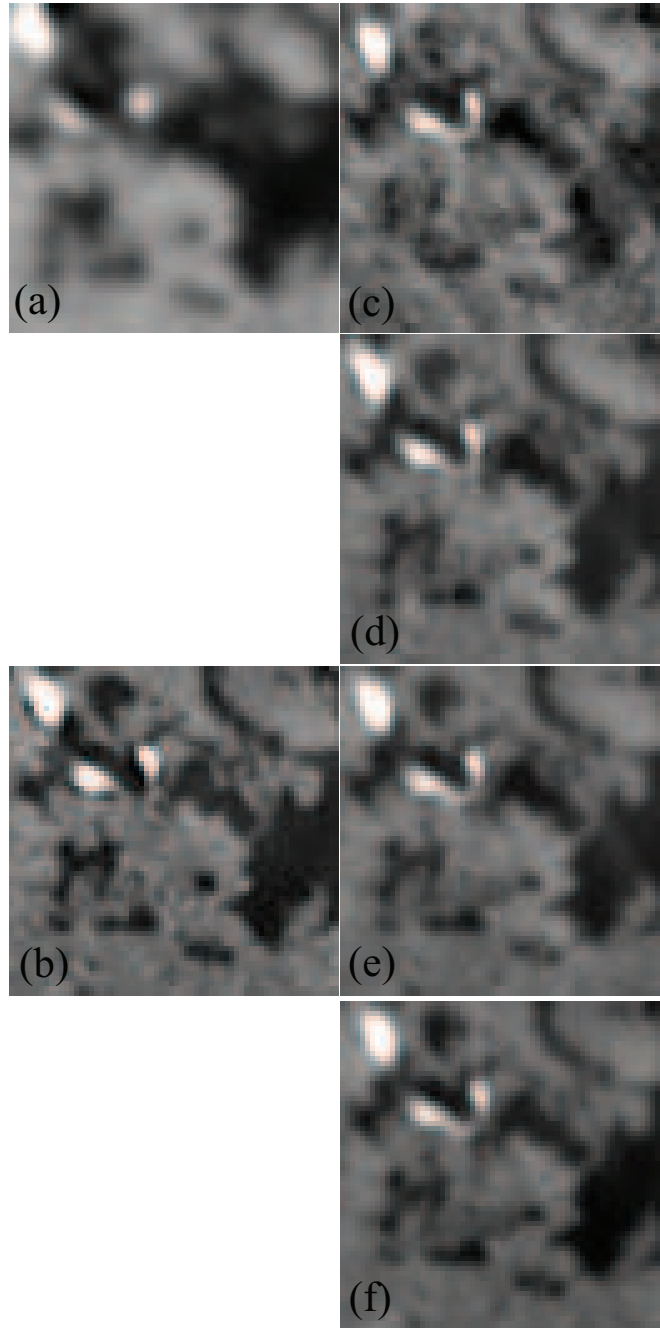


Figure 4.12: *The images show the cropped regions of the phase contrast based tomographic slices of the tumor to obtain the spatial resolution using the RSP. The images are ordered as follows: GIFM (a), Holotomography with detector convolution (b) and (c-f) Paganin in the order of smaller to larger sample-to-detector distances.*

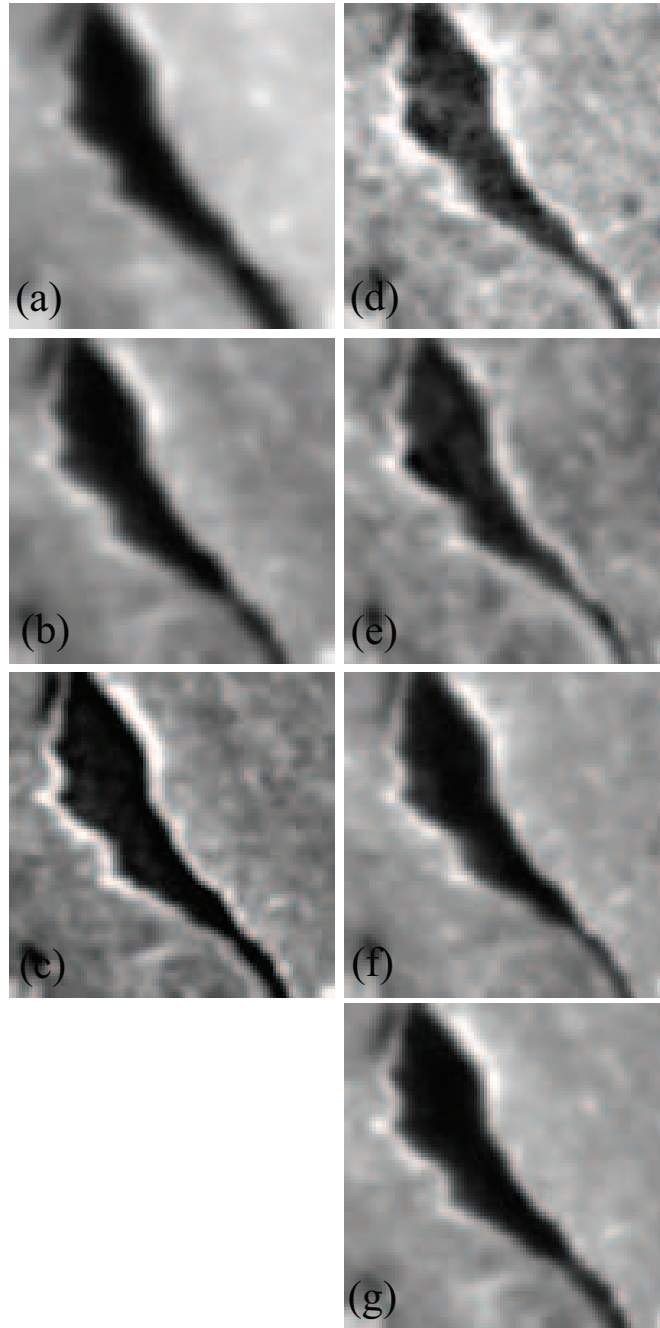


Figure 4.13: *The images show the cropped regions of the phase contrast based tomographic slices of the rat-heart to obtain the spatial resolution using the RSP. The images are ordered as follows: (GIFM (a), Holotomography with detector convolution (b), without detector convolution (c) and (d-g) Paganin in the order of smaller to larger sample-to-detector distances.*

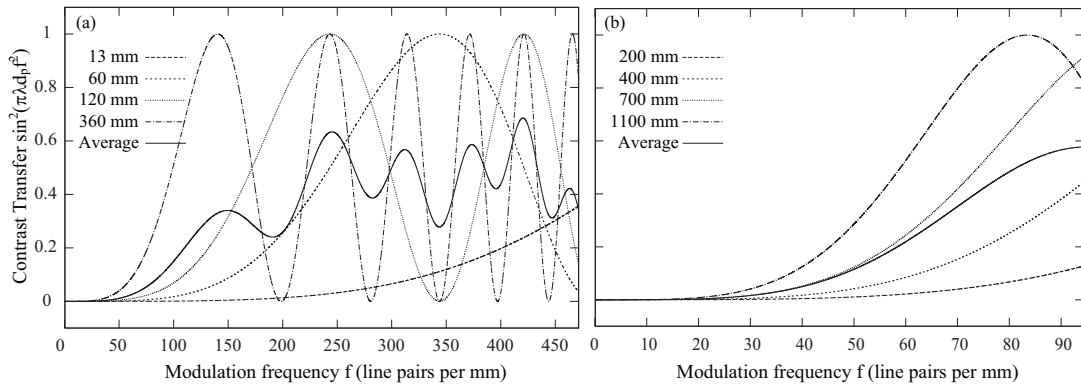


Figure 4.14: *The plots show the simulated contrast-transfer functions (CTF) for the propagation based tomography measurements of the tumor sample (a) and the rat-heart (b). The thick curves represent the combination of all CTF's obtained for different sample-to-detector distances d_p .*

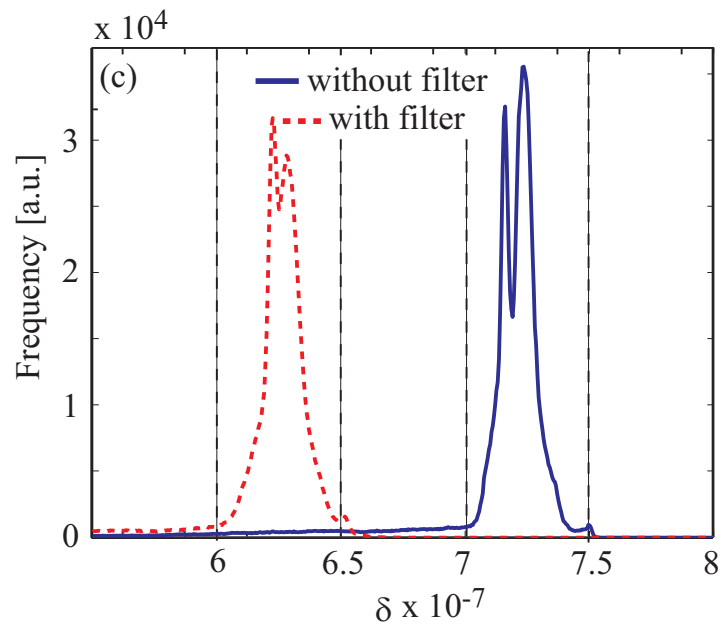
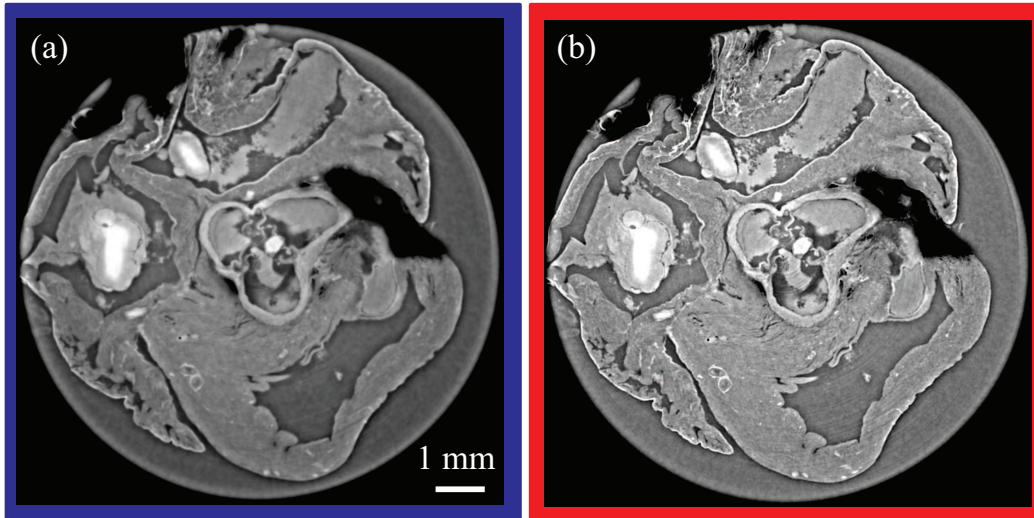


Figure 4.15: Tomographic slices of a rat-heart measured with holotomography at the beamline ID19 (European Synchrotron Radiation Facility, France). The propagation based raw data was processed with holotomography without (a) and with a detector filter (b).

Chapter 5

Morphological assessment of the vessel trees in cancerous and healthy tissues using synchrotron radiation-based micro computed tomography

5.1 Introduction

Tumor growth directly relates to angiogenesis in cancerous tissue [3,95]. As a result, the three-dimensional (3D) analysis of the vessel tree, including smallest capillaries, belongs to the key issue in cancer research. While in vivo methods such as magnetic resonance imaging (MRI) only indirectly provide the angiogenic network because of limited spatial resolution, highly sophisticated ex vivo techniques such as synchrotron radiation-based micro computed tomography (SR μ CT) allow the direct visualization of the capillaries [11, 17]. For these studies, however, the absorption contrast between the vessels and the surrounding soft tissues has to be improved to allow vessel segmentation [21], which requires staining protocols [11, 17], tissue embedding [10] or corrosion casting [25]. These procedures only work for intact vessel walls. In advanced stages of tumor formation, the vessels become leaky and the contrast agents, the embedding compound and the low viscosity resin for corrosion casting can penetrate through the damaged parts of the vessel walls. For these cases, phase contrast SR μ CT should be applied, since the achievable contrast is orders of magnitude higher than for the rather conventional absorption contrast mode. Hence the complicated tissue preparation procedures can be omitted at the expense of higher experimental efforts. The spatial resolution of many phase contrast techniques, however, disallows the identification of the smallest capillaries. Therefore, further efforts should be invested to extract the vessel tree with reasonable contrast and true micrometer resolution so that the entire network of vessels within a reasonably large part of the tumor can be segmented. For the phase contrast tomography data the vessels are difficult to be segmented using intensity-based approaches such as choosing an appropriate threshold. Therefore, the segmentation of the vessel tree was proposed by using a tool that detects vessels by means of their characteristic geometry (tubular structure), rather than by

a range of gray values. The feature-based method Frangi filter [96] is a well-established tool for the segmentation of vessels [97]. The limited photon statistics, always present in SR μ CT datasets [98], impedes the segmentation of continuous vessels commonly from arteries via capillaries toward veins. The passage, however, is a well-established matter of fact and, therefore, a vital prerequisite for simulating tumor formation. A direct comparison of these simulations with experimental high-resolution data by means of the vessel tree parameters requires not only the segmentation itself but also includes the skeletonization [95,99] and vectorization of the vessel tree from the SR μ CT data. Once the vessel tree has been successfully extracted, one can analyze the numerous parameters that characterize the vascular structure of healthy and cancerous tissues [3, 50, 99–102]. So far, the tortuosity of the vessel tree has been reported to be a key indicator to identify diseased tissue [99]. As soon as, the experimental parameters of vessel trees become available, the computer codes simulating tumor growth to get detailed insight in the neo-vascularization [7] can be validated or refused. Such validated simulations are promising paths to significantly ameliorate anti-angiogenesis treatments against cancer [101]. So far, it is still unclear how well the simulations of tumor growth describe the complex processes within the human body. In order to search for the characteristic parameters for cancerous vessels with respect to healthy ones, it has been examined the vascular structure of tissues on the basis of SR μ CT data. Corrosion casts of healthy and cancerous tissues imply ideal contrast and well-defined spatial resolution, but also the presence of preparation artifacts, which, for example, inhibit the precise measurement of vessel diameters. Therefore, additionally tumor specimens were measured using phase contrast SR μ CT.

These high-resolution absorption and phase contrast tomograms are processed to produce a vector-based representation of the vessel trees. It is shown, that the in-depth comparison of vessel trees in terms from healthy and diseased tissues exploring the vessel diameters, bifurcation densities (branching), angles between branching vessels, vessel/mean void distances, vessel lengths, tortuosity, and vessel density with the aim to find the leading indicators for the formation of cancerous tissue.

5.2 Material and Methods

The suspension with 10^6 C51 tumor cells from murine colon carcinoma was subcutaneously injected on the left flank of nude mouse (balb/c - Charles River Laboratories, France) in strict adherence to the Swiss law for animal protection. The first mouse was euthanized after 7 days and the second animal after 14 days. The 7-day old tumor about $(3 \text{ mm})^3$ in size was extracted and fixed in 5% para-formaldehyde solution (PFA), before transferred into the polymer container for SR μ CT measurements in phase contrast mode.

A polyurethane-based material according to the procedure described by Krucker et al. [25] served for exchanging the blood of the other freshly sacrificed animal to fabricate a corrosion cast of the entire circulatory system. This cast was fragmented to harvest the tumor vessel tree with a size of about $(10 \text{ mm})^3$ from the left flank and the casted vessels from healthy tissue $(45 \text{ mm})^3$ in size from the right flank. The casts were visualized using SR μ CT in absorption contrast mode.

Local tomography data of the cast from the cancerous tissue were recorded at the TOMCAT beamline (Swiss Light Source (SLS) at Paul Scherrer Institut, Villigen, Switzerland) [60] using a photon energy of 15 keV and a pixel size of $2 \times 0.74 \mu\text{m}$. The exposure time for each of the

1500 radiographs for equidistant rotation angles between 0° and 180° was set to 0.7 s. The 4 Mpixels detector covered only around 15% of the cast's projection.

The tomography data of the cast from the healthy tissue were scanned at the beamline BW 2 (HASYLAB at DESY, Hamburg, Germany). The Helmholtz Center Geesthacht, Germany [98] operated the tomography setup. Using a photon energy of 10 keV, a pixel size of $1.98 \mu\text{m}$ and an exposure time of 5.85 s, 1440 radiographs equidistantly acquired along 360° with an asymmetric rotation axis (see [19]) were combined to 720 radiographs used for data reconstruction. The spatial resolution determined from the 10% value of the modulation transfer function corresponded to $4.7 \mu\text{m}$ [74]. The X rays were converted to visible light by means of CdWO_4 scintillator with a thickness of $200 \mu\text{m}$.

The SR μ CT measurement taking advantage from propagation-based holotomography [34, 35] was conducted at the beamline ID 19 (ESRF, Grenoble, France). The ESRF-detector consisted of a $19\text{-}\mu\text{m}$ -thick gadolinium gallium garnet scintillator, a $10\times$ microscope optics and the FReLoN camera (model 230-42, 2048×2048 pixels of $15 \mu\text{m}$ size) resulting in an effective pixel size of $1.5 \mu\text{m}$. Using a photon energy of 17.6 keV filtered from the undulator spectrum by means of a Ru/B4C-multilayer with 4 nm-period and an exposure time of 0.3 s per radiograph, 800 radiographs equidistant between 0° and 180° were obtained for each of the three specimen-detector distances 60 mm, 120 mm, and 360 mm.

For holotomography, the phase retrieval was required for the reconstruction. The phase retrieval algorithm, implemented in GNU Octave version 2.1.73, was a mixed approach between the contrast transfer function (CTF) and the transport of intensity equation (TIE) [37, 87, 91]. The reconstruction was performed by means of the filtered back-projection technique, implemented in the parallel-beam reconstruction software PyHST (European Synchrotron Radiation Facility, Grenoble, France) [62]. The SR μ CT data obtained in the absorption contrast mode were reconstructed with the software available at the beamlines, both based on the conventional filtered back-projection algorithm [1].

The tomography data were segmented using an implementation in Matlab 7.10.9 R2010a (Simulink, The MathWorks, Inc., USA) of Kroon (2009) and skeletonized using the software implemented in MS Visual C++ 2010 Express V.4.0.30319RTMRel by Cornea et al. [49]. For the vectorization a coded also implemented in Matlab was applied. VG Studio Max 2.0 (Volume Graphics, Heidelberg, Germany) served for the 3D representations.

5.3 Image Analysis

The image analysis of the vascularization was conducted for the healthy and the cancerous corrosion cast as well as for the holotomography specimen of the tumor tissue.

To evaluate the local differences in the vessel parameters, four regions of interests were selected in each tomography dataset. Three regions of interest (ROI_1 , ROI_2 , ROI_3) were chosen in the size of $180\times 180\times 180$ voxels and a larger one (ROI_{large}) in the size of $590\times 590\times 500$ voxels, such that they were filled with vascular structures. The distance of smaller regions to the specimen center decreased from ROI_3 to ROI_1 [62].

Segmentation

In the case of the corrosion cast it was sufficient to set an appropriate intensity-based threshold for the segmentation. The threshold was defined in the absorption histogram by the

intersection point of two Gaussians related to the cast and the surrounding air [103]. The number of voxels representing air was almost equal to the one concerning the cast. Since the intensity values of the vessels strongly overlap with the values of other structures in the phase contrast dataset, the feature-based algorithm 'Frangi-Filter' was used for the vessel segmentation in the holotomograms. The Frangi-Filter is based on the eigenvalues $\lambda=(\lambda_1, \lambda_2, \lambda_3)$ of the three dimensional Hessian matrix [47] and provides the probability of a voxel to belong to a vessel e.g. its vesselness [96,104]. In this context the shape of the vessel is assumed to be tubular [48,105]. The vesselness function of the scale s is described by:

$$V_0(s) = \begin{cases} 0 & \text{if } \lambda_2 > 0 \vee \lambda_3 > 0 \\ \left(1 - \exp\left(-\frac{R_A^2}{2\alpha^2}\right)\right) \left(\exp\left(-\frac{R_B^2}{2\beta^2}\right)\right) \left(1 - \exp\left(-\frac{S^2}{2\gamma^2}\right)\right) & \text{else} \end{cases} \quad (5.1)$$

The ratio $R_A = |\lambda_2|/|\lambda_3|$ distinguishes between plate- and needle-like structures, the ratio $R_B = |\lambda_1|/\sqrt{|\lambda_2\lambda_3|}$ accounts for spherical structures $S = |\lambda|$ and for the "second order structureness". For an ideal tubular structure the eigenvalues fulfill the conditions $|\lambda_1| \approx 0$, $|\lambda_1| \ll |\lambda_2|$, $\lambda_2 \approx \lambda_3$ [47,96]. The constants α , β and γ determine the sensitivity of the filter measures R_A , R_B und S . The sign of eigenvalues λ_2 and λ_3 reflects if dark vessels reside in a bright background or vice versa. Finally, the vesselness measure is the maximum value of the vesselness function within the range $s_{min} \leq s \leq s_{max}$. In the present study, the scale range for the tube-like structures was chosen from 1 to 6 voxels (1.5 to 9 μm). The histogram of the resulting vesselness measure revealed an exponential decay. The data were binarized setting a threshold at 1% of the highest frequency detected. The threshold value of 1% results from a trade-off between capturing blood vessels and avoiding detecting structures caused by noise. It was chosen manually by visual judgment. An increase of the threshold leads to the segmentation of noisy structures, while a decrease reduces the volume of the segmented blood vessels.

Vectorization

The centerlines of the vessels were extracted using a skeletonization-code based on voxel erosion [49]. A 3D component labeling algorithm ordered the skeleton data by its number of objects. The neighboring voxels of each object were determined step by step from an arbitrary seed point. Objects with a total size of less than 10 voxels were neglected and replaced voxels in straight line by vectors. Finally, the vessel segments were represented by sorted lists of centerline points. The data components of a vessel included both endings T_1, T_n (0: endpoint, 1: bifurcation point), n positions of the vector points r_i , its mean radius R_m with its standard deviation R_s and the vessel length L . The radii at the centerline points were derived from the distance transformation of the dataset and averaged to the mean radius R_m . The vessel length L was evaluated by the sum of all distances between the vector points.

Vessel diameter, length and bifurcation

The mean diameter of the vessel tree was evaluated based on the average of all vessel radii R_m . The vessel length is the mean of the vessel segment lengths including inter-branch distances. The bifurcation density describes the relationship of the number of bifurcation points to the number of vessel segments and the bifurcation angle the mean angle at the bifurcations.

Tortuosity

The tortuosity of the vessel tree was analyzed in terms of the distance metric (DM) and a variant of the sum of angle metrics (SOAM) [99]. Distance metric (DM) corresponds to the ratio between the length of a line segment and the distance between the two endings [100]. Vessels deviating from a straight line show a distance metric value larger than one. Since this approach cannot distinguish between sinusoidal and C-curved vessels, Bullitt et al. [99] introduced the sum of angle metric. It is based on the ratio between the total curvature of segment and the vessel length, where the total curvature, the integral of the local curvature over the segment, is geometrically interpreted as a sum of the in-plane angle IP and the tortuous angle TP .

$$SOAM = \frac{\sum_{k=2}^{n-2} \left(\sqrt{IP_k^2 + TP_k^2} \right)}{L} \quad (5.2)$$

In case of co-linearity between the two vector points the tortuous angle is defined as zero. The SOAM yields a value of zero for a straight line.

Vessel and mean void distance

The vessel density represents the ratio between the voxels belonging to a vessel and the total number of voxels. The vessel density was determined in the 3D dataset and in the three orthogonal 2D sections. Three dimensional distance transformations of the datasets lead to the measurements of the void density and the mean void distance. The results were obtained by using every second voxel of the discretized vessel to reduce misleading effects due to the voxel discretization of the vessels.

Table 5.1: Vessel parameters for the healthy vessel cast (1.98 μm detector pixel size), the cancerous vessel cast (1.48 μm detector pixel size) and the vessels from a phase contrast measured tumor (1.5 μm detector pixel size). The parameters were determined for the region ROI_{large} ($590 \times 590 \times 500$ voxels).

	Mean Vessel Diameter (μm)	Mean Vesel Length (1/cm)	Tortuosity		Angle $_{Bif}$ (deg)	Vessel Density			Mean Void Distance (μm)	
			DM	SOAM (rad)		3D (%)	2D (%)			
							x	y		z
Healthy Cast	8.8 ± 4.2	20 ± 23	1.3 ± 0.6	0.18 ± 0.19	116 ± 29	9	6	5	10	49.9 ± 0.5
Tumor Cast	5.4 ± 5.0	17 ± 23	1.2 ± 0.6	0.24 ± 0.25	117 ± 28	9	8	7	10	53.4 ± 1.7
Tumor in PFA	9.5 ± 4.2	13 ± 13	1.2 ± 0.6	0.18 ± 0.24	115 ± 33	2	1	1	1	79.3 ± 1.3

5.4 Results

Vessel volume fraction

The vessel density features an anisotropic behavior in most of the selected regions (see Table 5.1 and 5.2). Figure 5.1 also illustrates this observation in terms of the three dimensional distance transformation (tumor cast, ROI_1), where the vessels appear in black. The colored void distance differs in the orthogonal sections in its maximum and its distribution. The largest void region can be found in the green section surrounded by rather dense vessel,

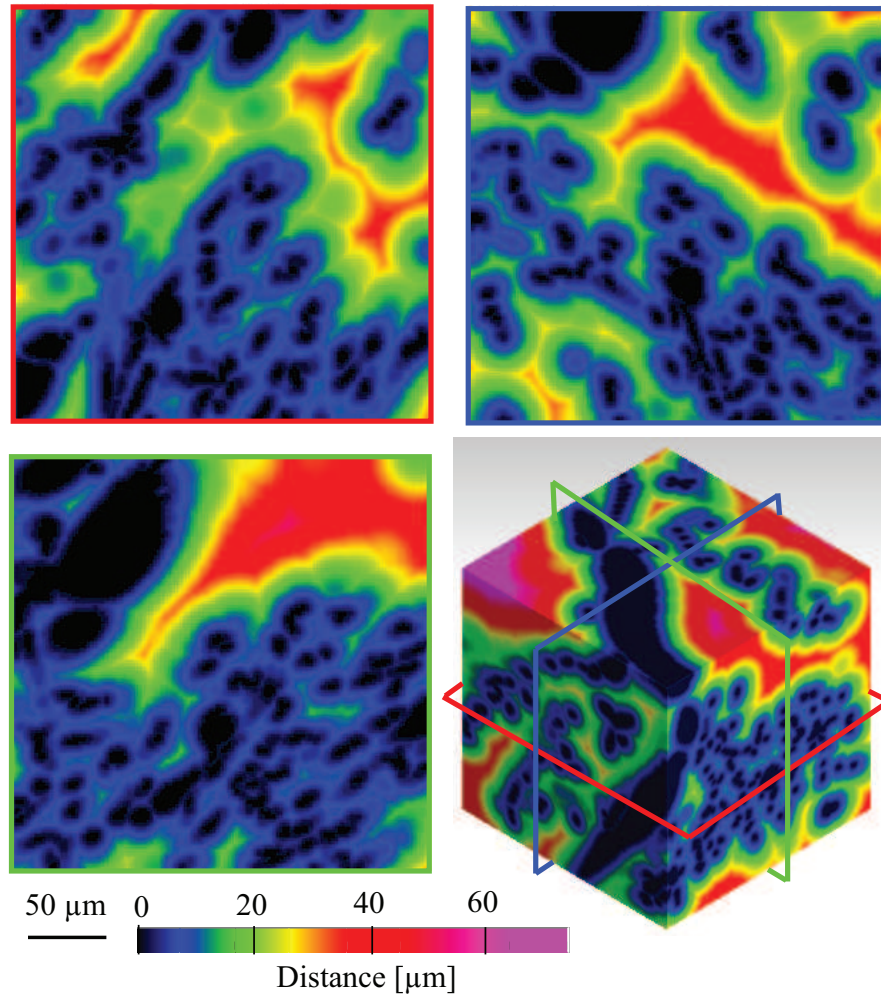


Figure 5.1: *The 3D distance transform of the cancer cast (ROI_1) reveals the void distances between the vessels. The void distance is evaluated on the segmented voxel data set in a robust manner, by determining the distance of a voxel to its closest vessel in 3D. The mean void distance is an indicator for the mean distances between the vessels and correlates inversely to the vessel density. The orthogonal 2D sections represent slices with a thickness of one voxel., i.e. the distance of a voxel to its closest vessel.*

Table 5.2: Vessel parameters for the healthy vessel cast (1.98 μm detector pixel size), the cancerous vessel cast (1.48 μm detector pixel size) and the vessels from a phase contrast measured tumor (1.5 μm detector pixel size). The parameters were determined for the regions ROI₁ to ROI₃ (180 \times 180 \times 180 voxels).

	Mean Vessel Diameter (μm)	Mean Vesel Length (1/cm)	Tortuosity		Angle _{Bif} (deg)	Vessel Density			Mean Void Distance (μm)	
			DM	SOAM (rad)		3D (%)	2D (%)			
							x	y		z
Healthy Cast	10.2 \pm 2.8	15 \pm 16	1.3 \pm 0.6	0.15 \pm 0.2	114 \pm 30	7	5	6	7	68.6 \pm 2.1
	5.5 \pm 1.2	31 \pm 36	1.2 \pm 0.5	0.13 \pm 0.15	116 \pm 27	4	4	4	4	71.7 \pm 1.2
	10.9 \pm 7.5	23 \pm 27	1.2 \pm 0.4	0.19 \pm 0.19	115 \pm 25	19	12	12	20	42.2 \pm 1.9
Tumor Cast	4.9 \pm 1.4	20 \pm 24	1.2 \pm 0.4	0.25 \pm 0.24	119 \pm 29	7	12	6	6	46.2 \pm 2.3
	4.0 \pm 2.5	13 \pm 14	1.4 \pm 1.2	0.22 \pm 0.26	114 \pm 32	3	2	2	3	43.8 \pm 1.4
	5.1 \pm 3.2	14 \pm 18	1.3 \pm 0.7	0.22 \pm 0.25	115 \pm 29	8	8	13	9	86.1 \pm 2.1
Tumor in PFA	6.4 \pm 3.6	12 \pm 10	1.3 \pm 1.0	0.19 \pm 0.24	112 \pm 31	2	4	3	4	60.1 \pm 2.4
	4.6 \pm 1.7	9 \pm 8	1.1 \pm 0.3	0.17 \pm 0.37	107 \pm 33	5	3	3	5	76.8 \pm 0.8
	9.0 \pm 5.6	11 \pm 10	1.3 \pm 0.9	0.18 \pm 0.25	112 \pm 33	3	3	2	2	95.1 \pm 0.2

whereas the vessels are distributed more uniformly in the other two sections. The mean void distance behaves inversely to the vessel density in ROI_{large}, and in most of the smaller ROIs.

Phase contrast

The phase contrast based tomography identified successfully the vessels in the tumor without contrast enhancing specimen preparations (see bright spots in Figure 5.2). Most of the vessels are located in the outer region of the tumor.

Vectorization

Figure 5.3 shows the segmented vessel trees and their vectorization for ROI₁, where the red dots represent the bifurcation points. The bifurcation density was found to be 27% for the healthy cast, 29% for the tumor cast, and 11% for the phase contrast data set. This corresponds to volume density values for the bifurcations of 1.6 mm^{-3} in the healthy tissue, to 3.8 mm^{-3} in the cancerous cast, and to 2.7 mm^{-3} in the phase tomography data. In all selected regions the phase contrast provided the smallest bifurcation density. The bifurcation angles exhibit a narrow distribution between 113 $^\circ$ and 119 $^\circ$ (see Table 5.1).

Tortuosity

Table 5.1 shows the tortuosity, the deviation from the straight line, in terms of the distance metric (DM) and the weighted sum-of-angle-metric (SOAM). The maximum values of the tortuosity based on the SOAM can be found for the cancer cast. Figure 5.4 illustrates the appearance of tortuosity in the healthy and cancerous vascularization. While the tumor features a large variety of tortuous vessels, the tortuosity in healthy tissue appears only at very few capillaries.

Vessel diameter and length

The mean vessel diameter ranges from 5 to 15 μm . For most of the analyzed datasets the healthy vessel cast exhibits the largest values for the diameter. The vessel length varies between 10 and 35 μm where the phase contrast based dataset features the smallest values for all ROIs.

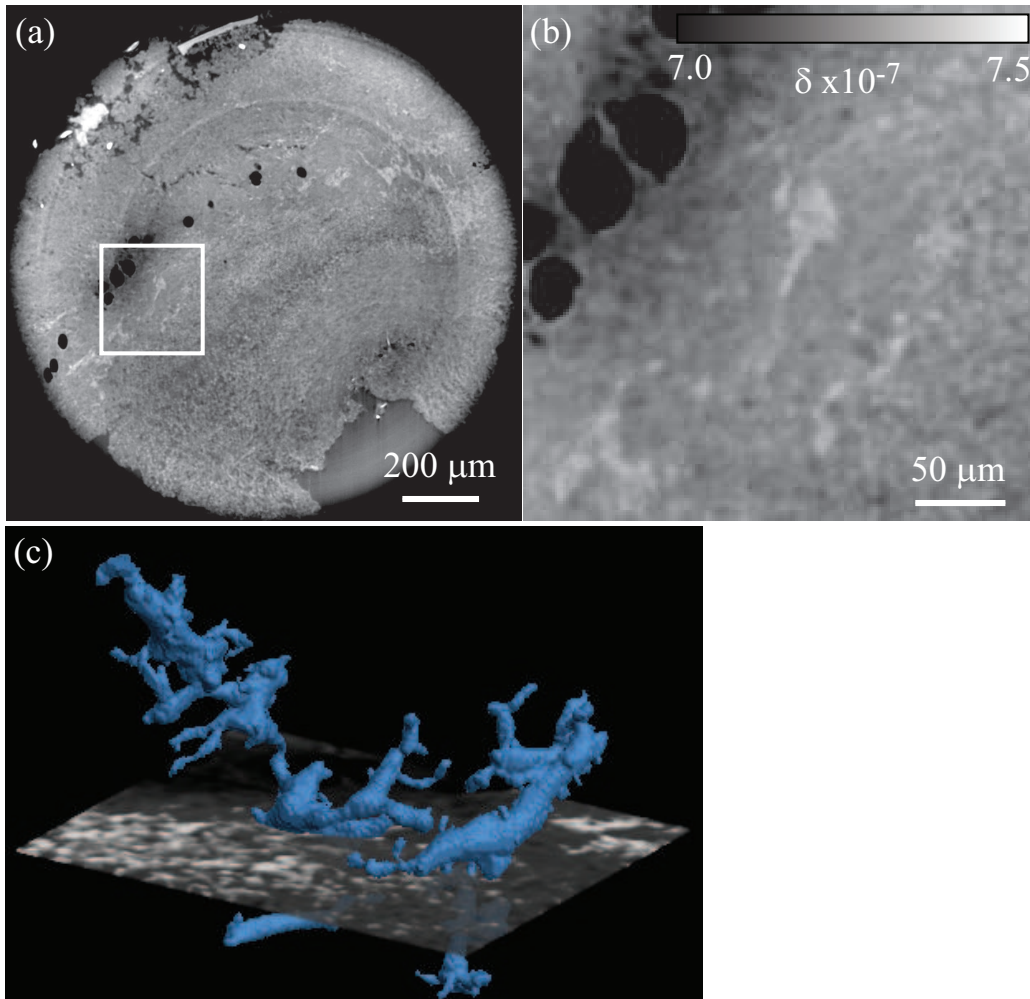


Figure 5.2: (a) The tomography slice of a tumor measured with phase contrast μCT (ID 19, ESRF, France) displays vessels down to the capillary size. (b) The zoom-in shows lipid cells (black) and vessels (white). The gray scale is based on the real decrement δ of the refractive index. (c) Segmentation of these vessels was achieved using the Frangi filter.

5.5 Discussion

The vascularization was analyzed for corrosion cast of the healthy and the cancerous tissues as well as for the tumor sample of the phase contrast measurements. As the selected voxel length is significantly smaller than the smallest capillary diameters, the spatial resolution for the different tomography systems is sufficient to segment the entire vessel tree. For both healthy and cancerous tissue the vessel density is anisotropic, i.e. depending on the direction selected. As a result, a 3D analysis is necessary to define the 3D vessel tree (see Figure 5.1 and Table 5.1 and 5.2). In contrary to the vessel behavior reported by Folarin et al. [101], the vascularization in the present tumor cast is coarser than in the healthy one. But Folarin et al. also stated that vesselless regions might be found in the tumor vascularization [101]. As the vessel structure in tumor tissue appears rather unpredictable, tumors with a few and no

vessels have been reported as well [50].

Figure 5.2 illustrates how the phase contrast tomogram reveals the micro-vascularization. The hemoglobin in the blood was presumed to provide sufficient contrast to distinguish the vessels from the surrounding tissue. The tomography slices show vessels in the outer regions of the tumors only, but the phase contrast in total reveals less vessels than the healthy corrosion cast according to Table 5.1 and 5.2. Histologically no endothelial cells were found in the interior of the tumor specimen. Since the tumor sample measured by means of phase tomography is younger (7 days) than the tumor used for the corrosion cast (14 days), it can be reasonably assumed that the cancerous angiogenesis is still at an early stage of its development [106].

The three dimensional vectorization of the vessel trees as shown in Figure 5.3 allows a quantitative assessment of the vessel characteristics. The casts of cancerous and healthy tissues were used to discover the differences between their micro-vascular structures. The tortuosity was expected to be larger in the tumor tissue [50,99]. The present results confirm this expectation in terms of DM and SOAM (see Table 5.1). However the tortuosity depends strongly on the choice of the selected region. In the present study, healthy tissue revealed tortuous vessels as well (see Figure 5.4 (a) inset). According to [24] tortuous capillaries can appear in the neighborhood of a muscle due to muscle compressions enforced by the cast preparation itself. The vessels of the health tissue were indeed extracted from the muscular flank of a mouse. Additionally, Aharinejad et al. [104] confirmed that capillaries with diameters below $15 \mu\text{m}$ can appear tortuously in both cancerous and healthy tissues.

The mean vessel diameter (Table 5.1 and 5.2) is smaller in the cancerous vessel cast and comparable with the result of a previous study [100]. This observation is in good agreement with the assumption of an exceeded angiogenesis in tumors involving a dense network of capillaries [107]. As a result, the evaluated vessel diameter can be used to distinguish between healthy and cancerous tissues. However it differs from the real value because of two reasons. First the corrosion cast method may cause tissue shrinkages of several percent. Second the corrosion of the surrounding tissue also affects the vessel wall. Hence the evaluated vessel diameter of the casts describes rather the diameter of the vessel lumen. Another problem of corrosion cast is the presence of leaked polymer [101], particularly, in tumor tissue where the vessels appear damaged. Figure 5.5 shows characteristic features that are interpreted as a result of leakages through damaged vessel walls.

For that reason the results of the phase contrast μCT method without contrast enhancement and polymer leakages were presented. The vessel diameters are comparable with the values of corrosion casts when the thickness of the vessel wall is taken into account. The vessel wall of capillaries (including endothelium, basal lamina, and pericytes) feature a thickness of approximately $1.0 \mu\text{m}$ in healthy tissue and of $1.2 \mu\text{m}$ in peritumoral tissue [18]. To allow a better comparison with the phase contrast based data the diameter in corrosion casts have to be increased by $2 \mu\text{m}$. Figure 5.3 shows that the vessel tree of the holotomogram seems to include numerous disconnected vessels. The disconnectivities can be a natural phenomenon or a result of the segmentation. During the Frangi-Filtering noise can lead to both virtual and disconnected vessels. As a result the number of bifurcation is small in the phase contrast based data. The number of bifurcations in the corrosion cast however is overestimated due to effect of leakages. The mean vessel length varies slightly for different regions. The phase contrast dataset delivers the smallest value, because of the part of the vessels might not have been captured by the segmentation tool.

The presence of non-connected vessels, or blind endings, in the segmented volumes can be

due either to an artifact in the image reconstruction or to a real physiological situation. In the corrosion casted tumor measured with absorption contrast mode, such endings have to be considered as artifact since we assume that the vessels have to be connected to allow the casting polymer to flow. It is therefore impossible to visualize real blind endings with this mode. Instead, in the phase contrast mode it is possible to visualize real blind endings (no contrast agent needed) but unfortunately, it is not possible to distinguish them from the artifacts. Nevertheless, from a biological point of view, the vascular structure of the tumor presents several non-connected vessels due to the continuous and non-controlled rearrangement of the vessel structure [108].

5.6 Conclusion

As tumor tissues are characterized by stronger neo-vascularization with respect to healthy tissues, the capillaries are of special interest. This study shows that the mean diameter of capillaries is 50% larger in healthy tissue than in the cancerous tissue, although there is no significant difference concerning vessel density, tortuosity, bifurcation density and angle. The mean bifurcation angle varies within the narrow range of 111 to 119 degrees. Phase contrast μ CT is a powerful alternative for the tumor vessel visualization as it allows imaging the vascularization without any material-based preparation procedure. In comparison to the corrosion cast, this approach enables further analyses such as optical microscopy of the histological slices. In future research the segmentation can be improved further by applying hysteresis thresholding [109]. It is expected to detect the bifurcation points and vascular structures in areas of weak contrast more reliably by the local choice between two thresholds. As a result, the number of vessel interrupted by the segmentation is expected to be reduced leading to a higher reliability of the quantification.

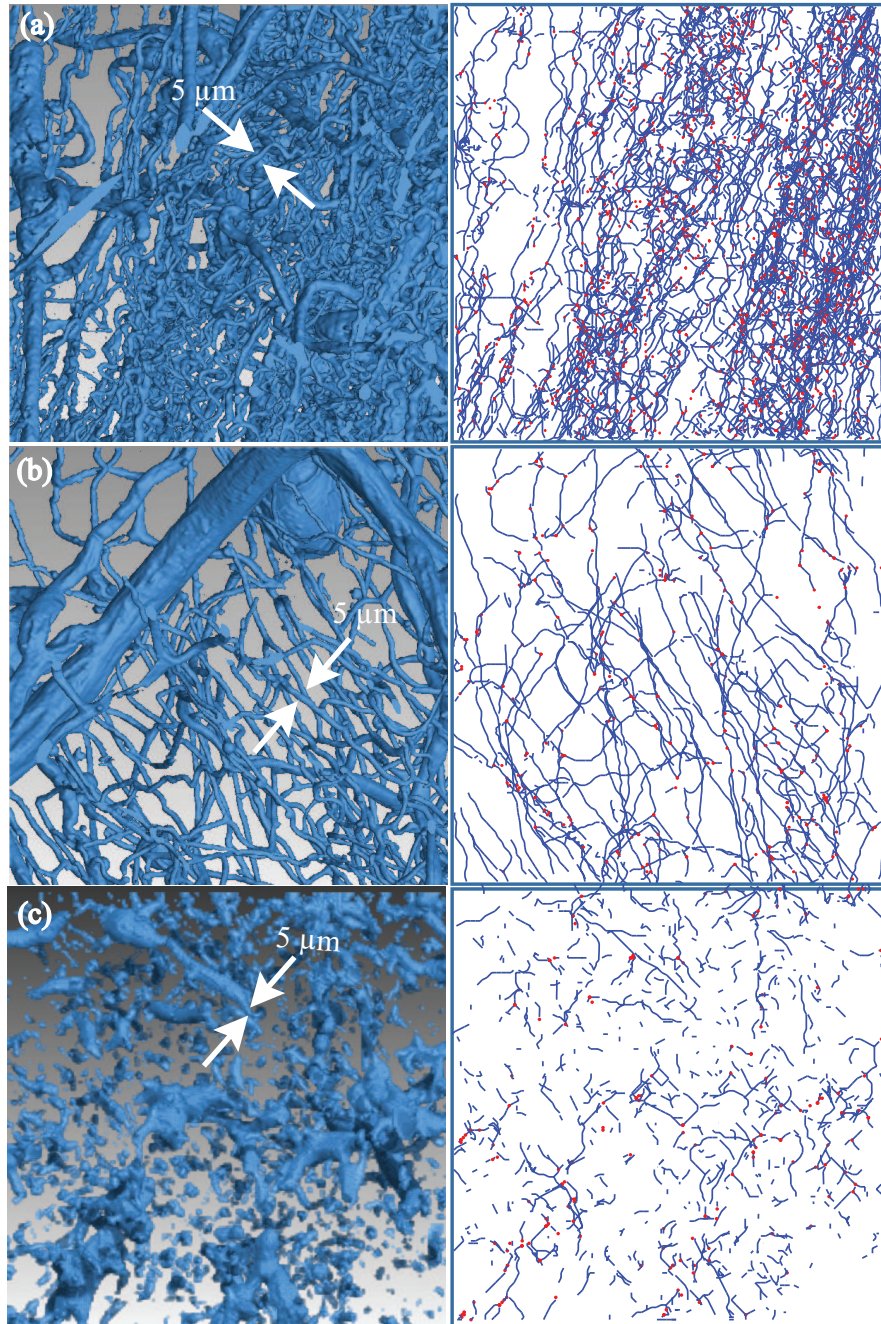


Figure 5.3: *The 3D representations of the region ROI_1 of each dataset (left) and the related vectorized vessel tree (right). The images correspond to the healthy vessel cast (a), the tumor cast (b) and the tumor in PFA acquired by phase contrast μCT (c). The red dots in the vectorized representation indicate the bifurcation points.*

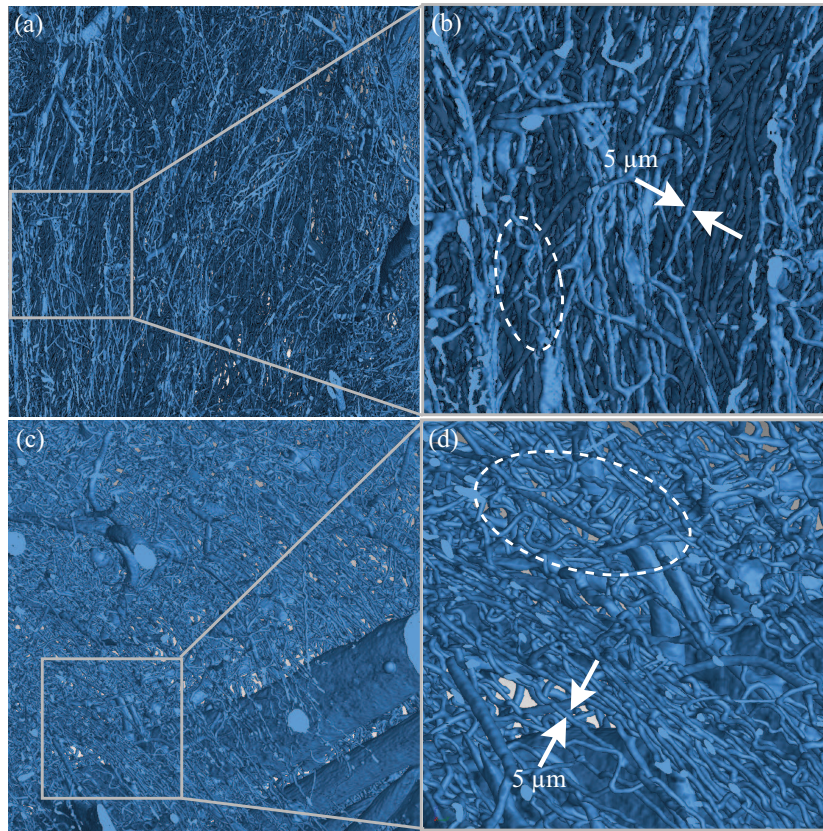


Figure 5.4: *The images show 3D representations of vessel casts (healthy, a-b, cancerous, c-d). The dashed ellipses highlight twisted vessels which are present in the healthy tissue (b) as well as in the cancerous tissue (d).*

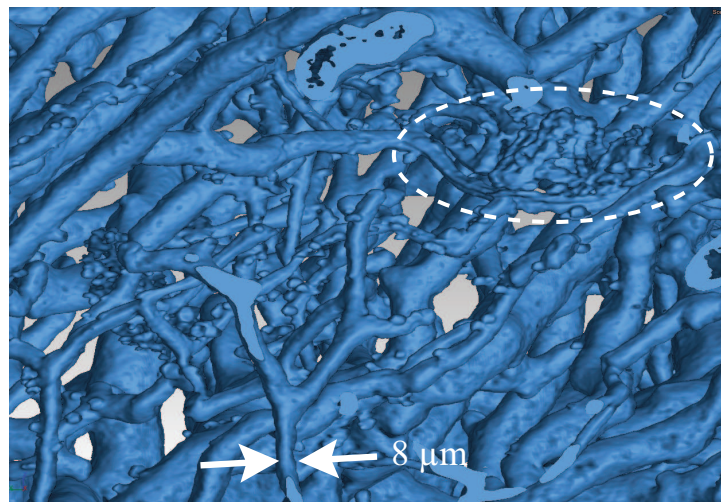


Figure 5.5: *The region of the cancerous vessel cast presented in this figure shows strong leakages of the polymer (dashed ellipse) due damaged vessel walls.*

Chapter 6

Conclusion

It is of main interest to visualize and analyze the tumor vessel tree down to the capillaries to obtain a better insight in the tumor growth. For the visualization of the tumor vascular network using absorption based SR μ CT contrast enhancement, like staining or corrosion cast was necessary to make the vessels visible in the tomographic slices. The contrast was sufficiently high to allow an extraction of the 3D vessel tree with intensity-based segmentation algorithms.

However both contrast enhancing methods had in common the same disadvantages. For both methods leakages of the perfused product could be observed [110]. This was because the necrosis inside the tumor caused damages in the vessel walls. Due to the complexity of the tumor vessel tree, it was impossible to correct the influence of the leakages in the data. Another aspect that has to be taken into account is that the contrast agent or the polymer filled only the lumen of the vessels. The vessel walls could therefore not be visualized in the tomograms, making it impossible to define the total mean diameter of the vessels. In addition, further analysis of the corrosion casts using microscopy of histological slices can not be performed since the soft and hard biological tissue had been removed for the cast preparation.

An alternative method is presented in this thesis, where contrast enhancement was unnecessary. Imaging the tumor with phase contrast based SR μ CT, the contrast has shown to be better improved in comparison to the conventional absorption based technique. The contrast of the vessels resulted most probably from the hemoglobin which is a constituent of the blood, containing iron, which exhibits a high electron density in comparison to the other part of soft tissue.

Phase contrast tomography was performed in propagation based tomography and grating interferometry setup. Both techniques have their advantages and disadvantages. Similar to the absorption based SR μ CT measurements the spatial resolution in in-line tomography is, besides the optics, only limited by the detector pixel size. Unfortunately this technique dealt with difficulties in the phase retrieval and low-frequency artifacts.

The grating interferometer did not have these problems and offers additionally a much higher contrast in the tomograms than the propagation based method. The spatial resolution in grating interferometry is however not only limited by the detector system but also by twice the periodicity of the second grating (absorption grating) and the lateral shear of two interfering waves behind the first grating (phase grating) [31]. To date, the smallest available grating period at ID19 (ESRF, Grenoble) is 2 μm . Therefore objects with diameters below

4 μm cannot be detected. Although the vessels could be identified in the phase contrast tomograms, difficult and time consuming segmentation strategies were necessary to extract the vessels from the tomography data.

For the characterization of the tumor vascularization the extraction of the vessel parameters was essential. The vectorization of the voxel-based data has shown to be a helpful tool for this purpose. Since the vectorized data format only contained information about the vessel, the format conversion caused also a strong reduction in the data size.

Since phase contrast μCT offers the possibility to visualize the tumor vessels without the need for invasive sample preparation to increase the contrast, it is therefore a promising technique for the analysis of tumor angiogenesis. As the clinical applications of phase contrast μCT s are on the rise, it can be assumed that this technique can help in the detection of illnesses during preliminary medical investigations by the analysis of the vessel characteristics. For that reason further enhancements in the vessel segmentation are necessary.

For a fast diagnosis and therefore advancements in cancer treatments in clinical research, the knowledge of tumor growth is of high importance. Computer algorithms simulating tumor growth will help to gain a better understanding in the mechanism involved and can be supported by computer scientists. In validation of the computed results for high resolution 3D images of a tumor using micro computed tomography, physicist can play a relevant role. The spatial resolution of 3D imaging modalities in clinical environment is restricted to a fraction of a millimeter. The application of micro computed tomography allows this limit to be reduced to about 1 μm . Furthermore, the usage of phase-contrast imaging enables us to not only measure the local X-ray absorption but also the changes in the local electron distributions characterized by the refractive index, so the high-resolution 3D data permits us to calibrate MR images.

The analysis of the vessel morphology can sufficiently describe the characteristic attributes of a tumor. However, it is desirable to simultaneously obtain results for the morphology and the physiology of the tumor for a better understanding in the underlying mechanism. This can be achieved by additional measurements using positron emission tomography (PET) which enables the analysis of tumor hypoxia and glucose metabolism [111]. Moreover, it would be interesting to analyze the total tumor vessel tree. This would also include the identification of the mother vessel(s) from which the vascularization has spread.

Bibliography

- [1] A.C. Kak and M. Slaney. Principles of computerized tomographic imaging. 1988.
- [2] WHO. Cancer fact sheet. <http://www.who.int/mediacentre/factsheets/fs297/en/>.
- [3] P.F.J.W. Rijken, H.J.J.A. Bernsen, and A.J. van der Kogel. Application of an image analysis system to the quantitation of tumor perfusion and vascularity in human glioma xenografts. *Microvascular Research*, 50(2):141–153, 1995.
- [4] P. Baluk, H. Hashizume, and D.M. McDonald. Cellular abnormalities of blood vessels as targets in cancer. *Current Opinion in Genetics & Development*, 15(1):102–111, 2005.
- [5] D. Hanahan. The hallmarks of cancer. *Cell*, 100(1):57–70, 2000.
- [6] G. Bergers and L.E. Benjamin. Tumorigenesis and the angiogenic switch. *Nature Reviews Cancer*, 3(6):401–410, 2003.
- [7] B. Lloyd, D. Szczerba, and G. Székely. A coupled finite element model of tumor growth and vascularization. *Medical Image Computing and Computer-Assisted Intervention*, 4792:874–881, 2007.
- [8] D. Szczerba and G. Székely. Simulating vascular systems in arbitrary anatomies. *Medical Image Computing and Computer-Assisted Intervention*, 3750:641–648, 2005.
- [9] J.G. Hanstede and P.O. Gerrits. The effects of embedding in water-soluble plastics on the final dimensions of liver sections. *Journal of Microscopy*, 131(1):79, 1983.
- [10] B. Müller, M. Germann, D. Jeanmonod, and A. Morel. Three-dimensional assessment of brain tissue morphology. In *Proceedings of SPIE*, volume 6318, pages 631803–1, 2006.
- [11] F. Plouraboué, P. Cloetens, C. Fonta, A. Steyer, F. Lauwers, and J.P. Marc-Vergnes. X-ray high-resolution vascular network imaging. *Journal of Microscopy*, 215(2):139–148, 2004.
- [12] E.B. Brown, R.B. Campbell, Y. Tsuzuki, L. Xu, P. Carmeliet, D. Fukumura, and R.K. Jain. In vivo measurement of gene expression, angiogenesis and physiological function in tumors using multiphoton laser scanning microscopy. *Nature Medicine*, 7(7):864–868, 2001.

- [13] B.J. Vakoc, R.M. Lanning, J.A. Tyrrell, T.P. Padera, L.A. Bartlett, T. Stylianopoulos, L.L. Munn, G.J. Tearney, D. Fukumura, R.K. Jain, et al. Three-dimensional microscopy of the tumor microenvironment in vivo using optical frequency domain imaging. *Nature Medicine*, 15(10):1219–1223, 2009.
- [14] C. Belisle and G. Sainte-Marie. Blood vascular network of the rat lymph node: Tridimensional studies by light and scanning electron microscopy. *American Journal of Anatomy*, 189(2):111–126, 1990.
- [15] A.O. Rodríguez. Principles of magnetic resonance imaging. *Revista Mexicana de Física*, 50(3), 2009.
- [16] M. Rudin, P.M.J. McSheehy, P.R. Allegrini, M. Rausch, D. Baumann, M. Becquet, K. Brecht, J. Brueggen, S. Ferretti, and F. Schaeffer. Ptk787/zk222584, a tyrosine kinase inhibitor of vascular endothelial growth factor receptor, reduces uptake of the contrast agent gddota by murine orthotopic b16/bl6 melanoma tumours and inhibits their growth in vivo. *NMR in Biomedicine*, 18(5):308–321, 2005.
- [17] B. Müller, J. Fischer, U. Dietz, P.J. Thurner, and F. Beckmann. Blood vessel staining in the myocardium for 3d visualization down to the smallest capillaries. *Nuclear Instruments and Methods in Physics Research Section B: Beam Interactions with Materials and Atoms*, 246(1):254–261, 2006.
- [18] M. Bertossi, D. Virgintino, E. Maiorano, M. Occhiogrosso, and L. Roncali. Ultrastructural and morphometric investigation of human brain capillaries in normal and peritumoral tissues. *Ultrastructural Pathology*, 21(1):41–49, 1997.
- [19] B. Müller, R. Bernhardt, T. Weitkamp, F. Beckmann, R. Bräuer, U. Schurig, A. Schrott-Fischer, R. Glueckert, M. Ney, and T. Beileites. Morphology of bony tissues and implants uncovered by high-resolution tomographic imaging. *International Journal of Materials Research*, 98(7):613–621, 2007.
- [20] A. Rack, T. Weitkamp, M. Riotte, D. Grigoriev, T. Rack, L. Helfen, T. Baumbach, R. Dietsch, T. Holz, and M. Kramer. Comparative study of multilayers used in monochromators for synchrotron-based coherent hard x-ray imaging. *Journal of Synchrotron Radiation*, 17(4):496–510, 2010.
- [21] B. Müller, S. Lang, M. Dominietto, M. Rudin, G. Schulz, H. Deyhle, M. Germann, F. Pfeiffer, C. David, and T. Weitkamp. High-resolution tomographic imaging of microvessels. In *Proceedings of SPIE*, volume 7078, pages 70780B–1, 2008.
- [22] M. Dominietto, F. Beckmann, J. Herzen, and B. Müller. Brain vessel staining for the visualization with micro computed tomography. *HASYLAB Annual Report*, 1:1–2, 2007.
- [23] M. Dominietto, S. Friess, S. Grabherr, J. Herzen, F. Beckmann, and B. Müller. Vessel tree visualization with synchrotron radiation-based micro computed tomography. *HASYLAB Annual Report*, 2:1559–1560, 2007.
- [24] R.F. Potter and A.C. Groom. Capillary diameter and geometry in cardiac and skeletal muscle studied by means of corrosion casts. *Microvascular Research*, 25(1):68–84, 1983.

- [25] T. Krucker, A. Lang, and E.P. Meyer. New polyurethane-based material for vascular corrosion casting with improved physical and imaging characteristics. *Microscopy Research and Technique*, 69(2):138–147, 2006.
- [26] S. Heinzer, T. Krucker, M. Stampanoni, R. Abela, E.P. Meyer, A. Schuler, P. Schneider, and R. Müller. Hierarchical microimaging for multiscale analysis of large vascular networks. *Neuroimage*, 32(2):626–636, 2006.
- [27] C. Kottler, C. David, F. Pfeiffer, and O. Bunk. A two-directional approach for grating based differential phase contrast imaging using hard x-rays. *Optics Express*, 15(3):1175–1181, 2007.
- [28] F. Pfeiffer, C. David, O. Bunk, T. Donath, M. Bech, G. Le Duc, A. Bravin, and P. Cloetens. Region-of-interest tomography for grating-based x-ray differential phase-contrast imaging. *Physical Review Letters*, 101(16):168101, 2008.
- [29] F. Pfeiffer, T. Weitkamp, and C. David. X-ray phase contrast imaging using a grating interferometer. *Europhysicsnews*, 37:13–15, 2006.
- [30] R. Fitzgerald. Phase-sensitive x-ray imaging. *Physics Today*, 53:23–26, 2000.
- [31] T. Weitkamp, A. Diaz, C. David, F. Pfeiffer, M. Stampanoni, P. Cloetens, and E. Ziegler. X-ray phase imaging with a grating interferometer. *Optics Express*, 13(16):6296–6304, 2005.
- [32] A. Momose, T. Takeda, Y. Itai, and K. Hirano. Phase-contrast x-ray computed tomography for observing biological soft tissues. *Nature Medicine*, 2(4):473–475, 1996.
- [33] F. Pfeiffer, T. Weitkamp, O. Bunk, and C. David. Phase retrieval and differential phase-contrast imaging with low-brilliance x-ray sources. *Nature Physics*, 2(4):258–261, 2006.
- [34] D. Gabor. A new microscopic principle. *Nature*, 161(4098):777–778, 1948.
- [35] S. Zabler, P. Cloetens, J.P. Guigay, J. Baruchel, and M. Schlenker. Optimization of phase contrast imaging using hard x rays. *Review of Scientific Instruments*, 76:073705, 2005.
- [36] D. Paganin, S.C. Mayo, T.E. Gureyev, P.R. Miller, and S.W. Wilkins. Simultaneous phase and amplitude extraction from a single defocused image of a homogeneous object. *Journal of Microscopy*, 206(1):33–40, 2002.
- [37] M. Langer, P. Cloetens, J.P. Guigay, and F. Peyrin. Quantitative comparison of direct phase retrieval algorithms in in-line phase tomography. *Medical Physics*, 35:4556, 2008.
- [38] P.C. Diemoz, P. Coan, I. Zanette, A. Bravin, S. Lang, C. Glaser, and T. Weitkamp. A simplified approach for computed tomography with an x-ray grating interferometer. *Optics Express*, 19(3):1691–1698, 2011.
- [39] C. David, B. Nöhammer, H.H. Solak, and E. Ziegler. Differential x-ray phase contrast imaging using a shearing interferometer. *Applied Physics Letters*, 81:3287, 2002.

- [40] A. Momose. Phase-sensitive imaging and phase tomography using x-ray interferometers. *Optics Express*, 11(19):2303–2314, 2003.
- [41] T. Weitkamp, C. David, O. Bunk, J. Bruder, P. Cloetens, and F. Pfeiffer. X-ray phase radiography and tomography of soft tissue using grating interferometry. *European Journal of Radiology*, 68(3):S13–S17, 2008.
- [42] M. Dominietto. *Multimodality Approach to Study the Fractal Physiology of Tumor Angiogenesis*. PhD thesis, ETH Zurich, 2011.
- [43] K. Myojin, A. Taguchi, K. Umetani, K. Fukushima, N. Nishiura, T. Matsuyama, H. Kimura, D.M. Stern, Y. Imai, and H. Mori. Visualization of intracerebral arteries by synchrotron radiation microangiography. *American Journal of Neuroradiology*, 28(5):953–957, 2007.
- [44] T. Weitkamp, I. Zanette, C. David, J. Baruchel, M. Bech, P. Bernard, H. Deyhle, T. Donath, S. Lang, J. Mohr, B. Müller, F. Pfeiffer, E. Reznikova, S. Rutishauser, G. Schulz, and J.P. Tapfer, A. and Valade. Recent developments in x-ray talbot interferometry at esrf-id19. In *Proceedings of SPIE*, volume 7804, pages 780406–1, 2010.
- [45] T. Weitkamp, D. Haas, D. Wegrzynek, and A. Rack. Ankaphase: Software for single-distance phase retrieval from inline x-ray phase-contrast radiographs. *Journal of Synchrotron Radiation*, 18(4):617–629, 2011.
- [46] A. Andronache, M. von Siebenthal, G. Székely, and P. Cattin. Non-rigid registration of multi-modal images using both mutual information and cross-correlation. *Medical Image Analysis*, 12(1):3–15, 2008.
- [47] Y. Sato, S. Nakajima, N. Shiraga, H. Atsumi, S. Yoshida, T. Koller, G. Gerig, and R. Kikinis. Three-dimensional multi-scale line filter for segmentation and visualization of curvilinear structures in medical images. *Medical Image Analysis*, 2(2):143–168, 1998.
- [48] J. Collins, C. Kurcz, C. Lisle, Y. Liu, and E. Zudaire. Assessment of vascular network segmentation. *International Journal of Image Processing*, 4(6):584, 2011.
- [49] N.D. Cornea, D. Silver, X. Yuan, and R. Balasubramanian. Computing hierarchical curve-skeletons of 3d objects. *The Visual Computer*, 21(11):945–955, 2005.
- [50] E. Bullitt, G. Gerig, S. Aylward, S. Joshi, K. Smith, M. Ewend, and W. Lin. Vascular attributes and malignant brain tumors. *Medical Image Computing and Computer-Assisted Intervention*, 2878:671–679, 2003.
- [51] M.P. Wiedeman. Dimensions of blood vessels from distributing artery to collecting vein. *Circulation Research*, 12(4):375, 1963.
- [52] T. Takeda, Y. Itai, K. Hyodo, M. Ando, T. Akatsuka, and C. Uyama. Medical applications with synchrotron radiation in japan. *Journal of Synchrotron Radiation*, 5(3):326–332, 1998.

- [53] D. Haberthur, C. Hintermuller, F. Marone, J.C. Schittny, and M. Stampanoni. Radiation dose optimized lateral expansion of the field of view in synchrotron radiation x-ray tomographic microscopy. *Journal of Synchrotron Radiation*, 17(5):590–599, 2010.
- [54] A. Faridani, E.L. Ritman, and K.T. Smith. Examples of local tomography. *SIAM Journal on Applied Mathematics*, 52:1193–1198, 1992.
- [55] T.E. Gureyev, Y.I. Nesterets, and S.C. Mayo. Quantitative quasi-local tomography using absorption and phase contrast. *Optics Communications*, 280(1):39–48, 2007.
- [56] T. Köhler and F. Noo. Comment on region-of-interest tomography for grating-based x-ray differential phase-contrast imaging. *Physical Review Letters*, 102(3):39801, 2009.
- [57] S. Bonnet, F. Peyrin, F. Turjman, and R. Prost. Tomographic reconstruction using nonseparable wavelets. *Image Processing, IEEE Transactions*, 9(8):1445–1450, 2000.
- [58] F. Marone, B. Münch, and M. Stampanoni. Fast reconstruction algorithm dealing with tomography artifacts. In *Proceedings of SPIE*, volume 7804, page 780410, 2010.
- [59] H. Kudo, M. Courdurier, F. Noo, and M. Defrise. Tiny a priori knowledge solves the interior problem in computed tomography. *Physics in Medicine and Biology*, 53:2207, 2008.
- [60] M. Stampanoni, A. Groso, A. Isenegger, G. Mikuljan, Q. Chen, A. Bertrand, S. Henein, R. Betemps, U. Frommherz, and P. Böhler. Trends in synchrotron-based tomographic imaging: The sls experience. In *Proceedings of SPIE*, volume 6318, pages 63180M–1, 2006.
- [61] PCO-AG. pco.2000 cooled digital 14 bit ccd camera system. product sheet, 2008.
- [62] A. Mirone, R. Wilcke, A. Hammersley, and C. Ferrero. Pyhst high speed tomographic reconstruction. <http://www.esrf.eu/UsersAndScience/Experiments/TBS/SciSoft/>, 2010.
- [63] J. Modersitzki. *Numerical Methods for Image Registration*. Oxford University Press, USA, 2004.
- [64] Z.F. Knops, J.B.A. Maintz, M.A. Viergever, and J.P.W. Pluim. Normalized mutual information based registration using k-means clustering and shading correction. *Medical Image Analysis*, 10(3):432–439, 2006.
- [65] P. Thurner, F. Beckmann, and B. Müller. An optimization procedure for spatial and density resolution in hard x-ray micro-computed tomography. *Nuclear Instruments and Methods in Physics Research Section B: Beam Interactions with Materials and Atoms*, 225(4):599–603, 2004.
- [66] R.C. Gonzalez and R.E. Woods. *Digital Image Processing*. Prentice Hall Upper Saddle River, NJ:, 2002.
- [67] P. Schneider, R. Voide, M. Stampanoni, and R. Müller. Post-processing technique for improved assessment of hard tissues in the submicrometer domain using local synchrotron radiation-based computed tomography. *Biomedical Engineering*, 54(1):48–54, 2009.

- [68] T. Weitkamp, C. Rau, A.A. Snigirev, B. Benner, T.F. Guenzler, M. Kuhlmann, and C.G. Schroer. In-line phase contrast in synchrotron-radiation microradiography and tomography. In *Proceedings of SPIE*, volume 4503, page 92, 2002.
- [69] T. Frese, N.C. Rouze, C.A. Bouman, K. Sauer, and G.D. Hutchins. Quantitative comparison of fbp, em, and bayesian reconstruction algorithms for the indypet scanner. *Medical Imaging, IEEE Transactions*, 22(2):258–276, 2003.
- [70] B. Hamelin, Y. Goussard, J.P. Dussault, G. Cloutier, G. Beaudoin, and G. Soulez. Design of iterative roi transmission tomography reconstruction procedures and image quality analysis. *Medical Physics*, 37:4577, 2010.
- [71] T. Martin and A. Koch. Recent developments in x-ray imaging with micrometer spatial resolution. *Journal of Synchrotron Radiation*, 13(2):180–194, 2006.
- [72] A. Tsuchiyama, K. Uesugi, T. Nakano, and S. Ikeda. Quantitative evaluation of attenuation contrast of x-ray computed tomography images using monochromatized beams. *American Mineralogist*, 90(1):132, 2005.
- [73] A. Koch, C. Raven, P. Spanne, and A. Snigirev. X-ray imaging with submicrometer resolution employing transparent luminescent screens. *Journal of the Optical Society of America A*, 15(7):1940–1951, 1998.
- [74] B. Müller, F. Beckmann, M. Huser, F. Maspero, G. Székely, K. Ruffieux, P. Thurner, and E. Wintermantel. Non-destructive three-dimensional evaluation of a polymer sponge by micro-tomography using synchrotron radiation. *Biomolecular Engineering*, 19(2-6):73–78, 2002.
- [75] A. Snigirev, I. Snigireva, V. Kohn, S. Kuznetsov, and I. Schelokov. On the possibilities of x-ray phase contrast microimaging by coherent high-energy synchrotron radiation. *Review of Scientific Instruments*, 66(12):5486–5492, 1995.
- [76] P. Thurner, B. Müller, F. Beckmann, T. Weitkamp, C. Rau, R. Müller, J.A. Hubbell, and U. Sennhauser. Tomography studies of human foreskin fibroblasts on polymer yarns. *Nuclear Instruments and Methods in Physics Research Section B: Beam Interactions with Materials and Atoms*, 200:397–405, 2003.
- [77] X. Xiao, F. De Carlo, and S. Stock. Practical error estimation in zoom-in and truncated tomography reconstructions. *Review of Scientific Instruments*, 78:063705, 2007.
- [78] M. Germann, A. Morel, F. Beckmann, A. Andronache, D. Jeanmonod, and B. Müller. Strain fields in histological slices of brain tissue determined by synchrotron radiation-based micro computed tomography. *Journal of Neuroscience Methods*, 170(1):149–155, 2008.
- [79] F. Beckmann, U. Bonse, F. Busch, and O. Günnewig. X-ray microtomography ([mu]ct) using phase contrast for the investigation of organic matter. *Journal of Computer Assisted Tomography*, 21(4):539, 1997.

- [80] A. Momose, T. Takeda, Y. Itai, A. Yoneyama, and K. Hirano. Phase-contrast tomographic imaging using an x-ray interferometer. *Journal of Synchrotron Radiation*, 5(3):309–314, 1998.
- [81] E. Förster, K. Goetz, and P. Zaumseil. Double crystal diffractometry for the characterization of targets for laser fusion experiments. *Kristall und Technik*, 15(8):937–945, 1980.
- [82] T.J. Davis, D. Gao, T.E. Gureyev, A.W. Stevenson, and S.W. Wilkins. Phase-contrast imaging of weakly absorbing materials using hard x-rays. *Nature*, 373(6515):595–598, 1995.
- [83] S.W. Wilkins, T.E. Gureyev, D. Gao, A. Pogany, and A.W. Stevenson. Phase-contrast imaging using polychromatic hard x-rays. *Nature*, 384(6607):335–338, 1996.
- [84] P. Cloetens, R. Barrett, J. Baruchel, J.P. Guigay, and M. Schlenker. Phase objects in synchrotron radiation hard x-ray imaging. *Journal of Physics D: Applied Physics*, 29:133, 1996.
- [85] A. Olivo and R. Speller. Modelling of a novel x-ray phase contrast imaging technique based on coded apertures. *Physics in Medicine and Biology*, 52:6555, 2007.
- [86] P. Cloetens, W. Ludwig, J. Baruchel, D. Van Dyck, J. Van Landuyt, J.P. Guigay, and M. Schlenker. Holotomography: Quantitative phase tomography with micrometer resolution using hard synchrotron radiation x rays. *Applied Physics Letters*, 75(19):2912–2914, 1999.
- [87] M. Langer, P. Cloetens, and F. Peyrin. Regularization of phase retrieval with phase-attenuation duality prior for 3-d holotomography. *Image Processing, IEEE Transactions*, 19(9):2428–2436, 2010.
- [88] T. Weitkamp, P. Tafforeau, E. Boller, P. Cloetens, J.P. Valade, P. Bernard, F. Peyrin, W. Ludwig, L. Helfen, and J. Baruchel. Status and evolution of the esrf beamline id19. *AIP Conference Proceeding*, 1221:33–38, 2010.
- [89] T. Weitkamp, C. David, C. Kottler, O. Bunk, and F. Pfeiffer. Tomography with grating interferometers at low-brilliance sources. In *Proceedings of SPIE*, volume 6318, page 63180S, 2006.
- [90] I. Zanette, T. Weitkamp, S. Lang, M. Langer, J. Mohr, C. David, and J. Baruchel. Quantitative phase and absorption tomography with an x-ray grating interferometer and synchrotron radiation. *Physica Status Solidi (a)*, 208:2526–2532, 2011.
- [91] J.P. Guigay, M. Langer, R. Boistel, and P. Cloetens. Mixed transfer function and transport of intensity approach for phase retrieval in the fresnel region. *Optics Letters*, 32(12):1617–1619, 2007.
- [92] P. Modregger, D. Lübbert, P. Schäfer, and R. Köhler. Spatial resolution in bragg-magnified x-ray images as determined by fourier analysis. *Physica Status Solidi (a)*, 204(8):2746–2752, 2007.

- [93] G. Schulz, T. Weitkamp, I. Zanette, F. Pfeiffer, F. Beckmann, C. David, S. Rutishauser, E. Reznikova, and B. Müller. High-resolution tomographic imaging of a human cerebellum: Comparison of absorption and grating-based phase contrast. *Journal of the Royal Society Interface*, 7(53):1665, 2010.
- [94] J. Herzen, T. Donath, F. Pfeiffer, O. Bunk, C. Padeste, F. Beckmann, A. Schreyer, and C. David. Quantitative phase-contrast tomography of a liquid phantom using a conventional x-ray tube source. *Optics Express*, 17:10010–10018, 2009.
- [95] R. Wild, S. Ramakrishnan, J. Sedgewick, and A.W. Griffioen. Quantitative assessment of angiogenesis and tumor vessel architecture by computer-assisted digital image analysis: Effects of vegf-toxin conjugate on tumor microvessel density. *Microvascular Research*, 59(3):368–376, 2000.
- [96] A. Frangi, W. Niessen, K. Vincken, and M. Viergever. Multiscale vessel enhancement filtering. *Medical Image Computing and Computer-Assisted Intervention*, 1496:130–137, 1998.
- [97] D. Lesage, E.D. Angelini, I. Bloch, and G. Funka-Lea. A review of 3d vessel lumen segmentation techniques: Models, features and extraction schemes. *Medical Image Analysis*, 13(6):819–845, 2009.
- [98] F. Beckmann. Microtomography using synchrotron radiation as a user experiment at beamlines bw2 and bw5 of hasylab at desy. In *Proceedings of SPIE*, volume 4503, page 34, 2002.
- [99] E. Bullitt, G. Gerig, S.M. Pizer, W. Lin, and S.R. Aylward. Measuring tortuosity of the intracerebral vasculature from mra images. *Medical Imaging, IEEE Transactions*, 22(9):1163–1171, 2003.
- [100] E.M. Brey, T.W. King, C. Johnston, L.V. McIntire, G.P. Reece, and C.W. Patrick. A technique for quantitative three-dimensional analysis of microvascular structure. *Microvascular Research*, 63(3):279–294, 2002.
- [101] A.A. Folarin, M.A. Konerding, J. Timonen, S. Nagl, and R.B. Pedley. Three-dimensional analysis of tumour vascular corrosion casts using stereoinaging and micro-computed tomography. *Microvascular Research*, 80(1):89–98, 2010.
- [102] X. Wu, N. Kathuria, C.W. Patrick, and G.P. Reece. Quantitative analysis of the microvasculature growing in the fibrin interface between a skin graft and the recipient site. *Microvascular Research*, 75(1):119–129, 2008.
- [103] S. Lang, M. Dominietto, P. Cattin, T. Weitkamp, A. Ulmann, and B. Müller. Global and local hard x-ray tomography of a centimetre-sized tumor vessel tree. *Journal of Synchrotron Radiation*, 19, 2012.
- [104] S. Aharinejad, W. Schreiner, and F. Neumann. Morphometry of human coronary arterial trees. *The Anatomical Record*, 251(1):50–59, 1998.

- [105] J. Zhou, S. Chang, D. Metaxas, and L. Axel. Vessel boundary extraction using ridge scan-conversion deformable model. In *Biomedical Imaging: Nano to Macro, IEEE International Symposium*, pages 189–192. IEEE, 2006.
- [106] G.N. Naumov, L.A. Akslen, and J. Folkman. Role of angiogenesis in human tumor dormancy: Animal models of the angiogenic switch. *Cell Cycle*, 5(16):1779, 2006.
- [107] D. Fukumura and R.K. Jain. Tumor microvasculature and microenvironment: Targets for anti-angiogenesis and normalization. *Microvascular Research*, 74(2):72–84, 2007.
- [108] D. Marmé and N. Fusenig. *Tumor Angiogenesis: Basic Mechanisms and Cancer Therapy*. Springer Verlag, 2007.
- [109] D. Wilson and J. Noble. Segmentation of cerebral vessels and aneurysms from mr angiography data. In *Information Processing in Medical Imaging*, pages 423–428. Springer, 1997.
- [110] P.D. Harris and A. Desoky. Analysis of microvascular systems using image processing. In *IEEE Conference Proceedings*, pages 690–693. IEEE, 1988.
- [111] J.G. Rajendran, D.A. Mankoff, F. O’ Sullivan, L.M. Peterson, D.L. Schwartz, E.U. Conrad, A.M. Spence, M. Muzi, D.G. Farwell, and K.A. Krohn. Hypoxia and glucose metabolism in malignant tumors. *Clinical Cancer Research*, 10(7):2245–2252, 2004.

Acknowledgments

Everybody who is part of my life has contributed to this thesis in one way or another. Therefore I would like to thank all of you.

Ik wull mi bedanken bi all de Lüüd, de mi in de Tied von mien Doktorarbeit jümmer ünnerstützt hebbt. Daarto hören nich blots de, de mi dorbi holpen hebbt, sünnern ok de, de mi de Tied so kommodig as möglich makt hebt.

Toerst segg ik mien Dank to **Bert Müller**, mien Doktorvadder, de mi de Möglichkeit geven hett, düsse Arbeit überhaupt to maken. He Lehr mi een goodes Oog för ?t Detail to kriegen. Du hest mi jümmers föddert un me dordörch bit an?t Enn bröcht.

Tweetens wull ik **Timm Weitkamp** danke seggen, för sien Gedüür un dat he me soveel bibröcht hett. Mit em öber physikalische Soken to diskuteern hett mi jümmers veel Freud makt und mi motiveert.

I would also like to thank: / Ik wull mi ook noch ganz hartli bedanken bi:

Marco Dominiotto:

Attività di laboratorio con te è sempre stato associato al piacere. Il tuo modo tranquillo che staro facendo molto bene. Grazie! Speriamo di si riunisce una volta tra Giappone e l'Australia.

Philippe Cattin:

Du hest mi allens öber MATLAB un Bildverarbeitung bibröcht. Un obschoonst ik keen student vun di wesen bünn, hest Du mi jümmers holpen.

Silja Kiriyanthan:

Mien Leidensgenossin. Tohoop hebbt wi jümmer den Namiddag op'n Balkon hockt un öber unse Probleme klönen kunnt. öber mathematische Probleme wusst du ook immer good Bescheid un hest mi dat ok jümmer good verklören kunnt. Ik wünsch Di noch ganz veel Glück bi dine Arbeit.

Hans Deyhle, Georg Schulz, Simone Hieber, Maggie Holme un Therese Bormann:

Veele Probleme köönt blots löst warden, wenn en se mit annerlüüd diskuteern deit. Dat weer mit jüm jümmers möglich, dafür wull ik mi bedanken. Ji hebt mi ok jümmers holpen, mien?n Texte to korrigiern. Dat is ja nich jümmers eenfach ween. Dorüm veelen Dank.

Mien Modder:

Dafür dat du to jeder Tied en open Ohr for mi harrst. Du weerst jümmers för mi dor.

Mien Vadder:

Ook wenn du dat nich mehr belevt hest, bün ik mi seker, datt ik allens, wat ik erreicht heff, di to danken heff.

Krischan:

Wi sünd jümmers een Meen'n un dat obschoonst wi so raar mitenanner snacken doot. Düsse Verbinn' is wat Besünners un ik will höpen, datt dat ok in Tokunft so blifft.

Oma:

Di is dat egol, wat ik nu Physiker bün or Eier op'n Markt verkoopen do. För di bün ik eenfach blots ene Enkelin, un dat Gefühl is mi doch von all dat leevste.

Christa un Hans Peter Mosimann:

Ji geven mi dat Gefühl, ok in der Schweiz to huus to sein. Ji hebbt mi ok jümmers holpen, wenn ik mi mit de schweizer Bürokratie nicht utkennt heff.

Irene Zanette:

Tu mi hai aiutato al lavoro e sempre reso la vita più facile in Francia. Grazie. Vi auguro tutto il meglio in futuro.

MIAC:

Bi jüm bedank ik mi för de 'Free Food', de ik bi jüm jümmers kregen heff.

Younhwa Kim:

나에게 친절하게 대해 주었던 너와 너의 가족들에게 감사해. 나는 너가 항상 행복하기를 바랄게.

Gretje Hell:

Mit keeneen verstoh ik mi so good as mit mien leev Gretje. Du steckst mi jümmers an mit dien Fröhlichkeit un schaffst dat jümmers wedder, mi ok öber de lüttjen Dinger int Leben to freun.

Takashi Ogasawara:

君には笑わされてばかりだよ。君は、良い友達だけでなく良い先生でもあるなあ。ずっと仲良しでいてね。

Jasmin Vural, Imke (Diddens) Greving, Franziska Curdt, Esther Dönsdorf und Yvonne Roed:

Ji weern mien Leidensgenossen in de akademische Tied un obschoonst wi nu öber de ganze Welt verdeelt warrt, hebt wi ok in der PhD Tied tosamen leden. We sünd en goodet Team. Un dat ward ok jümmer so blieven.

Naomi Kishiwada:

以前のようにしょっちゅうは会えないけど、ずっと私たちは友だちだよ。元気でいてね。そしてご家族にもどうかよろしく。

Johanna (Wissenbach) Preuß:

Vun all mien Frünnen kenn ik di nu an'n längsten. Du büst dat afsluut Gegendeel vun mi un liekers verstahn wi uns jümmer so god. Dank Di hebb ik de Möglichkeit, ok mol in de annere Richt to kieken.

Kumiko Shimizu:

キールより横浜へ感謝を込めて。会えてとても楽しかったよ、多言語(英、日、独) だったしね～。楽しい時間をありがとう。

Uta Becht und Nicole Kegel:

Ji hebbt dat schafft, mi ok mal von de Arbeit aftolenken. Wi hebbt so veel lacht in all de Tied. Ik hööp, datt wi uns nich ut de Oogen verleeren doot.

Curriculum Vitae

Name: Sabrina Lang
Citizenship: Germany
Professional Address: Biomaterials Science Center (BMC)
University of Basel
c/o University Hospital Basel
Date of Birth: 29.05.1983
Place of Birth: Kiel, Germany

Education

2008 Diploma in physics at the Christian-Albrecht Universität zu Kiel (D)
2002 Qualification for university entrance at Hans-Geiger-Gymnasium in Kiel (D)
1999 Certificate for Realschule at the Realschule Flintbek (D)

Employment

Research

2008-2011 Dissertation *The Visualization of the Tumor Vascularization using Micro Computed Tomography* at the Biomaterials Science Center (BMC) in Basel, Switzerland

Publication

- 2012 **S. Lang**, M. Dominiotto, P. Cattin, T. Weitkamp, A. Ulmann, B. Müller, *Global and local hard X-ray tomography of a centimetre-sized tumour vessel tree*, Journal of Synchrotron Radiation 19 (1) 114-125.
- 2012 B. Müller, H. Deyhle, **S. Lang**, G. Schulz, T. Bormann, F. Fierz, S. Hieber *Three-dimensional registration of tomography data for quantification in biomaterials science*, International Journal of Materials Research 103 (2) (2012) 242-249.
- 2011 I. Zanette, T. Weitkamp, **S. Lang**, M. Langer, J. Mohr, C. David, J. Baruchel, *Quantitative Phase and Absorption Tomography with an X-ray Grating Interferometer and Synchrotron Radiation*, Physica Status Solidi (a), 208, 2526 - 2532.

- 2011 P. C. Diemoz, P. Coan, I. Zanette, A. Bravin, **S. Lang**, C. Glaser, T. Weitkamp, *A simplified approach for computed tomography with an x-ray grating interferometer*, Optics Express 19 (3) (2011) 1691-1698.
- 2010 T. Weitkamp, I. Zanette, G. Schulz, M. Bech, S. Rutishauser, **S. Lang**, T. Donath, A. Tapfer, H. Deyhle, P. Bernard, J. Valade, E. Reznikova, J. Kenntner, J. Mohr, B. Müller, F. Pfeiffer, C. David, J. Baruchel, *X-ray grating interferometry at ESRF: Applications and recent technical developments* AIP Conference Proceedings 1365 28-31.
- 2010 T. Weitkamp, I. Zanette, C. David, J. Baruchel, M. Bech, P. Bernard, H. Deyhle, T. Donath, J. Kenntner, **S. Lang**, J. Mohr, B. Müller, F. Pfeiffer, E. Reznikova, S. Rutishauser, G. Schulz, A. Tapfer, J. Valade, *Recent developments in x-ray talbot interferometry at ESRF-ID19*, Proceedings of SPIE 7804 (2010) 780406.
- 2009 **S. Lang**, M. Dominietto, B. Müller, *Visualization of tumor vessels using synchrotron radiation-based micro computed tomography*, Journal of Physics: Conference Series 186 (2009) 012088.
- 2008 B. Müller, **S. Lang**, M. Dominietto, M. Rudin, G. Schulz, H. Deyhle, M. Germann, F. Pfeiffer, C. David, T. Weitkamp, *High-resolution tomographic imaging of microvessels*, Proceedings of SPIE 7078 (2008) 70780B.
- 2008 **S. Lang**, M. Dominietto, F. Beckmann, J. Herzen, B. Müller *Vessel staining in tumours by angiofil*, European Cells and Materials 16 (1) (2008) 39.